Inaugural dissertation

for

obtaining the doctoral degree

of the

Combined Faculty of Mathematics, Engineering and Natural Sciences

of the

Ruprecht - Karls - University

Heidelberg

Presented by

M.Sc. Jonas Norbert Schwickert

born in: Limburg an der Lahn, Germany

Oral examination: 1st of March 2024

Characterization of PARP inhibitor resistance in patient-derived ovarian cancer cell lines

Referees:

Prof. Dr. Andreas Trumpp

Prof. Dr. Benedikt Brors

„Wenn wir wüssten, was wir tun, würde das nicht Forschung heißen, oder?“ (Albert Einstein)

1. Declaration

The work presented in this dissertation was performed from September 2018 until December 2023 at the German Cancer Research Center (Deutsches Krebsforschungszentrum, DKFZ, Heidelberg) and the Heidelberg Institute for Stem Cell Technology and Experimental Medicine (HI-STEM gGmbH, Heidelberg) under the supervision of Prof. Dr. Andreas Trumpp and Dr. Martin Sprick.

Declarations according to § 8 (3) c), d) and h) of the Doctoral Degree Regulations:

c) I hereby declare that I have written the submitted dissertation myself and, in this process, have used no other sources or materials than those explicitly indicated.

d) I hereby declare that I have not applied to be examined at any other institution, nor have I used the dissertation in this way or any other form at any other institution as an examination paper nor submitted it to any other faculty as dissertation.

h) I hereby consent to the verification of the dissertation by means of electronic data processing programs against standing scientific standards.

2. Summary

Poly(ADP-ribose) polymerase inhibitors (PARPis) have exhibited significant efficacy in clinical settings and thus shown promise as a therapeutic option for ovarian cancer patients with BRCA mutations. However, the emergence of resistance to PARPis poses a substantial challenge, limiting its long-term effectiveness. Consequently, understanding additional resistance mechanisms is crucial to improve the treatment efficacy of PARPis.

In this thesis, I utilized patient-derived ovarian cancer cell lines initially screened for their response to PARPi treatment. To induce resistance, the two most responsive cell lines were subjected to multiple rounds of increasing concentrations of olaparib (the first approved PARPi) treatment. Notably, both cell lines were Homologous Recombination (HR)-proficient, making them theoretically unsuitable for PARPi treatment. Employing various molecular and sequencing approaches, I investigated and characterized the acquired PARPi resistance mechanism in these HR-proficient ovarian cancer cell lines.

Surprisingly, I did not detect a known resistance mechanism to PARPis, possibly due to the HR proficiency of both resistant and sensitive cells. However, the olaparib-resistant cell lines demonstrated cross-resistance to other PARPis (Pamiparib, Niraparib, Rucaparib, Talazoparib) while remaining sensitive to DNA-damaging agents, suggesting a PARP-specific and DNA repair-independent resistance mechanism. Yet, the precise mechanism underlying acquired resistance to PARPis in both cell lines remains to be determined. Nonetheless, the observation that HR-proficient cell lines can be susceptible to PARPi treatment may expand the potential treatment scope of PARPis to patients traditionally excluded based on their HR status.

In summary, this study demonstrates that some HR-proficient cells can be vulnerable to PARPi treatment and that the acquired resistance in these cell lines is independent of DNA repair pathways.

3. Zusammenfassung

Poly(ADP-Ribose)-Polymerase-Inhibitoren (PARPis) haben in der klinischen Praxis eine beachtliche Wirksamkeit gezeigt und sich somit als vielversprechende Therapieoption für Eierstockkrebspatientinnen mit BRCA-Mutationen erwiesen. Das Auftreten von Resistenzen gegen PARPis stellt jedoch eine große Herausforderung dar und schränkt die langfristige Wirksamkeit von PARPis ein. Daher ist das Verständnis zusätzlicher Resistenzmechanismen von entscheidender Bedeutung, um die Wirksamkeit der Behandlung mit PARPis zu verbessern.

In dieser Arbeit habe ich von Patientinnen stammende Eierstockkrebs-Zelllinien verwendet, die zunächst auf ihr Ansprechen auf eine PARPi-Behandlung untersucht wurden. Um eine Resistenz zu induzieren, wurden die beiden Zelllinien, die am stärksten darauf ansprachen, mehreren Runden mit steigenden Konzentrationen von Olaparib (dem ersten zugelassenen PARPi) unterzogen. Bemerkenswert ist, dass beide Zelllinien eine homologe Rekombination (HR) aufwiesen, was sie theoretisch für eine PARPi-Behandlung ungeeignet macht. Mit Hilfe verschiedener molekularer und sequenzieller Methoden untersuchte und charakterisierte ich den Mechanismus der erworbenen PARPi-Resistenz in diesen HR-positive Eierstockkrebs-Zelllinien.

Überraschenderweise konnte ich keinen bekannten Resistenzmechanismus gegenüber PARPis feststellen, was möglicherweise darauf zurückzuführen ist, dass sowohl die resistenten als auch die sensiblen Zellen HR-fähig sind. Die Olaparib-resistenten Zelllinien zeigten jedoch eine Kreuzresistenz gegenüber anderen PARPis (Pamiparib, Niraparib, Rucaparib, Talazoparib), während sie gegenüber DNA-schädigenden Wirkstoffen empfindlich blieben, was auf einen PARP-spezifischen und DNA-Reparatur-unabhängigen Resistenzmechanismus hindeutet. Der genaue Mechanismus, der der erworbenen Resistenz gegen PARPis in beiden Zelllinien zugrunde liegt, muss jedoch noch ermittelt werden. Nichtsdestotrotz könnte die Beobachtung, dass HR-positive Zelllinien für eine PARPi-Behandlung empfänglich sein können, den potenziellen Behandlungsbereich von PARPis auf Patienten ausweiten, die traditionell aufgrund ihres HR-Status ausgeschlossen wurden.

Zusammenfassend zeigt diese Studie, dass einige HR-positive Zellen für eine PARPi-Behandlung anfällig sein können und dass die erworbene Resistenz in diesen Zelllinien unabhängig von DNA-Reparaturwegen ist.

4. Table of contents

Table of contents

Table of contents

5. List of Figures

List of Figures

6. List of Tables

1. Introduction

1.1 Ovarian Cancer

Ovarian cancer is a heterogeneous disease that affects over 200.000 patients and causes 150.000 deaths worldwide every year. It is the fifth leading cause of cancer-related deaths in women and the most lethal gynecological malignancy [1-3]. The five-year overall survival rate is 47 % and drops below 30 % once the tumor metastasizes [4]. The low overall survival rate is primarily due to late-stage ovarian cancer diagnoses.

Females		
Lung & bronchus	59,910	21%
Breast	43,170	15%
Colon & rectum	24,080	8%
Pancreas	23,930	8%
Ovary	13,270	5%
Uterine corpus	13,030	5%
Liver & intrahepatic bile duct	10,380	4%
Leukemia	9,810	3%
Non-Hodgkin lymphoma	8,400	3%
Brain & other nervous system	7,970	3%
All Sites	**287,740**	**100%**

Figure 1 Ten leading cancer types for the estimated deaths in the United States in 2023, adapted from Siegel et al. 2023

Ovarian cancer can be subdivided into several morphological subtypes according to their cell type: clear-cell carcinomas (5 - 10 %), endometroid carcinomas (10 %), mucinous carcinomas (2-3 %), and serous carcinomas (75 %) [5]. Serous carcinomas can be further divided into High-grade serous ovarian cancer (HGSOC) and Low-grade serous ovarian cancer, where HGSOC accounts for 70 % of all diagnosed ovarian cancers. HGSOC is usually diagnosed at an advanced stage of the disease and is responsible for the majority of ovarian cancer-related deaths [1, 6]. Driver mutations in HGSOC are relatively rare compared to other tumor entities. For example, colorectal cancer has common driver mutations in Adenomatous polyposis coli protein (*APC)*, proto-oncogene *KRAS*, SMAD family member 4 (*SMAD4)*, and tumor protein P53 (*TP53)*, leading to the formation of cancer. HGSOC has only three genes with mutations in the tumor suppressor *TP53* (96 %) and the DNA damage repair genes breast cancer susceptibility 1 and 2 (*BRCA1/2)* (22 %), representing the most common mutations [7]. Furthermore, in 50 % of HGSOC patients, a Homologous recombination deficiency (HRD) is present [8]. Characteristics of different ovarian cancer subtypes are summarized in Table 1.

Risk factors for ovarian cancer are primarily genetic. These include germline mutations in *BRCA1* or *BRCA2*, representing the most common genetic risk factors. Aside from genetic

factors, it has been shown that post-menopausal women who undergo hormone replacement therapy face an elevated likelihood of developing ovarian cancer [6]. On the other hand, there are also factors reducing the risk of developing ovarian cancer, such as giving birth or the use of oral contraceptives [9]. It is also worth mentioning that the different histological subtypes may have different risk factors [10].

Table 1 Characteristics of ovarian cancer by histology, genomic characteristics, and therapies. Adapted from Matulonis, U.A., et al. 2016 [6]

Histological subtype	Clinical findings	Genetic characteristics	Treatment options
High-grade serous carcinoma	• Can present with peritoneal carcinomas, ascites, and/or pelvic mass • Typically, the advanced stage of the presentation	• Deficiencies in homologous recombination (50 % of tumors) • Associated with *BRCA* and *TP53* mutations	• Platinum-based chemotherapy and PARP inhibitors • Tumors are initially sensitive to platinum-based chemotherapy, but most patients with advanced-stage cancer will recur
Low-grade serous carcinoma	• Presents in younger patients • Can be early or late stage at presentation	• Associated with *KRAS* and *BRAF* mutations • Tumors have genomic instability	• MEK inhibitors and hormonal therapy
Low-grade endometrioid carcinoma	• Can be associated with endometriosis	• Associated with *PTEN*, *ARID1A* and *PIK3CA* mutations • Can have microsatellite instability	• Possible hormonal therapies (not yet established)
Clear-cell carcinoma	• Can present with parenchymal metastases (in liver and lungs) • Can be associated with hypercoagulability and hypercalcemia	• Associated with *ARID1A* and *PIK3CA* mutations	• Immunotherapy agents • Can be resistant to platinum-based chemotherapy
Mucinous carcinoma	• Presents in younger patients and is typically in the early stage of presentation	• Associated with *KRAS* mutations	• Tends to be insensitive to chemotherapy but is still treated initially with cytotoxic chemotherapy

1.2 Advancements in Ovarian Cancer Treatment

Despite improved screening strategies for early detection of ovarian cancer, only 20 % of patients are diagnosed at a stage where the tumor remains localized at the ovaries (stage 1). At this stage, up to 90 % of the patients can be cured by cytoreductive surgery followed by a combination of platinum and taxane-based chemotherapy [1]. However, most patients are diagnosed at late stages where the tumor has spread to the pelvic organs (stage 2), the abdomen (stage 3), and beyond the peritoneal cavity (stage 4). Despite a 29 % drop in the

overall cancer death rate in the United States, ovarian cancer-related deaths have remained unchanged for the past three decades [11]. This can be explained mainly by the fact that 87 % of patients are diagnosed at a late stage of the disease, at which the tumor has already metastasized to distant organs, such as the liver, spleen, or pleural effusion containing cancer cells [12]. Second, there is a high likelihood of relapse in patients with metastatic disease driven by drug-resistant cells that drive tumor regrowth despite aggressive therapeutic interventions [5].

1.3 DNA repair pathways

The inability of cancer cells to repair DNA damage is one of the hallmarks of cancer [13, 14]. As discussed in 1.1 HGSOC is characterized by mutations in TP53 and BRCA1/2. In addition to *TP53* and *BRCA* mutations, 50 % of patients have an HRD. These mutational characteristics make HGSOC a perfect candidate for the treatment with DNA-damaging agents, such as platinum-based chemotherapy, or inhibitors targeting HRD, such as poly (ADP-ribose) polymerase (PARP) inhibitors [15, 16].

1.3.1 Single-strand break repair

DNA damage occurs up to 70.000 times in every cell in our body [17]. Single-strand DNA breaks (SSBs) are the most common types of DNA damage, arising more than 10.000 times per cell per day [17]. SSBs can occur through intracellular factors such as increased reactive oxygen species (ROS) levels, spontaneous deamination due to alkylation and replication stress, or extracellular factors such as UV light [18, 19]. Unrepaired SSBs can lead to more severe DNA damage and give rise to DNA double-strand breaks. Therefore, cells have developed several repair pathways to cope with and repair SSBs. These include mismatch repair (MMR), base excision repair (BER), and nucleotide excision repair (NER) [14, 20, 21].

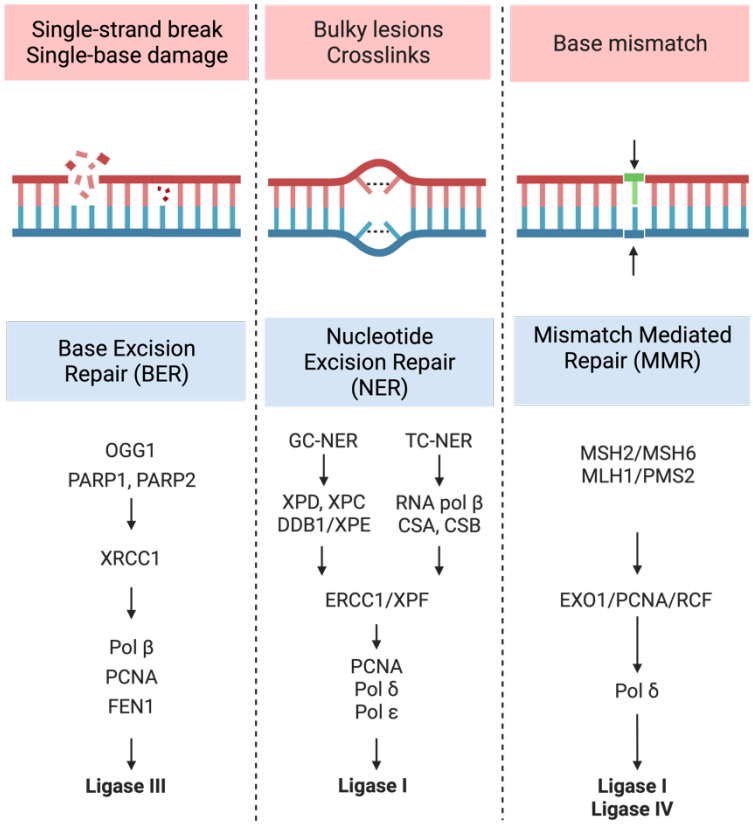

Figure 2 Schematic overview of single-strand break repair pathways.
From left to right, Base Excision Repair, Nucleotide Excision Repair, Mismatch Repair, and its key enzymes.

1.3.1.1 Mismatch repair (MMR)

MMR is a highly conserved cellular process that plays a vital role in maintaining genome integrity. It is responsible for correcting errors during DNA replication, such as base mismatches and insertion or deletion loops (indels). MMR defects can lead to genome instability and elevated levels of microsatellite instability by failing to correct spontaneous mutations. Consequently, MMR ensures the accuracy of DNA replication by identifying and rectifying these discrepancies, thus preventing the accumulation of mutations and the onset of genomic instability. MMR is composed of three stages: initiation, excision, and resynthesis. MutS (DNA mismatch repair protein MutS) homologs recognize single nucleotide mismatches and short indels of up to 4 bases in length [14]. At the resynthesis stage, the DNA is unwound by a helicase and excised by exonuclease I (Exo I), followed by resynthesis via polymerase δ and ligation by DNA Ligase I, with support of the DNA sliding clamp, proliferating cell nuclear antigen (PCNA) [14]. Errors in MMR can have severe effects on genome integrity. For example, microsatellite instability represents a genetic condition that results in hypermutated tumors due to impaired MMR and is associated with several cancers, including ovarian cancer. MMR

defects are linked to the development of Lynch syndrome, an autosomal dominant syndrome that predisposes patients to colorectal, endometrial, and ovarian cancers [14].

Base excision repair (BER)

Like MMR, BER is vital for genome maintenance and functions by correcting altered bases. Cells use BER to repair minor base lesions induced by reactive oxygen species, deamination, or alkylation. Next to small base lesions, BER is also one of the primary repair pathways to repair SSBs in the cell [18]. BER repair pathway is a five-staged process. In the first step, BER glycosylases recognize and remove the damaged bases to form an abasic intermediate. In the second step, BER endonucleases, mostly APE1, make a site incision, resulting in an SSB. The SSB is recognized by PARP1 (the role of PARP1 is explained in more detail at 1.4), which catalyzes poly(ADP) ribose (PAR) chains and recruits X-Ray Repair Cross Complementing 1 (XRCC1). XRCC1 recruits other BER factors to the DNA damage site [20]. In the third step, the DNA backbone is modified by a phosphodiesterase. In the fourth step, the newly formed gap is filled by either DNA Polymerase β, if a short patch, or Polymerases δ or ε, if a long patch. In the final fifth step, the DNA is ligated by DNA Ligase I (long patch) or III (short patch) [14, 20].

1.3.1.2 Nucleotide excision repair (NER)

The NER pathway is highly conserved and is mainly involved in repairing lesions caused by UV light [22]. Defects in the NER pathway are associated with several cancers, like lung, skin, and bladder cancer. Furthermore, NER plays a vital role in ovarian cancer as platinum therapy-induced DNA cross-links are repaired mainly by NER. Therefore, NER can drive resistance to platinum therapy in ovarian cancer [14].

NER can be divided into three steps: 1) damage recognition, 2) dual incisions and release of excision products, and 3) gap filling and ligation. In contrast to BER, NER recognizes double-strand distortions or RNA Polymerase II-stalled lesions. The NER process can be divided into two sub-pathways: global genomic nucleotide excision repair (GG-NER) and transcription-coupled nucleotide excision repair (TC-NER). GG-NER is responsible for detecting and repairing DNA lesions throughout the entire genome, regardless of location. It involves recognizing DNA damage by XPC Complex Subunit, DNA Damage Recognition And Repair Factor (XPC), which acts as a DNA damage sensor. Additional proteins are recruited upon damage recognition, assembling a larger protein complex at the lesion site. This complex includes factors such as XPA, XPG, and transcription factor (TF) IIH that coordinate the incision and removal of the damaged DNA strand on both sides of the lesion. The resulting gap is repaired by DNA

synthesis, facilitated by polymerases δ or ε and DNA Ligases I and III to restore the DNA sequence.

Transcription coupled-NER (TC-NER) is a specialized sub-pathway that specifically targets DNA damage in the actively transcribed regions of genes. It relies on the stalling of RNA Polymerase II at the site of DNA damage, triggering the recruitment of specific factors such as CSA and CSB ubiquitin ligase complex subunits. These factors facilitate the recruitment of NER proteins, ultimately repairing the damaged DNA strand [23].

1.3.2 DNA double-strand break repair

In dividing cells, around ten DNA double-strand breaks (DSBs) occur daily [24]. DSBs are the most dangerous lesions. When left unrepaired, they can accumulate chromosomal rearrangements, disrupt gene function, and ultimately cause cell death via apoptosis. To prevent and secure the stability of the genome, DSBs can be repaired by two major repair pathways: homologous recombination (HR) and end joining pathways. End-joining pathways can be further divided into canonical non-homologous end joining (NHEJ) and alternative end joining (alt-NHEJ) [25-27].

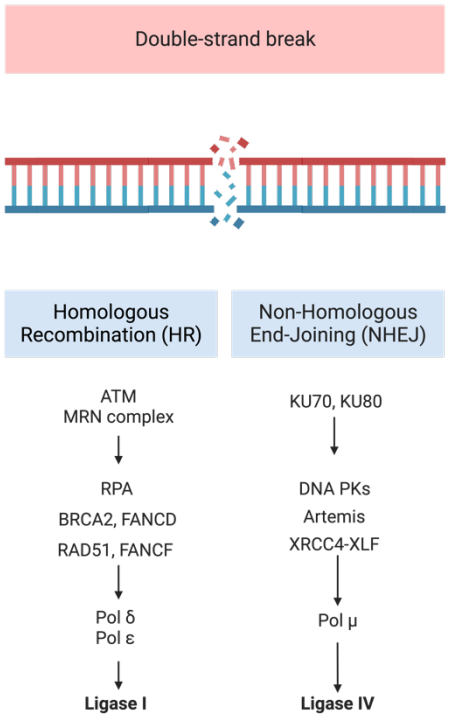

Figure 3 Schematic overview of DNA double-strand break repair.
From left to right, Base Excision Repair, Nucleotide Excision Repair, and Mismatch Repair and its key enzymes.

1.3.2.1 Non-homologous end joining (NHEJ)

DSBs occur throughout the cell cycle and are predominantly repaired outside the S and G2 phases by NHEJ since NHEJ is not dependent on the presence of a homologous sequence [26]. Defects in NEHJ lead to sensitivity to ionizing radiation [28].

In NHEJ, the DSB is detected and recognized by the KU70-KU80 heterodimer, which binds to the DNA and recruits other repair enzymes to the damaged site. DNA-dependent protein kinase catalytic subunits (DNA-PKcs) bind to the heterodimer and form a DNA-PK complex. Usually, the two ends of the DSBs are incompatible with each other. To resect the DNA ends, the endonuclease Artemis is recruited and activated by DNA-PKcs. In the case of non-ligatable DNA ends, DNA Polymerase λ and μ fill up the gaps. The final step of NHEJ is ligating the two strands by the XRCC4-XLF complex and DNA Ligase IV [26-28].

1.3.2.2 Homologous recombination (HR)

HR is the most accurate DNA repair mechanism. It requires sizeable homologous DNA sequences to repair the damaged DNA region. As HR relies on the presence of homologous sequences, HR is limited to the cell cycle phases in S- and G2 when homologous sister chromatids are available [25, 29]. Initially, the ends of DSBs are recognized and processed by DNA end resection to generate 3´- single-strand overhangs. The MRN complex, including MRE11 homolog, MRE11, RAD50, and Nibrin (NBS1) initiate DNA end resection. MRE11 has a single-strand endonuclease activity and a 3'-5' exonuclease activity on stranded DNA, but it requires CtBP-interacting proteins (CtIP) for its endonuclease activity. RAD50 and MRE11 form the core of the MRN complex and facilitate DNA tethering for the complex. NBS1 does not have enzymatic activity, but it is crucial for recruiting ATM to DSB sites. The single-stranded DNA is subsequently bound by the DNA-directed RNA polymerase I subunit complex (RPA1, RPA2, and RPA3), protecting the binding with other single-stranded DNA molecules. To further proceed with HR, the RPA proteins are removed from the DNA to allow the binding and formation of the RAD51 filament. BRCA2 displaces the RPA molecules and loads RAD51 onto the DNA. After RAD51 filament formation and strand invasion, one or two Holiday Junctions are formed by engaging one or both ends of the DSB. Afterward, RAD51 is removed from the DNA by RAD54, and the 3' end serves as the starting point for DNA synthesis by DNA polymerase δ or polymerase ε using the intact DNA strand from the sister chromatid as a template. The Holiday Junction is resolved, and the DSB is repaired error-free [27, 30, 31].

1.4 PARP1

The poly (ADP-ribose) polymerase family has 18 members today [32]. As the name already indicates, the PARP family members are enzymes transferring ADP-ribose(s) onto target proteins. This molecular process of ADP ribosylation is a post-transcriptional modification by which ADP-ribose units are added to target proteins' Glu, Asp, and Lys residues. The single PARPs are in their function different from each other. For example, not all PARPs can transfer multiple ADP ribose molecules to target proteins [33]. Therefore, the PARP family can be subdivided into four subgroups based on their domain architecture (Figure 4). The most prominent subfamily are the DNA-dependent PARPs: PARP1, PARP2, and PARP3, which bind DNA molecules with their DNA-binding domain [32, 34, 35].

PARP1 was the first identified member of the PARP family and is a highly conserved protein among eukaryotes [36]. PARP1 consists of three main domains: an amino-terminal DNA-binding domain, which comprises of three zinc finger domains, a nuclear localization signal, a BRCT domain containing a central auto modification domain, and a carboxy-terminal catalytic domain [37].

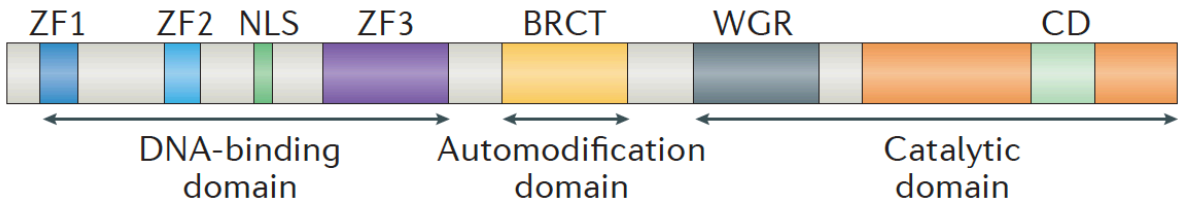

Figure 4 Molecular structure of PARP1.
ZF, zinc finger domain; NLS, nuclear localization signal; BRCT, BRCA1 C terminus; WGR, Trp-Gly-Arg domain; CD, catalytic domain. Adapted from Ray Chaudhuri, A. and A. Nussenzweig [38]

PARP1 is a versatile protein involved in multiple cellular processes such as chromatin remodeling, transcription, stabilization of replication forks, sensing of unlighted Okazaki fragments during replication, inflammation, and metabolism [32, 39-41]. Besides all these functions, PARP1 is mainly known for its role in DNA repair.

In response to DNA damage, PARP1 uses Nicotinamide adenine dinucleotide (NAD+) to synthesize a linear or multibranched polymer of ADP ribose on itself, as auto modification, or on other target proteins [32]. The vital role of PARP1 in DNA repair has been demonstrated in PARP1-deficient mouse models, which appeared to be hypersensitive to alkylating agents and ionizing radiation [42].

1.4.1 The role of PARP1 in single-strand break repair

DNA damage occurs frequently in every cell in our body. Therefore, cells have developed several mechanisms to repair DNA damage and thus maintain the integrity of their genome. Of the different types of DNA damage that occur in cells, SSBs are the most common, arising at a frequency of up to 1000 times per cell per day [21].

One key enzyme in the SSB repair pathway is PARP1. When a single-strand DNA break occurs, PARP1 senses the site of DNA damage and binds to the DNA. PARP1 starts to synthesize several hundred negatively charged, branched PAR chains on itself and other target proteins [43, 44]. These branched PAR chains serve as a scaffold for other DNA repair enzymes, particularly X-ray repair cross-complementing protein 1 (XRCC1) [40]. The binding of PARP1 onto the DNA is transient because self-modified PARP1 is rapidly released from DNA, and PAR chains can also be degraded by poly(ADP-ribose) glycohydrolase (PARG) [45].

1.4.2 The role of PARP1 in the repair of DSBs

It has been shown that PARP1 is involved in the recruitment of meiotic recombination 11 (MRE11) to DSBs, in line with Mre11 having a putative PAR binding domain [46]. Furthermore, there is evidence that PARP1 is also involved in recruiting BRCA1 to sites of DSBs [47]. However, there are multiple PARP1-independent ways for BRAC1 to be recruited to DSBs, such as DNA damage-mediated ubiquitylation [48].

In the case of NHEJ, it has been shown in *in vitro* studies that PARP1 can PARylate the DNA-dependent protein kinase catalytic subunit (DNA-PKcs), which is a crucial enzyme in NHEJ, and stimulate the kinase activity of DNA-PKcs [49].

1.4.3 Replication fork reversal and processing

Stalled replication forks occur upon replication stress and protect the cells from replicating damaged DNA. At stalled replication forks, single-stranded DNA is exposed, which leads to the recruitment of PARP1 to the stalled replication fork. The ATP-dependent DNA helicase Q1 (RECQ1) is essential for the restart of a stalled replication fork [50]. RECQ1 can bind to PARylated PARP1, which inactivates the helicase activity of RECQ1 that prevents the restart of the stalled replication fork, allowing DNA repair [50]. The relationship between PARP1 and RECQ1 at the initiation of a stalled replication fork may also account for the observed phenomenon where inhibition of PARP leads to uncontrolled restart of stalled replication

forks due to the potential overactivity of RECQ1. This restarting can result in the accumulation of unrepaired lesions and fork collapse, leading to the formation of DSBs [38, 50].
Furthermore, PARP1 seems necessary to restart stalled replication forks by recruiting MRE11 [51]. MRE11 induces end resection at stalled replication forks, allowing the repair of DNA lesions. However, it has been shown that PARP1 prevents end resection at stalled forks by MRE11[52].

1.5 PARP inhibitors

In 2015, a new class of drugs, termed PARP inhibitors, were approved by the American Food and Drug Administration (FDA) and European Medicines Agency (EMA) for the treatment of ovarian cancer patients. They were approved as monotherapy for the maintenance treatment of patients who are either sensitive to platinum, carry a *BRCA1/2* mutation, or are diagnosed as HGSOC. In 2005, two groups showed a synthetic lethality between the inhibition of PARP1 in the presence of *BRCA1* or *BRCA2* mutations [53, 54]. The concept of synthetic lethality was described in 1922 by Calvin Bridges; he observed that when crossing fruit flies (*D. melanogaster*), some combinations of non-lethal mutations resulted in lethality [55]. Twenty years later, the term synthetic lethality was coined by Theodore Dobzhansky [56, 57].

The first approved PARPi was olaparib in 2015. In phase I and II clinical trials, over 60 % of the patients carrying a *BRCA1/2* mutation showed a clinical benefit to olaparib treatment [58-61]. In 2017, the next PARPi, niraparib, was approved by the FDA and EMA for the treatment of ovarian cancer patients showing sensitivity to platinum therapy [62]. In 2018, rucaparib was approved by the FDA and EMA as a single agent for HGSOC patients carrying a BRCA1/2 germline or somatic mutation [62]. A timeline of PARPis and their discovery is shown in Figure 5. However, as observed with many other targeted therapies, most patients with advanced ovarian cancer develop resistance to PARPi treatment [15, 63]. In addition to late-stage diagnosis when the tumor has already metastasized, the development of treatment resistance poses significant challenges in the management and cure of ovarian cancer patients.
Consequently, it is crucial to gain insights into the molecular mechanisms underlying resistance to PARPis and to identify strategies for overcoming acquired resistance. Multiple combination therapy approaches are currently being explored to enhance the effectiveness of PARPi treatment. These strategies involve combining PARPi with ATR Serine/Threonine

Kinase (ATR) [64, 65], Checkpoint Kinase 1 (CHK1) inhibitors [66], and WEE1 G2 Checkpoint Kinase inhibitors (WEE1) [67].

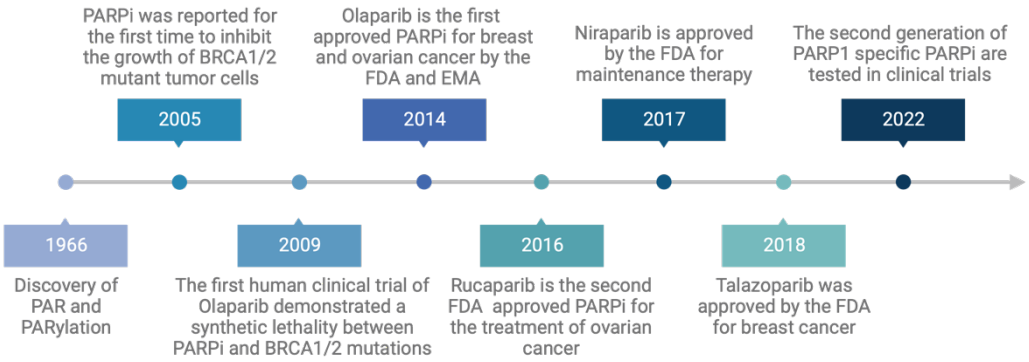

Figure 5 Timeline of the discovery and clinical approval of PARPis.
The figure was adapted from [68]

1.5.1 Molecular mechanism of PARP inhibition

In the initial two publications on PARPis by Farmer and Bryant in 2005, they proposed a hypothesis suggesting that the inhibition of PARP1 prevents the repair of SSBs, leading to the accumulation of unrepaired lesions. These unrepaired lesions were thought to give rise to DSBs during the progression of DNA replication forks [53, 54]. However, contrary to their hypothesis, subsequent research demonstrated that the depletion of PARP1 did not increase SSBs [68].

These findings led to a new hypothesis explaining the molecular basis of PARPi - induced toxicity in HR-deficient cells. This hypothesis is based on the trapping potential of PARPis, suggesting that they function by trapping PARP1 onto the DNA, resulting in DNA-protein cross-links. These cross-links lead to the collapse of replication forks during the S-phase of the cell cycle, ultimately resulting in the accumulation of DSBs. Significantly, in HR-deficient cells, these DSBs cannot be efficiently repaired error-free (see Figure 7) [41]. The trapping hypothesis is also supported by the finding that PARylation is necessary to release PARP1 from DNA, indicating that PARP-DNA complexes can form and be resolved through active PARylation [69]. Different PARPis exhibit different levels of cytotoxicity, even though their capacity to inhibit the catalytic domain of PARP1 is quite similar among them [70, 71]. The trapping potencies of several PARPis are illustrated in Figure 6, with talazoparib exhibiting the most potent PARP trapping potency. Talazoparib is 100 times more potent than niraparib, which is followed by olaparib, rucaparib and veliparib [15, 70].

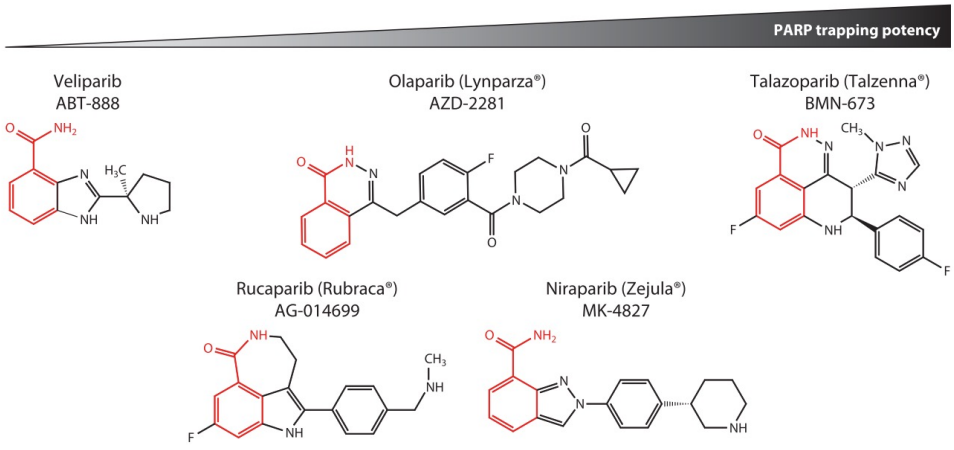

Figure 6 Clinical PARPi ranked by potency for PARP trapping.
The red portions of the molecules correspond to the aminobenzamide group that binds to the NAD+ pocket of PARPs. The commercial names of the FDA-approved PARPi are indicated in parentheses, adapted from [70].

In line with these various trapping potencies, PARPis also differ in their allosteric effect. Talazoparib (the strongest trapper) prevents the release of PARP1 from the DNA. In contrast, rucaparib, niraparib, and veliparib promote the release of PARP1 from the DNA, potentially explaining the difference in their pharmacological potency [72]. Consistent with these findings, it is conceivable that the maximum-tolerated dose of PARPis decreases as trapping potential levels increase [73].

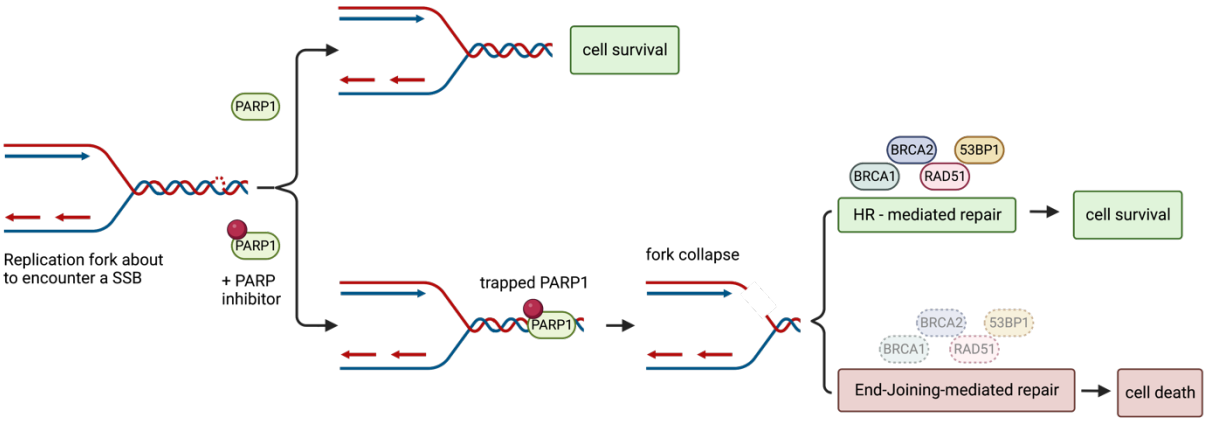

Figure 7 PARPis and their mode of action.
PARPi were believed to block PARylation, inducing cytotoxicity. However, subsequent discoveries revealed that the primary cause of tumor cell death stemmed from the trapping of PARP1 enzyme at SSBs. While PARP1 repairs SSBs, its trapping poses a risk to replication forks during the S phase of the cell cycle. This ultimately leads to the collapse of the replication fork, giving rise to DSBs. In cells proficient in HR, these DSBs were repaired error-free. In contrast, cells lacking one of the key HR proteins (BRCA1, BRCA2, RAD51, 53BP1) depend on error-prone repair pathways, the end-joining pathways (NHEJ & alternative end-joining), to repair DSBs. The dependency of error-prone pathways results in the accumulation of chromosomal aberrations and cell death, adapted from [41].

1.6 Resistance to PARP inhibitors

Although PARPis have demonstrated promising responses in clinical trials, most patients are faced with resistance to the treatment. Several resistance mechanisms to PARPis have been identified in the last years. Resistance to PARPi treatment can occur through three general mechanisms: restoration of HR, drug target-related effects, or loss of DNA end-protection / restoration of replication fork protection (reviewed here [41, 74, 75]). These three general mechanisms are explained in the following sections.

1.6.1 PARP inhibitor resistance through the restoration of HR

The most common resistance mechanism to PARPi treatment is restoring HR by a second mutation in *BRCA1* or *BRCA2*, re-inducing the expression of the wild-type proteins. This mechanism was initially found and described in a *BRCA2* mutant ovarian and pancreatic cancer cell line upon prolonged treatment with PARPi or cisplatin treatment [76, 77]. In the last years, several studies described secondary mutations as the reason for acquired PARP inhibitor resistance [78] in patients with ovarian [77, 79-84], breast [79, 83, 85], pancreatic [86] and prostate cancer [87, 88]. Similar secondary mutations in HR genes have been identified in patients carrying a mutation in *RAD51C*, *RAD51D*, and Partner and localizer of BRCA2 (*PALB2*) [81, 88]. These reversion mutations can be found in approximately 20-25 % of patients with acquired PARPi resistance [80].

Besides restoration of HR via secondary mutations in essential pathway proteins, other mechanisms exist to restore HR repair in *BRCA1/2* mutant cells. One of these mechanisms is a loss of NHEJ by a mutation in TP53-binding protein 1 *53BP1*, which counteracts the effect of BRCA1 loss on HR and genomic stability. More specifically, the loss of 53BP1 restores DNA-end resection during the first step in HR, shifting the balance towards HR [89, 90]. However, the loss of 53BP1 does not restore HR in *BRCA2* mutant cells, indicating a different role of BRCA1 and BRCA2 in HR [89, 91]. In line with the restoration of HR via the loss of 53BP1, other studies identified downstream proteins of 53BP1 (RIF1, REV7, DYNLL1, and the shieldin complex (SHLD1, SHLD2, SHLD3, and REV7)), which also restore end-resection [91-95]. On the other hand, other mechanisms promoting HR and thereby suppressing NHEJ have been identified. For example, overexpression of Thyroid Hormone Receptor Interactor 13 (TRIP13) in BRCA1 deficient cells can dissemble the REV7-REV3 complex [96], and the upregulation of micro-RNA 622 in *BRCA1* mutant cells suppresses NHEJ by downregulating the expression of the KU complex proteins [97].

1.6.2 PARP inhibitor resistance through drug target-related effects

One of the first identified mechanisms of PARPi resistance was the upregulation of the drug efflux transporter ABCB1 [98, 99]. ABCB1 belongs to the ATP binding cassette (ABC) transporter family, which has been identified as the source of resistance for multiple chemotherapy and other agents by transporting the molecules out of the cell and preventing the accumulation of the substance in the cell [100, 101]. This acquired resistance to PARPi can be reversed by co-treatment with ABCB1 inhibitors, for example, tariquidar. However, ABCB1 inhibitors have severe side effects and are therefore unsuitable for clinical use [102, 103]. To avoid ABCB1-driven resistance, several PARPis, including veliparib, niraparib, and pamiparib, were developed and designed as poor substrates for ABCB1 [104, 105]. As most patients are pretreated with chemotherapies such as taxanes and doxorubicin that can induce upregulation of ABCB1, these PARPis may represent a promising and effective option [98].

The current PARPis have in common that they target the catalytic domain of PARP1 and compete there with the substrate NAD+ [106]. Therefore, resistance to PARPis could also arise from mutations within the NAD binding domain of PARP1. Such a mutation can potentially reduce the affinity to the inhibitor or catalytic function of PARP1 [107]. It should also be mentioned that such PARP1 mutations can only lead to resistance in HR-proficient cells or in cells with a hippomorphic BRCA1 activity due to the synthetic lethal effect of a combined loss of PARP1 and BRCA1 [41].

Another drug target-related resistance mechanism is the loss of poly(ADP-ribose) glycohydrolase (PARG). PARG functions by removing PAR chains from target proteins. Loss of PARG is considered to restore the PARylation of target proteins, thus inducing DNA repair and reducing PARP1 trapping onto the DNA [108].

1.6.3 PARP inhibitor resistance through the restoration of fork stability

While restoration of HR function is only limited to cells carrying a BRCA1 mutation, acquired resistance to PARPis due to restoration of the replication fork is a common mechanism in both BRCA1 and BRCA2 deficient cells. The function of BRCA1 and BRCA2 is not restricted to DNA damage repair, but both enzymes play an essential role in protecting and stabilizing replication forks. For example, in the absence of BRCA1/2, the nucleases MRE11 and MUS81 perform uncontrolled end-resection of the stalled replication fork, leading to a collapse of the replication fork [38, 52]. The depletion of either the protein complex PTIP or the nucleosome

remodeling factor Chromodomain-helicase-DNA-binding protein 4 (CHD4) hinders the recruitment of MRE11 to stalled replication forks. This leads to fork protection and resistance to PARPi in BRCA1/2 deficient cells [38, 109]. In addition, the chromatin remodeling factor SWI/SNF Related, Matrix Associated, Actin Dependent Regulator Of Chromatin, Subfamily A Like 1 (SMARCAL1) has also been identified to promote MRE11 end-resection in BRCA1/2 deficient cells; therefore, depletion of SMARCAL1 decreases the sensitivity to PARPi in BRCA1/2 mutant cells [110].

1.7 Strategies to overcome PARPi resistance

One strategy to overcome PARPi resistance is surgical debulking of the remaining tumor after a determined treatment period, which might reduce or eliminate resistant clones. However, this approach is more theoretical since ovarian cancer patients are mostly diagnosed at late stages, and post-therapy debulking surgery is rarely performed due to the reduced fitness of the patients [12].

Further strategies to overcome PARPi resistance aim at increasing the anti-tumor effects of PARPi by increasing the vulnerability of cancer cells to DNA damage. Some promising approaches and strategies are discussed in the following section.

1.7.1 Combination strategies to overcome PARPi resistance

Over the past few years, research has illustrated that BRCA1 is not solely essential for DNA-end resection within HR. It also plays a role in recruiting the BRCA2-PALB2 complex to facilitate the assembly of RAD51 filaments mediated by BRCA2. Additionally, in cells lacking BRCA1, PALB2 is recruited in a BRCA1-independent manner using Ring Finger Protein 168 (RNF168) [111, 112]. These findings indicate that the reactivation of HR in BRCA1 and 53BP1 deficient cells is made possible through RNF168 dependent recruitment of PALB2, resulting in enhanced DNA end-resection [113, 114]. In line with this discovery, the absence of RNF168 suppresses HR in BRCA1/53BP double-deficient cells, making these cells susceptible to PARPi treatment once again [112]. Consequently, targeting the RNF168-dependent recruitment of PALB2 emerges as a potential strategy to sensitize BRCA1 and 53BP double-deficient cells to PARPi treatment.

A second factor that has gained attention over the past years is the DNA repair protein RAD52. The simultaneous depletion of RAD52 and BRCA1/2 leads to a phenomenon called synthetic lethality, suggesting that RAD52 serves as an alternative pathway for recruiting RAD51 to

processed DNA ends when BRCA1/2 are absent [115, 116]. Furthermore, subsequent research has revealed that RAD52 also plays a role in repairing single-stranded DNA at stalled replication forks and facilitates fork reversal [117]. The synthetic lethality observed upon RAD52 loss in combination with BRCA1/2 deficiency might be attributed to the combined effects of both functions of RAD52. Notably, RAD52 inhibitors have been developed and demonstrated synergistic effects when combined with PARPis [118].

In addition to directly targeting proteins involved in HR, there is an alternative approach to induce "HRDness" (the suppression of HR by non-HR genes) by inhibiting signaling pathways that promote HR repair. Multiple studies have demonstrated that signaling pathways such as androgen receptor (AR), RAS, and PI3K-AKT can stimulate HR repair like Bromodomain-containing protein 4 (BRD4). Inhibiting BRD4 has been shown to reduce the transcription of several crucial DNA damage response (DDR) genes, including *CTIP*, *BRCA1*, *RAD51*, *TOPB1*, and *WEE1*, resulting in HR deficiency [119, 120]. Consequently, targeting these pathways may offer a viable strategy to induce HR deficiency and re-sensitize PARPi-resistant cells to PARPi treatment [121].

Additionally, it has been established that inhibiting proteins unrelated to DNA repair, such as EGFR, IGF1R, and VEGF, can disrupt DNA repair through HR [122]. Combining the VEGF antagonist bevacizumab with PARPi olaparib or niraparib has shown notable improvements in progression-free survival in two cohorts of ovarian cancer patients, including patients with proficient HR, compared to patients treated with placebo or PARPi monotherapy [123, 124].
Another potential strategy to overcome acquired resistance to PARPis involves targeting the cell-cycle checkpoint signaling pathways. These pathways are primarily governed by two key enzymes, ATM and ATR, which regulate cell-cycle activation and enforce cell-cycle arrest in response to DNA damage [125, 126]. ATR plays a significant role in processes related to fork protection and BRCA1-independent steps within the HR pathway, such as loading RAD51 onto damaged DNA and stalled replication forks [127]. Current investigations explore combination therapies involving ATR and PARPis, particularly in BRCA1-deficient patients with restored HR function or enhanced fork protection [128, 129].
In the event of an upregulation of the drug efflux pump ABCB1, as discussed in section 1.6.2 potential strategy to counteract this upregulation is administering an ABCB1 inhibitor. Besides

this combination strategy, a more promising approach could involve the usage of second-generation PARPis that do not serve as substrates for ABCB1 and other drug efflux pumps. One example of these second-generation PARPis is pamiparib, which is approximately 16-fold more potent than olaparib and specifically designed to avoid transportation by drug efflux transporters such as ABCB1 [104].

2. The aim of this dissertation

Ovarian cancer, particularly HGSOC, is a highly aggressive and often lethal disease with a poor prognosis when diagnosed in its advanced stages [1, 2]. In 2014, Olaparib, the first PARPi, was approved as a maintenance therapy for ovarian cancer patients sensitive to platinum, BRCA-mutated, or diagnosed with HGSOC [16]. However, most patients experienced only a modest increase in overall survival due to the development of resistance to PARPi treatment [41, 130]. This fact underscores the importance of intensive research to identify and understand the molecular mechanisms responsible for PARPi resistance to improve treatment outcome.

The primary aim of this thesis was to identify a new resistance mechanism to PARPi treatment. Therefore, I used patient-derived, serum-free cultured, ovarian cancer cell lines and applied them to a long-term treatment regimen to generate PARPi-resistant cell lines. This approach helped mitigate unwanted serum-induced side effects and to simulate clinical treatment scenarios.

Next, I utilized transcriptional and genomic approaches such as RNA-, Whole Exome, and Whole Genome Sequencing to identify potential candidates inducing PARPi resistance in ovarian cancer cell lines. To investigate the role of potential resistance-inducing genes, I performed CRISPR Cas9-based knockouts to analyze whether their depletion could re-sensitize olaparib-resistant cells to PARPi treatment.

Additionally, I characterized the PARPi-resistant cell lines based on molecular approaches such as cell proliferation assay, cell cycle state, cell viability assays, colony forming assays, and DNA repair capacity of the cell lines. Ultimately, I attempted to overcome olaparib resistance by combining it with inhibitors of the NAD+ synthesis pathway based on the findings obtained in this thesis.

In total, this thesis should enhance our understanding of PARPi resistance and show potential ways to overcome acquired resistance.

3. Material & Methods

3.1 Cell culture of primary cell lines

Primary patient-derived cell lines were cultured in tumorMACS supplemented with ovarian cancer supplement (#130-119-483, Miletnyi Biotech) on Corning® Primaria™ dishes or flasks at 37°C and 5 % CO2. The medium was exchanged twice a week.

Passaging of cells was performed by dissociating the cells with Accutase (A11105, Thermo Fisher). Cells were collected with COBG medium (CO_2-independent medium (#18045088 Thermo Fisher), supplemented with 1 % BSA and 2 mM L-glutamine) and centrifuged at 300 x g for 5 min at RT. The cell pellet was resuspended in 1 ml of tumorMACS medium and seeded in a fresh dish/flask at 1:20 (OC12) and 1:10 (OC14).

For cell counting, the CytoSMART Exact Cell Counter was used.

For cryopreservation, cells were dissociated and collected as described above and, after centrifugation, resuspended in 500 µl CryoStor (#C2874-100, Sigma) per vial. Vials were transferred to Mr. Frosties and stored at -80°C overnight. For long-term storage, cells were stored in liquid nitrogen.

Table 2 Patient-derived ovarian cancer cell lines used in this study with diagnosis, origin, and treatment data.

Cell line	diagnosis	origin	treatment
OC12	Adenocarcinoma of the ovary	ascites	Cyclophosphamide, Adriamycin, and cisplatin
OC14	serous adenocarcinoma	ascites	1st line Carboplatin/Taxol, 2nd line Caelyx (doxorubicin) after Platinum resistance 3rd line Topotecan, Catumaxomab (CD3 & EpCAM Ab) & Gemcitabine
OC15	serous adenocarcinoma	ascites	1st line 6 cycles Carboplatin & Taxol 2nd line Topotecan
OC19	serous adenocarcinoma	tumor	not treated
OC20	serous adenocarcinoma	pleural effusion	1st line Carboplatin, Paclitaxel 2nd line Carboplatin, Gemcitabine, Bevacizumab
OC22	serous adenocarcinoma	tumor	not treated
PE306	serous adenocarcinoma	ascites	1st line 6 cycles of Carboplatin & Paclitaxel 2nd line 6 cycles of Carboplatin & Paclitaxel Platin resistance
Asc211	serous adenocarcinoma	ascites	1st line 6 cycles of Carboplatin, Paclitaxel & Bevacizumab 2nd line 6 cycles of Carboplatin, Doxorubicin, Bevacizumab 3rd line Topotecan

Cells were thawed in a 37°C warm water bath, and the thawed cell suspension was transferred into a 15 ml tube and slowly filled up to 10 ml with pre-warmed COBG medium and centrifuged at 300 x g for 5 min at RT. Cells were resuspended in 1 ml of tumorMACS supplemented with ovarian cancer supplement, and cells were seeded in Corning® Primaria™ flasks or dishes.
Cell lines were routinely tested for mycoplasma contamination and analyzed by single-nucleotide polymorphism (Multiplexion & Eurofins Genomics).

3.2 Generation of PARPi (olaparib) resistant Ovarian cancer cell lines

The basal cell lines were split into six flasks to obtain olaparib-resistant cell lines. Three were treated with olaparib (S1060, Selleckchem), and the other three replicates with DMSO (D2650, Sigma) as vehicle control. Each flask was treated for 4 days (medium was replaced after 48 h) with indicated doses of olaparib or DMSO, followed by a drug holiday period until the cells reached 90 % confluency. The same drug concentrations were administered simultaneously to three biological replicates of each cell line. This procedure was repeated for 11 (OC12) / 15 (OC14) rounds with increasing doses of olaparib, as shown in Table 3

Table 3: Olaparib concentrations at each treatment round during the treatment regimen

Treatment round	Olaparib concentration OC12	Olaparib concentration OC14
1	1 μM	3 μM
2	1 μM	3 μM
3	1.5 μM	3 μM
4	2 μM	4 μM
5	2.5 μM	4.5 μM
6	3 μM	5.5 μM
7	4 μM	6.5 μM
8	5 μM	10 μM
9	10 μM	15 μM
10	15 μM	20 μM
11	20 μM	20 μM
12	-	22.5 μM
13	-	22.5 μM
14	-	22.5 μM
15	-	22.5 μM

3.3 Western blot analysis

3.3.1 Preparation of whole cell lysate

Cells were cultured in Corning® Primaria™ (#35846, Corning) 6 well plates. Protein lysis buffer was prepared with the following reagents:

10x RIPA buffer	100 µl
100x AEBSF	10 µl
100x EDTA	10 µl
100x Protease an Inhibitor Cocktail	10 µl
H2O	870 µl
Total:	1000 µl

The culture medium was removed, and wells were washed once with ice-cold PBS. For lysis, 100 µl Protein lysis buffer was added per 6-well and incubated for 5 min on ice and scraped using a cell-scraper. The cell suspension was transferred to a pre-cold 1.5 ml tube followed by 15 min incubation on ice. To remove any cell debris, the cell lysates were centrifuged at 17,000 x g for 15 min at 4°C. The supernatant was transferred into a new pre-cooled 1.5 ml tube and for long-term storage, stored at -80°C.

3.3.2 Preparation of the nuclear fraction

The protocol for nuclear fractionation is based on [131]. Cells were cultured in Corning® Primaria™ (#35846, Corning) 6 well plates. After the designated treatment, the medium was removed, and 500 µl Accutase was added to detach the cells. Once the cells were detached, they were resuspended in 1 ml of ice-cold PBS and centrifuged at 300 x g for 5 min at 4°C. Afterwards, the cells were washed in 1 ml ice-cold PBS. After the washing step, the PBS was aspirated, and the pellet was resuspended in 100 µl ice-cold hypotonic buffer (Table 4) and incubated for 3 min on ice. In order to lyse the cell-membrane NP-40 was added to a final concertation of 1 % and incubated for 3 min on ice and centrifuged at 1000 x g for 5 min at 4°C to separate the nuclei (pellet) and cytoplasmatic (supernatant) fraction.

Nuclear fraction: the pellet was resuspended in 150 µl isotonic buffer (Table 5) containing NP-40 with a final concentration of 0.3 % and incubated for 10 min on ice. After incubation, the solution was centrifuged at 1000 x g at 4°C for 3 min. The supernatant was transferred to a fresh tube and sonicated two times for 10 sec at an amplitude of 10 %.

Cytoplasmatic fraction: the supernatant was centrifuged at maximum speed for 3 min at 4°C. The supernatant was transferred to a fresh tube and labeled as cytoplasmatic fraction.

Table 4 Compounds of hypotonic buffer for nuclear fractionation

20 mM Tris-HCl (pH 7.4)
10 mM KCl
2 mM $MgCl_2$
1 mM EGTA
0.5 mM DTT
0.5 mM PMSF

Table 5 Compounds of isotonic buffer for nuclear fractionation

20 mM Tris-HCl (pH 7.4)
150 mM KCl
2 mM $MgCl_2$
1 mM EGTA
0.5 mM DTT
0.5 mM PMSF

3.3.3 Preparation of chromatin-bound fraction

For each precipitation, 5 Mio cells were seeded in a T75 Primaria™ flask (#353810, Corning). After the experiment, the cells were detached from the flask by adding 3 ml of Accutase. Afterward, cells were resuspended in 7 ml PBS and centrifuged at 300 g for 5 min at 4°C. The cell pellet was washed 2 times with ice-cold PBS, resuspended in 1 ml of lysis buffer (Table 6), and incubated for 30 min on ice. After incubation, the lysed cells were centrifuged at high speed for 10 min at 4°C. The supernatant (cytoplasmatic fraction) was discarded, and the pellet (nuclei) was resuspended in 200 µl low salt buffer (Table 7), incubated for 15 min on ice, and centrifuged as described before. The supernatant (nuclear soluble fraction) was discarded, and the pellet was washed with 200 µl low salt buffer (Table 7) and centrifuged as described in the previous step. The pellet was then resuspended in 75 µl 0.2 M HCl, incubated for 20 min on ice, and centrifuged as described before. The supernatant (chromatin-fraction) was transferred to a new, pre-chilled tube, and 75 µl 1 M Tris-HCl (pH 8) was added to neutralize the acid.

Table 6 Composition of lysis buffer for chromatin-bound fraction

10 mM HEPES pH 7.6
10 mM KCl
0.05 % NP-40
Supplemented with phosphatase and protease inhibitor cocktail

Table 7 Composition of low salt buffer for chromatin-bound fraction

10 mM HEPES pH 7.6
10 mM KCl
0.05 % NP-40
Supplemented with phosphatase and protease inhibitor cocktail

The following steps were performed for all protein fractions described above

Protein concentration was determined using the Pierce™ BCA Protein Assay (#23255, Thermo Fisher Scientific) or Qubit™ Protein Assay (#Q33211, Thermo Fisher Scientific), following the manufacturer's instructions. Protein lysates were usually diluted in a 1:10 ratio.

For protein denaturation, 2x protein buffer was prepared as follows:

10x Reducing agent (TCEP)	200 µl
4x NUPage LDS sample buffer	500 µl
H_2O	300 µl
Total:	1000 µl

Aiming a 1µg/µl protein concentration, 500 µg protein was mixed with 250 µl H_2O and 250 µl of 2x protein buffer and incubated at 72°C for 10 min. Afterwards, samples were stored at -20°C or, for loading, they were put on ice.

For western blot analysis, the BioRad Laboratories System was used. 4 – 20 % Criterion™ TGX Stain-Free™ protein gels (#5678094, BioRad) were put into a gel chamber filled with 1 L running buffer (100 mL 10X Tris/glycine/SDS (TGS)/NUPage + 900 mL MilliPore water). 20 µg protein lysate was loaded onto the gel, and 10 µL Spectra™ Multicolor Broad Range Protein Ladder (#26634, Thermo Fisher) was used as molecular weight standard. Gel was run at 100 V for ~90 min. After the run was finished, the gel was removed from the cassette.

For protein transfer, the gel and PVDF membrane (Trans-Blot® Turbo™ Midi PVDF Transfer Packs, #1704157, BioRad) were assembled inside the Trans-Blot Turbo transfer system cassette. For this purpose, the membrane was activated in 100 % methanol for 1 min until the membrane was translucent and washed in Turbo-Blot transfer buffer (100 mL 5X Turbo-Blot transfer buffer + 100 mL 100 % ethanol + 300 mL H_2O). Transfer stacks were soaked in transfer buffer and put into the blotting cassette. The transfer sandwich was assembled as follows (from bottom to top): bottom (+) cassette, bottom ion reservoir stack, blotting membrane, protein gel, top ion reservoir stack, and top (-) cassette electrode. The transfer was run applying the program 'Mixed (or High) Molecular Weight' for 7-10 min.

Afterward, the membrane was blocked in 5 % BSA-Tris-buffered saline (TBS) with 0.05 % Tween 20 (TBST-T) for 1 h at RT or overnight at 4°C seesawed. Primary antibodies were diluted in appropriate blocking buffer and incubated on membranes overnight at 4°C seesawed. Primary antibodies in the working solution were supplemented with 0.01 % final concentration of sodium acetate and stored at -20°C. The membrane was washed thrice with 1x TBS-T for 10 min each. The secondary HRP-coupled antibodies were diluted 1:10,000 in blocking buffer and added to the membrane, followed by an incubation time of 1h at RT on a rocker. Secondary antibodies were discarded, and membranes were washed three times with 1X TBS-T again for 10 min each. 2 mL Clarity (Max) Western ECL substrate was prepared by mixing 1 mL of each part in the kit (#170506 0/2, BioRad) and applied to the membrane. The chemiDoc-imaging system was used to acquire colorimetric and chemiluminescent images of blots. Image Lab software (v. 6.0) was used for image acquisition and analysis.

Table 8 Primary antibodies used for Western blot analysis

Primary antibodies	Isotype	Dilution	kDa	Product number	Producer
ABCB1	Rabbit IgG	1:1000	130-180	#13978	Cell Signaling Technologies
ATM	Rabbit IgG	1:1000	350	#2873	Cell Signaling Technologies
α-Tubulin	Mouse IgG	1:1000	52	#3873	Cell Signaling Technologies
BRCA1	Rabbit IgG	1:1000	220	ab9141	Abcam
DNA ligase IV	Rabbit IgG	1:1000	104	GTX55592	GeneTex
Histon H3	Rabbit IgG	1:10.000	15	ab1791	Abcam
Mre11	Rabbit IgG	1:5000	81	NB100-142	Novus Biologicals
PARP1	Rabbit	1:1000	116	#9532T	Cell Signaling Technologies
Phospho-ATM (Ser1981)	Rabbit IgG	1:1000	350	#13050	Cell Signaling Technologies
Poly/Mono-ADP Ribose	Rabbit	1:1000		#83732	Cell Signaling Technologies
Rad51	Rabbit IgG	1:5000	36	ab176458	Abcam
XRCC4	Rabbit IgG	1:1000	38	GTX109632	GeneTex
53BP1	Rabbit IgG	1:2000	250	NB100-305	Novus Biologicals

Table 9 Secondary antibodies used for western blot analysis

secondary antibodies	Isotype	Dilution	Product number	Producer
Anti-rabbit IgG, HRP-linked Antibody	Rabbit	1:10.000	#7074	Cell Signaling Technologies
Goat Anti-Mouse IgG1-HRP	Mouse	1:10.000	#1071-05	Biozol

3.4 Virus production using PEI and Sodium Chloride

On the day before transfection, HEK293T cells were seeded in T150 cell culture flasks in DMEM supplemented with 10 % FCS and incubated at 37°C, 5 % CO2 overnight. On the day of transfection, the optimal confluency of cells was roughly 80 %. The medium was aspirated and replaced by DMEM supplemented with 10 % heat-inactivated FCS and 25 μM chloroquine. For this purpose, FCS was heat-inactivated at 52°C for 1 h before being added to the medium.

On the day of transfection, the three plasmids (pMD2.G, pSPAX2, and the plasmid of interest) are prepared in a 1:1:1 equimolar ratio, aiming for a total plasmid concentration of 1,05 μg/ml. The plasmid mix was prepared by mixing the three plasmids with 1.5 M NaCl (final concentration of 200 μM); for the PEI mix, PEI (1 μg/μl) was mixed with 1.5M NaCl (final concentration of 200 μM) and water to reach a final PEI concentration of 5,5 μg of PEI per 1 μg of DNA. The plasmid- and PEI mix were mixed by vortexing for 10 sec, followed by an incubation time of 15 min at RT. In the meantime, the medium was carefully aspirated and replaced with 20 ml/flask of fresh DMEM supplemented with 10 % FCS. After 15 min, the total volume of the transfection mix was added to the flask and distributed by gently swirling the flask. Twelve hours post-transfection, the medium was carefully aspirated and replaced by 20 ml of freshly prepared collection medium (DMEM supplemented with 10 % heat-inactivated FCS, 4 mM Caffeine, and 1 mM Sodium butyrate). 48 h post-transfection, the virus collection medium was harvested and filtered using a Millipore™ Stericup™ Quick Release-HV Vacuum Filtration System 0.45 μm (#S2HVU02RE, Merck Millipore). The filtered collection medium was transferred to autoclaved, sterile Beckman tubes (#326823, Beckman Coulter) and centrifuged at 25.000 rpm for 2 h at 4°C in an ultracentrifuge. Afterward, the supernatant was aspirated, and the remaining liquid was carefully removed with clean paper wipes. The pellet was resuspended in a 500 x concentrated volume of PBS. The virus was aliquoted at 20 μl and stored at -80°C.

3.4.1 Virus Titer by Flow Cytometry

In order to determine the virus titer, 50,000 OC12 or OC14 cells were seeded in a Corning® Primaria™ (#35846, Corning) 6 well plate. On the next day, the medium was aspirated, and fresh tumorMACS supplemented with ovarian cancer supplement (#130-119-483, Miletnyi) and 10 μg/mL polybrene (#TR-1003, Sigma) was added to cells. 10 μl virus was added in a 1:10 dilution series to the cells in duplicates. The medium was changed 14 h after transduction. 72 h post-transduction, cells were harvested as usual and analyzed by flow cytometry. Transfection efficiency and virus titer were calculated according to the following formula:

$$Titer\ (TU\ per\ ml) = (N * P)/(V * D)$$

N = cell number at Day 2

P = percentage of positive cells (should be 10-20 %)

V = virus volume used for infection in each well (here: V(ml) = 20 (µl) x 10^{-3})

D = dilution fold

TU = transduction unit

3.4.2 Virus Titer by Cell count

In order to determine the virus titer, 50,000 cells were seeded in Corning® Primaria™ (#35846, Corning) 6 well plate. The medium was aspirated the next day, and fresh TumorMACS™ Medium supplemented with ovarian cancer supplement and 10 µg/mL polybrene (#TR-1003, Sigma) was added to cells. 10 µl virus was added in a 1:10 dilution series to the cells in duplicates. The medium was changed 14 h after transduction and replaced with medium containing puromycin at the respective concentration. Cells were incubated for 4 to 6 days, and medium was replaced every second day with a fresh medium containing puromycin. After puromycin selection, cells were harvested as usual and counted. Transfection efficiency and virus titer were calculated according to the following formula:

$$Titer\ (TU\ per\ ml) = N * D * 50$$

N = cell number per well

50 (depends on the volume of virus dilution added to 1ml of the medium; 20 µl in 1 ml = 50x)

D = dilution fold

TU = transduction unit

3.5 Quantitative Real-Time PCR (qRT-PCR)

Cells were cultured in Corning® Primaria™ (#35846, Corning) 6 well plates. For RNA isolation, 700 µL QIAzolo® lysis reagent was added to the cells and incubated for 5 min at RT. Afterwards, lysed cells were transferred into a 1.5 mL tube and snap-frozen in liquid nitrogen. Samples were stored at -80°C until RNA isolation. Following the manufacturer's protocol, total RNA was extracted using the miRNeasy Mini kit (#217004, Qiagen). In all cases, optional DNAse digest was performed according to instructions in Appendix D of the handbook. According to the manufacturer's instructions, RNA concentration and quality were determined using Nanodrop

or Qubit 3.0 fluorometer (Thermo Scientific). RNA was reverse-transcribed using the high-capacity cDNA reverse-transcription kit (#4374966, Applied Biosystems) according to the manufacturer's instructions. 60 ng of synthesized cDNA in triplicates was a template for quantitative real-time polymerase chain reaction (RT-qPCR) analysis. TaqMan™ gene expression assays using the Fast Advance Master Mix and according to dual-labeled TaqMan™ probes (see Table 10) were used in order to acquire gene expression data with the VIIA7 Real-Time PCR or QuantStudio™ 5 Real-Time PCR Systems (Thermo Scientific). The ΔΔCt method was applied to calculate samples' relative fold gene expression. Acquired Ct-values for genes of interest were normalized to the geometric mean of up to three housekeeping genes (RPL13A, POLR2A, and PPIA). In order to obtain the relative fold gene expression of each target, ΔCt-values were normalized to the respective ΔCt-values of the control sample. The QuantStudio™ Design and Analysis software (v. 1.4.3) was used for data acquisition, and Microsoft Excel was used for data analysis. Data were further analyzed using GraphPad Prism9 (Version 9.3.1 or newer). Statistical differences between the two groups were detected using an unpaired two-tailed Student's t-test.

Table 10 TaqMan probes used for qRT-PCR

TaqMan Probe	**Assay ID**
ABCB1	Hs00184500_m1
APLF	Hs01063873_m1
POLR2A	Hs00172187_m1
PPIA	Hs99999904_m1
TBP	Hs00427620_m1
Twist1	Hs00361186_m1

3.6 CRISPR-Cas9 mediated knockout

Ovarian cancer cells were cultivated and detached from flasks as described in (3.1). For a single reaction, 1 x 10^6 cells were used. The crRNA for target genes was designed and ordered from IDT, and electroporation was applied using the NEPA21 electroporator from Nepagene according to the manufacturer's protocol.

The gene-specific Alt-R CRISPR-Cas9 crRNA (200 μM, IDT) and Alt-R CRISPR-Cas9 tracrRNA (200 μM, IDT) were mixed in equimolar ratio and heated up to 95°C for 5 min to form a crRNA:tracrRNA duplex. The annealed gRNA was allowed to cool down to reach RT. To form the RNP complex, 4 μl of the gRNA was mixed with 5 μl of Cas9 Nuclease (61 μM, IDT) and

incubated at RT for 20 min. To the 9 µl RNP mix, 16 µl of Opti-MEM™ (#10149832, Gibco) was added. 1x10^6 cells were resuspended in 100 µl Opti-MEM™, and 10 µl RNP complex was added and mixed carefully. 100 µl of the cell/RNP suspension was dispensed into an electroporation cuvette (2 mm gap) and remixed by tapping the cuvette with a finger. The cells were then electroporated with the following settings:

Poring Pulse:	Transfer Pulse:
• 125 V	• 20 V
• 5 ms (length)	• 50 ms (length)
• 50 ms (interval)	• 50 ms (interval)
• 2 pulses	• 5 pulses
• 10 % D. Rate	• 40 % D.Rate

After successful electroporation, cells were transferred into a 6-well Primaria™ plate with pre-warmed tumorMACS ovarian cancer medium and cultured for 24 – 48 h. The validation of the Knockout efficiency was either performed by Western Blot analysis or Sanger sequencing of the target region see (3.3 or 0).

Table 11 guide RNAs for CRISPR-Cas9 mediated gene knockout

Target gene	**Exon**	**Position**	**Sequence (5’ to 3’)**	**PAM**
ABCB1	3	87,600,161	GATCTTGAAGGGGACCGCAA	TGG
ABCB4	4	87,462,857	TATGTCGCTGGGTACCATCA	TGG
APLF	5	68,513,637	TCAGTACCAGCAATCAGTGG	AGG
EPCAM	2	47,373,527	GTGCACCAACTGAAGTACAC	TGG
TWIST	1	19,117,320	CGCGTCGCCGCTCGAGAGAT	TGG

3.7 Sanger Sequencing

Genomic DNA was extracted from Ovarian cancer cell lines using the DNAeasy Blood and Tissue Kit (# 69504, Qiagen) according to the manufacturer's instructions, including RNAse digest. DNA quality and quantity were determined using NanoDrop (Thermo Scientific). In order to determine the knockout efficiency of CRISPR cas9 KO experiments (3.6), the region surrounding the target site was amplified by PCR using Q5 hot start high-fidelity 2x master mix (#M0492, New England Biolabs Inc.) according to the manufacturer's instructions. PCR and Sanger Sequencing Primer were summarized in Table 12. PCR products were purified by PCR Purification Kit (#28104, Qiagen) according to the manufacturer's instructions. Sanger sequencing was performed at Eurofins Genomics. Knockout efficiency was determined using the ICE CRISPR Analysis Tool, comparing DNA sequences of wild-type/non-targeting and knockout samples [132]

Table 12 PCR and Sanger sequencing primers

Target gene	**Application**	**Direction**	**Sequence (5' to 3')**
APLF	PCR/sequencing	Forward	TCTAGAGGCTGGGTGGTGATCT
	PCR/sequencing	Reverse	ACCCTCTTATTGTGCTGGCCTT
Twist	PCR/sequencing	Forward	CCGTTGGGCGCTTTCTTTTT
	PCR	Reverse	TCTTGCTCAGCTTGTCCGAG
ABCB1	PCR	Forward	GCTTCTTGAGGCGTGGATA
	PCR	Reverse	GCGACCAACACCACTTGAAA
	Sequencing	Forward	CTTCGTGGAGATGCTGGAGA
	Sequencing	Reverse	ATTCCAAAGGCTAGCTTGCG
ABCB4	PCR	Forward	AGAGGAGAAATTCCATTCCACA
	PCR	Reverse	CAACTCCCAAATTTTTACCCAG
	Sequencing	Forward	AGAGGAGAAATTCCATTCCACA

3.8 Cell titer Blue™ (CTB) assay, drug titration

For the Cell titer Blue™ assay, ovarian cancer cells (for cell numbers, see Table 13) were seeded in Corning® Primaria™ (#353872, Corning) 96 well plates. 24 h after seeding, individual compounds (see Table 14) and the corresponding vehicle control were titrated in quadruplicates in a 1:3 serial dilution. 10 μM staurosporine (S1421, selleckchem) was used as dead control to determine the background signal. After 72 or 120 h (medium change after 72 h), cell viability was assessed by addition of 20 μl/well CTB reagent (#G8081, Promega) and incubation for 2 – 3 h. Metabolic activity was measured by fluorescence signal (555/585 nm) at a SpectraMax iD3 microplate reader (Molecular Devices). The surviving fraction of drug-treated cells was normalized to values from the DMSO-treated control. Relative cell viability values were plotted using GraphPad Prism software.

Table 13 Cell numbers for CTB assay

Duration of the experiment	**OC12**	**OC14**
72 h	2.500 cells/well	6.000 cells/well
120 h	1000 cells/well	3.000 cells/well

Table 14 List of compounds used in experiments of this thesis

Compound	**Catalog number**	**Producer/distributor**
Olaparib (AZD2281)	S1060	Selleckchem
Rucaparib (AG014699)	S4948	Selleckchem
Talazoparib (BMN 673)	S7048	Selleckchem
Paclitaxel (NSC 125973)	S1150	Selleckchem
Zosuquidar (LY335979)	S1481	Selleckchem
Elacridar (GF120918)	S7772	Selleckchem
Pamiparib (BGB-290)	S8592	Selleckchem
Daporinad (FK866)	S2799	Selleckchem

3.9 Crystal Violet (CV) assays

For crystal violet assay, Corning® Primaria™ (#353872, Corning) 96 well plates from CTB assay were further used for cell confluency measurements. After CTB measurement, plates were washed with PBS (#D8537, Sigma) and fixed for at least 24 h in 10 % Formalin (Sigma). After fixation, plates were washed with H_2O and stained for 30 min with 100 µl/well CV (V5265, Sigma). Upon CV removal, plates were washed with H_2O, dried, and CV was dissolved with 100 µl/well 10 % Acetic acid (#320099, Sigma). CV absorbance was measured at 600 nm in a SpectraMax iD3 microplate reader (Molecular Devices). The data were normalized as described for the CTB assay (3.8). Relative cell confluency curves were plotted using GraphPad Prism software.

3.10 Colony forming assay

For colony forming assay, cells (for numbers, see Table 15) were seeded in a Corning® Primaria™ (#353847, Corning) 24 well plates. 24 h after seeding, cells were treated with drugs at varying concentrations, including DMSO control (corresponding to the highest drug concentration) treatment, for 96 h with refreshed treatment after 48 h. After treatment, drug treatment was removed, and media was replaced to enable cells to recover for 48 h under drug-free conditions. After 6 days, cells were washed with PBS and fixed in 10 % Formalin for at least 24 h and subsequently stained with 500 µl CV per well as described above. The plates were imaged using a ChemiDoc imaging system (BioRad).

Table 15 Cell numbers for Colony forming assay

Duration of the experiment	**OC12**	**OC14**
7 days	1,000 cells/well	R#1: 3,000 cells/well R#2 & 3: 5,000 cells/well S#1, 2, 3: 2,000 cells/well

3.11 Whole Exome Sequencing

Genomic DNA was extracted from Ovarian cancer cells using the DNAeasy Blood and Tissue Kit (# 69504, Qiagen) according to the manufacturer's instructions, including RNAse digest. DNA concentration was determined using a Qubit 3.0 Fluorometer (Thermo Scientific). Whole Exome Sequencing (WES) was performed using the SureSelect XT HS Human All Exon V7 kit (#5191-4028, Agilent) following the manufacturer's instructions. The final libraries were pooled in an equimolar manner (10 nM) and submitted for sequencing at the Genomics and Proteomics Core Facility of the German Cancer Research Center (GPCF, DKFZ) and sequenced on an Illumina NextSeq 550 PE 150bp High Output. The Omics IT and Data Management performed alignment of sequences to the reference genome - Core Facility (ODCF DKFZ) using bwa mem aligner [133]. Single nuclear variants and Indels were called from bam files using the SureCall NGS software from Agilent. Copy number variations were celled using CNVkit [134].

3.12 Whole Genome Sequencing

Genomic DNA was extracted from Ovarian cancer cells using the DNAeasy Blood and Tissue Kit (# 69504, Qiagen) according to the manufacturer's instructions, including RNAse digest. The DNA concentration was determined using a Qubit 3.0 Fluorometer (Thermo Scientific). The library preparation of the genomic DNA was performed using the TruSeq DNA Nano kit from Illumina (# 20015964, Illumina) following the manufacturer's instructions. The final libraries were pooled in an equimolar manner (10 nM) and submitted for sequencing at the Genomics and Proteomics Core Facility of the German Cancer Research Center (GPCF, DKFZ) and sequenced on an Illumina NovaSeq 6000 PE 150bp S4. The Omics IT and Data Management performed alignment of sequences to the reference genome - Core Facility (ODCF DKFZ) using bwa mem aligner [133]. Single nuclear variants and Indels were called from bam files by the ODCF following the pipeline as described in [135].

3.13 RNA-seq

Cells were cultured under specific treatment and control conditions (RNA expression under drug treatment) or without treatment (RNA expression after treatment regimen). Cells were cultured in Corning® Primaria™ (#35846, Corning) 6 well plates.

For RNA isolation from Ovarian Cancer cell lines, 700 µL QIAzolo® lysis reagent was added to the cells and incubated for 5 min at RT. Afterwards, lysed cells were transferred into a 1.5 mL tube and snap-frozen in liquid nitrogen. Samples were stored at -80°C until RNA isolation. Total RNA was extracted from Ovarian cancer cells using the miRNeasy Mini kit (#217004, Qiagen) following the manufacturer's protocol. In all cases, optional DNAse digest was performed according to instructions in Appendix D of the handbook. RNA concentration was determined using Nanodrop (Thermo Scientific), and the quality of extracted RNA (RIN) was determined on a Bioanalyzer (Agilent Technologies) using the RNA 6000 Pico Assay (#5067-1513, Agilent Technologies). Library preparation was performed using the TruSeq® Stranded mRNA Library kit (#20020594, Illumina), following the manufacturer's instructions. Final libraries were pooled equimolar (10 nM) and submitted for sequencing at the Genomics and Proteomics Core Facility of the German Cancer Research Center (GPCF, DKFZ) and sequenced on an Illumina NovaSeq 6k PE 100bp S4. The Omics IT and Data Management core facility (ODCF DKFZ) used the STAR to align sequences to the reference genome [136].

Differential gene expression analysis was performed using DESeq2 [137]. According to the empirical Bayes method, we first applied an unpaired t-test (two-tailed) to determine statistical significance ($P < 0.05$) and performed Benjamini Hochberg correction to identify differentially expressed genes with an adjusted p-value < 0.05.

Gene set enrichment analysis (GSEA) was performed on normalized counts using the GSEA Java Desktop Application (Version 4.1.0 Broad Institute). Differentially enriched gene sets provided by the Molecular Signature Database (MSigDB, release v2022.1.Hs) were used.

3.14 Alkaline Comet Assay

Cells were irradiated at 4 Gy and harvested by Accutase treatment after indicated time points after irradiation. For early time points (15 min after irradiation), cells were harvested before irradiation and kept in tumorMACS ovarian cancer medium. 2.5 x10^5 cells were resuspended in 500 µl PBS (500 cells/µl), 50 µl of the cell suspension was mixed with 350 µl low-melting agarose, and 60 µl of the suspension was spread on comet slides (#4250-200-03, Biozol

Diagnostica) and set on a metal rack placed on ice. After 10 min, the slides were placed in a glass chamber filled with lysis buffer (2.5 M NaCl, 10 mM Trizma®-Base, 100 mM Na_2-EDTA, 1 % N-Lauryl sarcosine Na-Salt) and incubated overnight, protected from light at 4°C. The next day, the electrophoresis chamber was placed on ice and filled with Electrophoresis buffer (300 mM NaOH, 1.15 mM Na_2-EDTA). Comet slides were placed and fixed by a drop of electrophoresis buffer to the surface of the chamber and carefully overlaid with electrophoresis buffer, incubated for 20 min, and afterwards subjected to electrophoresis at 25 Volt and 300 mA for 20 min. Comet slides were afterward fixed with abs. Ethanol for 10 min at RT. For staining, 50 µl of a 0.01 % SYBER Green solution (#4250-050-05, Biozol) was dropped onto each sample and incubated for 20 min at RT. Afterwards the slides were mounted with 50 µl mounting solution (200 µl VECTASHIELD® mounting solution (#VEC-H-1000, Biozol) + 800 µl 0.01 % SYBER Green solution). Images were acquired using a Leitz, Laborlux 11 microscope, Olive Tail moments (an arbitrary-unit measure of DNA strand breaks: Tail DNA content in % x Tail Moment Length) from 200 cells per sample were scored blinded using automated Comet Assay software "Kinetic Imaging Komet version 6.0".

3.15 Immunofluorescence (IF) staining

Cells were cultured on comet slides and either irradiated (4 Gy) or treated with different drugs with specific concentrations and duration. After the treatment, cells were washed with PBS and fixed with 4 % PFA for 15 min at RT. Cells were washed for 5 min in PBS at RT, permeabilized with 0.15 % Triton X-100 in PBS for 10 min at RT, and blocked with blocking buffer (1.5 % BSA, 20 mM glycine in PBS) for 30 min at RT. Cells were then incubated with primary antibody (see.

Table 16). Therefore, 60 µl of the antibody solution (prim. Antibody in PBS) was pipetted onto each sample and incubated at 4°C overnight. The following day, the slides were washed for 5 min in PBS and permeabilized again with 0.15 % Triton X-100 in PBS for 5 min at RT, followed by blocking for 5 min at RT. After blocking, slides were incubated with goat anti-rabbit or goat anti-mouse Alexa Fluor 488 or 594 (Invitrogen) for 1 h, protected from light at RT, and washed again for 5 min in PBS. DNA was stained for 3 min with DAPI (1.5 µg/ml DAPI in PBS) and mounted with Fluoromount-G® (#0100-01, SouthernBiotech). Images were acquired fully automated using a Zeiss Axioplan 2 microscope. RAD51 and γH2AX foci were automatically counted with the Metafer4 V3.1.3 software (MetaCyte).

To enhance visualization of the microscopy images in the results section, I applied the Unsharp Mask filter in Adobe Photoshop (version 13.0 20120315.r.428 2012/03/15:21:00:00) x64) with the following settings: Amount at 333 %, Radius set to 4.1 Pixels, and a Threshold of 75 levels.

Table 16 List of primary and secondary antibodies used for IF

antibody	**fluorophore**	**IgG**	**dilution**	**producer**
Anti yH2A.X	-	mouse	1:250	#05-636-I, Merck
Anti yH2A.X	-	rabbit	1:1000	#ab2893, abcam
Anti-Rad51	-	rabbit	1:1000	#PC130, Merck
Goat anti-mouse IgG (H+L) Cross-Adsorbed Secondary Antibody	Alexa 594	Goat IgG	1:1000	# A-11005 Thermo Fisher
Goat anti-rabbit IgG (H+L) Cross-Adsorbed Secondary Antibody	Alexa 488	Goat IgG	1:1000	# A-11008 Thermo Fisher

3.16 Flow cytometry

For FACS and flow cytometry analysis, cells were harvested as described XX, the cell pellet was resuspended in FACS buffer (PBS supplemented with 1 % BSA and 2mM EDTA), and the cell number was determined. Up to $1x10^7$ were resuspended in 100 µl FACS buffer containing fluorophore-labeled antibodies of interest or isotype control (Table 17) and incubated for 1 h at 4°C in the dark. After labeling, cells were washed with excessive FACS buffer and centrifuged at 300 g for 5 min at 4°C and resuspended in 150 µl FACS buffer containing live/dead cell markers (1:1000 PI or 0,15 µg/ml DAPI). Analyses were performed at LSR II, Fortessa, or Canto II flow cytometers (BD Biosciences). Data analysis was performed with FlowJo™ 10 Software and GraphPad Prism (Version 9.5.1) software.

FACS experiments were performed using a BD FACS Aria I, II, or III flow cytometer (BD Biosciences) at the Cytometry DKFZ Core Facility

3.16.1 Annexin V staining

The number of apoptotic cells was measured and quantified by detecting phosphatidylserine externalization using an Annexin V FITC and PI kit (#556547, BD) following the manufacturer's instructions. In Brief, cells were cultured in 6-well Primaria™ plates as described before and treated with indicated concentrations of olaparib or DMSO for 72h. After treatment, cells and

the medium were collected, washed in ice-cold PBS resuspended in Annexin V binding buffer, stained with Annexin V – FITC and PI at room temperature, and analyzed immediately afterward. Analysis was performed using FlowJo™ 10 Software and GraphPad Prism (Version 9.5.1) software.

3.16.2 Cell cycle analysis using 5-Brom-2'-deoxyuridine (BrdU)

Cells were cultured in 6-well Primaria™ plates and treated with indicated concentrations of olaparib or DMSO. At specific time points, cells were treated for 2 h with 10 μM BrdU, afterwards harvested and fixed in ice-cold 70 % ethanol and kept in the dark until all samples were collected. Fixed cells were pelleted at 4.000 rpm for 2 min (centrifugation settings remained the same for the following centrifugation steps) and permeabilized in 500 μl 2 N HCl, 0.5 % Triton X-100 and incubated for 30 min at RT. Cells were again centrifuged and resuspended in 500 μl 0,1 M sodium tetraborate and incubated for 2 min, followed by centrifugation. Cells were once washed with 150 μl PBS supplemented with 1 % BSA, centrifuged, and resuspended in 50 μl PBS supplemented with 0.5 % Tween-20, 1 % BSA, and 20 μl anti-BrdU antibody; cells were incubated for 1 h at RT. After incubation, cells were pelleted and resuspended in 200 μl PBS supplemented with 10 μg/ml RNase A (12091-021, Invitrogen) and 20 μg/ml PI (P3566, Thermo Fisher) and transferred to FACS tubes; incubated for 30 min at RT in the dark. Analysis was performed at an LSR II (BD Biosciences), and data were further analyzed using FlowJo™ 10 Software and GraphPad Prism (Version 9.5.1) software.

Table 17 Antibodies used for Flow cytometry

antibody	fluorophore	IgG	dilution	producer
Anti-Annexin V	FITC		5 μl per test	51-65874X, BD Biosciences
Anti BrdU	FITC	mouse	20 μl per test	51-33284X, BD Biosciences
CD243 (ABCB1)	APC	recombinant	2 μl per test	130-124-449, Miltenyi Biotech
Isotype	FITC	mouse IgG1		11-4714-42, e.Bioscience
Isotype	APC	Mouse IgG1		17-4714-42, e.Bioscience

3.17 Seahorse Assay

The Agilent Seahorse Mito Stress assay (#103015, Agilent) assessed mitochondrial respiration activity. To measure the oxygen consumption rate (OCR) and extracellular acidification rate (ECAR), three molecules targeting different complexes of the mitochondrial electron transport chain were serially injected: oligomycin, carbonylcyanide-4 (trifluoromethoxy) phenylhydrazone (FCCP), and rotenone/antimycin A. Using this method, it is possible to measure multiple parameters simultaneously, including basal and maximal respiration activity, spare respiratory capacity, ATP production, and non-mitochondrial respiration.

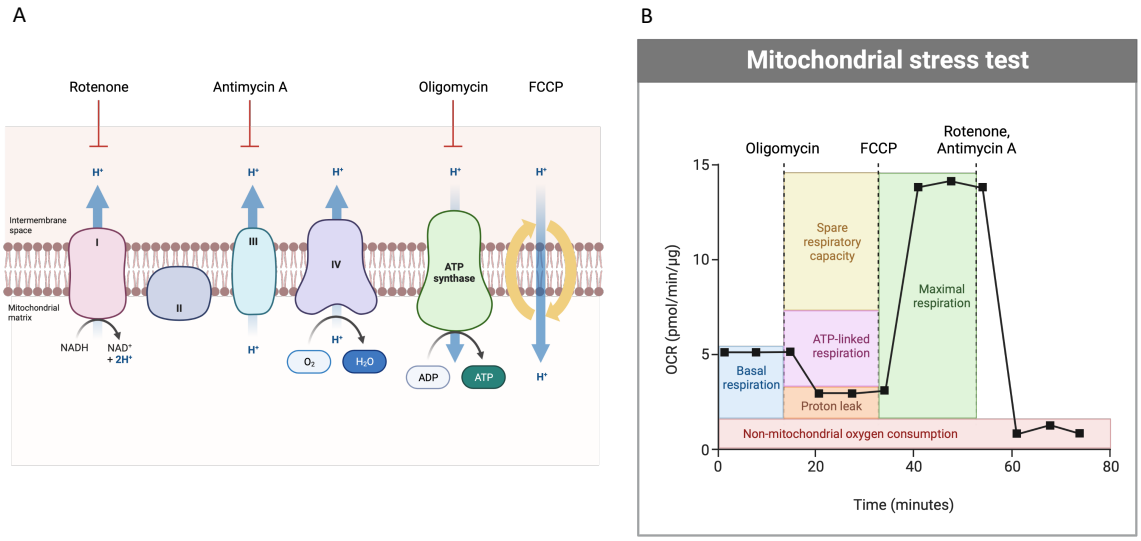

Figure 8: Overview of Seahorse XF Mito Stress Assay.
A The schematic illustrates the inhibitors rotenone, antimycin A, oligomycin, and FCCP, which target different mitochondrial electron transport chain complexes. **B** The figure shows the Seahorse XF Cell Mito Stress Test profile measuring oxygen consumption rate (OCR). After three measurements of basal OCR, oligomycin is injected into cells, inhibiting ATP synthase, complex V of the electron transport chain, reducing OCR. After each injection, three measurements are performed. Second, the uncoupling agent carbonylcyanide-4 (trifluoromethoxy) phenylhydrazone (FCCP) is injected, disrupting the mitochondrial membrane potential. Third, a mixture of rotenone and antimycin A targeting complex I and III is injected, shutting down mitochondrial respiration. Based on these measurements, parameters including basal respiration, ATP-linked respiration, proton leak, maximal respiration, spare capacity, and non-mitochondrial oxygen consumption are calculated.

For detailed protocol, the manufacturer's instructions were followed. Before the assay day, the sensor cartridge was hydrated in sterile water (200 µL/well); the Seahorse XF calibrant solution was incubated at 37°C in a non-CO2 incubator overnight. Cells were seeded at specific cell numbers in Seahorse Xfe PDL cell culture plates (#103730-100, Agilent). The cells were pre-incubated at 37°C in a non-CO2 incubator overnight before the assay. On the assay day, the water from the sensor cartridge was discarded and filled with pre-warmed Seahorse XF calibrant solution (200 µL/well). The assembled sensor cartridge and utility plate were placed at 37°C in a non-CO2 incubator for 45-60 minutes before loading the injection ports of the sensor cartridge. The Seahorse XF Cell Mito Stress Assay medium was prepared as follows:

100 ml	Seahorse XF DMEM
1 ml	1 mM Pyruvate
1 ml	2 mM Glutamine
400 µl	10 mM Glucose

The Seahorse XF assay medium was pre-warmed in a water bath at 37°C, and the pH was adjusted to 7.4 using a 0.1 M NaOH solution. The medium was sterile filtered and kept at 37°C until needed for the assay. The corner wells of the plate were filled with medium and were used as a reference for background measurements. The remaining wells were filled to a final 180 µL/well volume with assay medium. Subsequently, cells were incubated at 37°C in a non-CO2 incubator for 20 minutes. Meanwhile, stock compounds were prepared by resuspending them in the pre-warmed assay medium as follows:

Compound	Assay medium
Oligomycin	630 µl
FCCP	720 µl
ROT/AA	540 µl

Three 15 mL tubes were prepared and filled with 2.7 mL pre-warmed assay medium each. To one vial each, 300 µL of each compound was added. 20 µL/well of oligomycin (final concentration: 1.5 µM) was pipetted to port A, 22 µL/well of FCCP (final concentration: 1 µM) was added to port B, and 25 µL/well of ROT/AA (final concentration: 0.5 µM) was pipetted to port C using a multichannel pipette. The sensor cartridge was placed in a non-CO2 incubator at 37°C until the run was started. The Seahorse Xfe 96 Extracellular Flux Analyzer (Agilent) and the WAVE software were used to measure the Mito Stress assay, and data analysis was performed automatically by WAVE. GraphPad Prism9 (Version 9.3.1) was used for data analysis. The normality of the data distribution was assessed using the Shapiro-Wilk normality test, and data were considered normally distributed if the significance level (alpha) was more significant than 0.05. Statistical differences between the two groups were determined using an unpaired two-tailed Student's t-test. For non-parametric data distribution, the Mann-

Whitney U-test was used. Statistical significances were denoted by * for $p < 0.05$, ** for $p < 0.01$, *** for $p < 0.001$, and ns for non-significant.

3.18 Measurement of intracellular NAD levels

The NAD/NADH Glo™ Assay (Promega, G9071) was used to analyze intracellular NAD levels. In short, the NAD/NADH glo reagent contains the NAD cycling enzyme, which converts NAD+ to NADH. In the presence of NADH, the enzyme reductase reduces a pro-luciferin reductase substrate to form luciferin, which can be measured with a luminometer.

The assay was performed following the manufacturer's protocol. Before the assay, cells were seeded in a 96-well Primaria™ plate, as described before. The next day, cells were treated with 10 μM olaparib for 24 h. After incubation, the intercellular NAD analysis was performed with 15 μl of NAD/NADH-Glo reagent in a 384-well plate (Cat.# 3570, Corning). Luminescence was measured with an integration time of 0.5 seconds on a SpectraMax iD3 microplate reader (Molecular Devices).

3.19 Traffic light reporter assay

The cells were infected with pCVL Traffic Light Reporter 1.1 (Sce target) Ef1a Puro lentivirus at a low MOI of 1 and selected with puromycin for successful transduction. Selected cells were transduced with pCVL.SFFV.d14GFP.EF1a.HA.NLS.Sce(opt).T2A.TagBFP, pRRL sEF1a HA.NLS.Sce(opt).T2A.IFP, or pRRL SFFV d20GFP.T2A.mTagBFP Donor (Table 18) virus at different MOIs (0 - 100). 72 h after transduction, GFP and mCherry fluorescence was analyzed in BFP-positive cells using LSR II, Fortessa, or Canto II flow cytometers (BD Biosciences).

Table 18 Plasmids used for traffic light reporter assay

plasmid	distributor
pCVL Traffic Light Reporter 1.1 (Sce target) Ef1a Puro	addgene
pCVL.SFFV.d14GFP.EF1a.HA.NLS.Sce(opt).T2A.TagBFP	addgene
pRRL sEF1a HA.NLS.Sce(opt).T2A.IFP	addgene
pRRL SFFV d20GFP.T2A.mTagBFP Donor	addgene

4. Results

4.1 Screening eight ovarian cancer cell lines for olaparib sensitivity

As outlined in the aims (chapter 2), this thesis aimed to investigate PARPi resistance in patient-derived ovarian cancer cell lines. The cell lines used in the thesis (OC12, OC14, OC15, OC19, OC20, OC22, PE306, and Asc211) were established by my former colleague Dr. Steve Wagner [138] (detailed information about each cell line can be found in Table 2). The initial step was to screen the patient-derived cell lines for sensitivity or resistance to PARPi treatment. To achieve this, I performed drug titration assays (described in section 3.8) where I treated the cells for five consecutive days with eleven different concentrations of olaparib, ranging from 10 nM to 500 µM, alongside corresponding concentrations of DMSO as vehicle control.

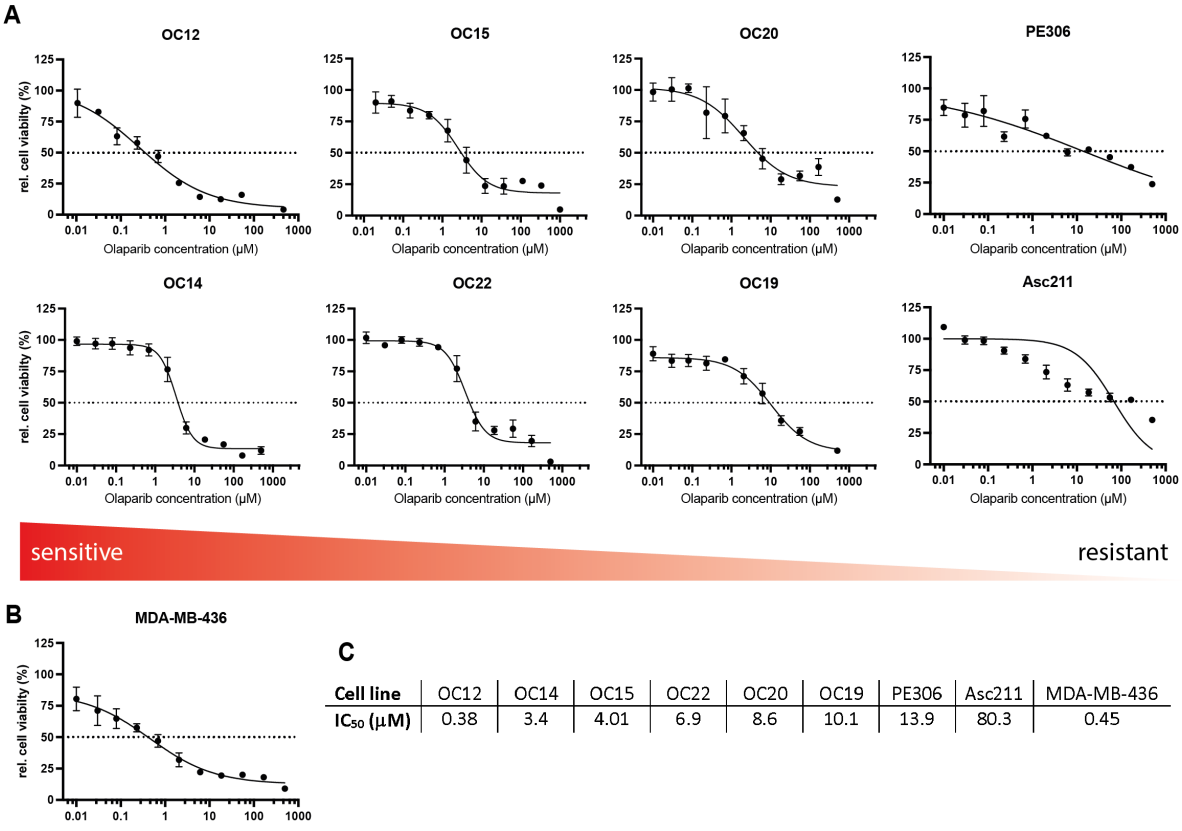

Cell line	OC12	OC14	OC15	OC22	OC20	OC19	PE306	Asc211	MDA-MB-436
IC_{50} (µM)	0.38	3.4	4.01	6.9	8.6	10.1	13.9	80.3	0.45

Figure 9 Sensitivity to olaparib of six ovarian cancer cell lines.
A Drug titration assay was performed on eight different ovarian cancer cell lines. Cells were treated with indicated concentrations of olaparib for 5 days, and relative cell viability was normalized to corresponding DMSO control. The bar below orders the cells from sensitive to resistant based on their IC_{50} values. **B** Drug titration assay conducted on BRCA1-deficient breast cancer cell line MDA-MB-436. Cells were treated with indicated concentrations of olaparib for 5 days, and relative cell viability was normalized to corresponding DMSO control. **C** Calculated IC_{50} values from the drug titration assays presented in A and B. Data is displayed as mean ± 95 % CI.

The half-maximal inhibitory concentration (IC_{50}), representing the concentration at which 50 % of the cells were found to be non-viable, varied among the six tested cell lines, ranging from 0.38 µM (OC12) to 80.2 µM (Asc211) for olaparib (

Figure **9** A, C). To benchmark these IC_{50} values against BRCA1-deficient cells, I also conducted drug titration assays with the $BRCA1^{-/-}$ cell line MDA-MB-436, which exhibited an IC_{50} of 0.45 µM. This comparison indicated that one of the tested ovarian cell lines (OCI12) with lowest IC_{50} value fell within a similar range as the known PARP inhibitor-sensitive cell line MDA-MB-436. Furthermore, the peak plasma concentration of olaparib in patients is typically between 12 and 16 µM, and 6 out of the 8 tested cell lines (OC12, OC14, OC15, OC22, OC20, OC19) showed lower IC_{50} values than the peak plasma concentration in patients.

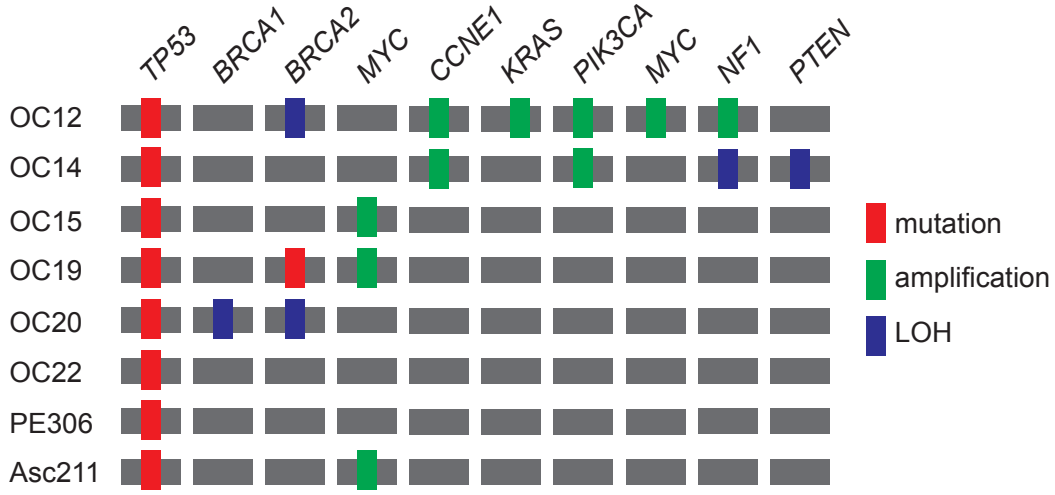

Figure 10 Genetic characterization of the eight ovarian cancer cell lines used for olaparib sensitivity screen.
Genetic characterization of the cell lines is based on Whole Genome Sequencing results. Mutations are depicted as coding nonsynonymous insertions and deletions (Indel) or coding nonsynonymous single nucleotide variants (SNVs); chromosomal amplification and deletion were assessed based on copy number variation (CNV) analysis; LOH = loss of heterozygosity. Sequencing data for OC15, OC19, OC20, OC22, PE306, and Asc211 are from Jabs, J. *et al.* (2017) [139].

To genomically characterize the eight ovarian cancer cell lines used in the olaparib screen described above, I performed whole genome sequencing (WGS) on OC12 and OC14, the most sensitive cell lines in the screen. The sequencing data for the remaining cell lines was obtained from Dr. Julia Jabs, Dr. Franziska Zickgraf, and Dr. Jeongbin Park, as detailed in the publication "Screening drug effects in patient-derived cancer cells links organoid responses to genome alterations" by Jabs et al. [139].

Interestingly, OC12 and OC14 did not exhibit any mutations or genomic alterations in HR genes, even though OC12 had a loss of heterozygosity (LOH) of *BRCA2* (Figure 10). Unfortunately, I could not calculate the HR deficiency status of the cell lines due to the absence of germline control data for all eight patient-derived cell lines. Despite being classified as HR proficient based on WGS, the IC_{50} values of these two cell lines (OC12, 0.38 µM; OC14, 3.4 µM) fell within the range of the HR deficient cell line MDA-MB-436 (0.45 µM) (Figure 9 B).

This shows that the cell lines were sensitive to PARPi despite the lack of detectable HR deficiency. Consequently, I selected these two cell lines to generate PARPi-resistant cell lines to study PARPi resistance.

4.2 Generation of PARPi resistance in olaparib-sensitive cell lines

To generate PARPi-resistant cell lines from the original sensitive cell lines, I recapitulated the treatment regimen in the clinic by treating the cells for several treatment rounds with escalating concentrations of olaparib.

To achieve this, I divided both cell lines into six biological replicates each. Among these, three were treated with olaparib, while the remaining three were treated with DMSO as a vehicle control. The cells underwent a four-day treatment regimen with olaparib or equivalent concentrations of DMSO, with a medium refreshment occurring on the third day. Subsequently, a drug holiday period allowed the cells to recover and proliferate until they reached confluency (illustrated in Figure 11 A and described in section 3.2). Following this phase, the subsequent treatment cycle followed with an increased dose of olaparib (the specific concentrations are outlined in Figure 11 B)

After ten treatment cycles, OC12 cells reached the final olaparib concentration of 20 μM, which is 1.25 to 1.6-fold higher than the peak plasma concentrations typically observed in patients (12 and 16 μM). In the case of OC14 cells, I administered five additional treatment rounds for a total of 15 cycles with a final olaparib concentration of 22.5 μM to induce resistance to olaparib.

I conducted cell viability assays to assess the development of olaparib resistance in the treated cell lines. As expected, the three OC12 and OC14 biological replicates subjected to olaparib treatment (R#1, R#2, R#3) exhibited resistance, as evidenced by the elevated IC_{50} values (Figure 11 C - F). More specifically, I observed a range of resistance levels to olaparib in the three resistant OC12 replicates (R#1, R#2, R#3), spanning from a 35-fold increase (R#3) to a substantial 177-fold increase (R#2) in IC_{50} values compared to the DMSO-treated control cells (S#1, S#2, S#3). Similarly, for the three OC14 cell lines treated with olaparib (R#1, R#2, R#3), I detected an increase in IC_{50} values ranging from 19-fold (R#3) to a notable 118-fold (R#1) elevation.

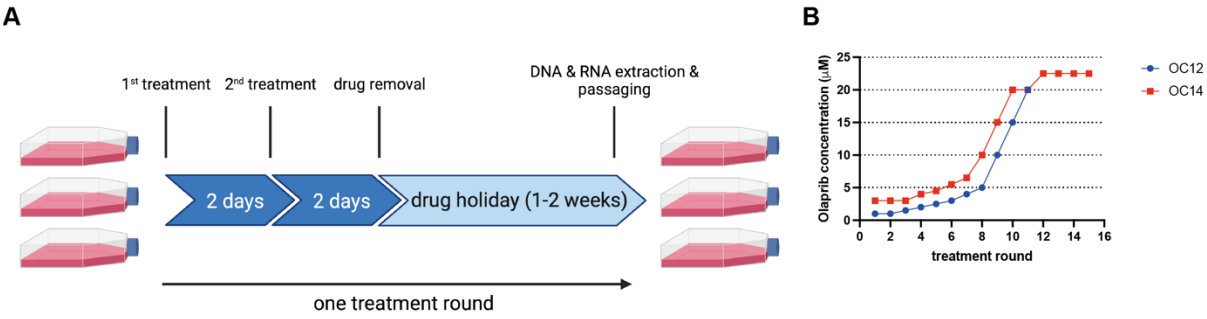

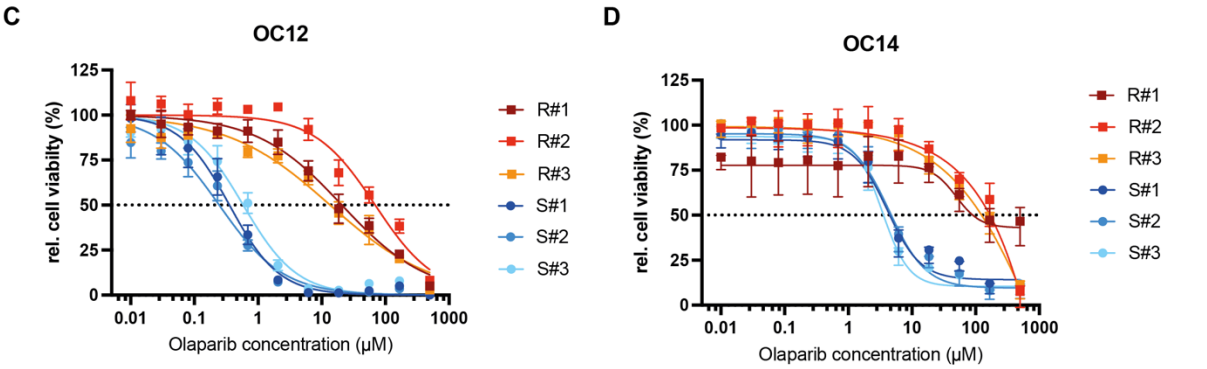

E

cell line	IC_{50} (µM)	cell line	IC_{50} (µM)	resistance score
OC12 S#1	0.35	OC12 R#1	20.7	53.1
OC12 S#2	0.24	OC12 R#2	69.1	177.2
OC12 S#3	0.58	OC12 R#3	13.5	34.6

F

cell line	IC_{50} (µM)	cell line	IC_{50} (µM)	resistance score
OC14 S#1	6.95	OC14 R#1	704	118.3
OC14 S#2	6.34	OC14 R#2	145	24.4
OC14 S#3	4.57	OC14 R#3	115	19.3

Figure 11 Generating olaparib resistant OC12 and OC14 cell lines.
A Schematic representation of the olaparib treatment regimen, consisting of 2 + 2 days of treatment followed by a drug-free interval to allow cells to recovery. **B** Graph showing the olaparib concentration at each treatment round for OC12 and OC14. **C** Cell viability assay results for three control (S) and three olaparib-treated (R) OC12 cell lines after the 10th treatment round. Cells were treated for 5 days with specified concentrations of olaparib, and relative cell viability was normalized to the corresponding DMSO control. **D** Cell viability assay results for three control (S) and three olaparib-treated (R) OC14 cell lines after the 15th treatment round. Cells were treated for 5 days with indicated concentrations of olaparib, and relative cell viability was normalized to the corresponding DMSO control. **E** Table displaying the calculated IC_{50} values of OC12 S and R cell lines after 10 treatment rounds. The resistance score was calculated by dividing the IC_{50} value of the R cell line by the mean IC_{50} value of the three S cell lines. **F** Table representing the calculated IC_{50} values of OC14 S and R cell lines after 15 treatment rounds. The resistance score was calculated by dividing the IC_{50} value of the R cell line by the mean IC_{50} value of the three S cell lines. Data are represented as mean ± 95 % CI.

The results from the cell viability assays aligned with the observations from colony-forming assays (CFA). I treated the three resistant and three sensitive (control) cell lines from both OC12 and OC14 for four days with olaparib at concentrations of 0.5, 1, and 10 µM, alongside DMSO as vehicle control, followed by a two-day recovery period. All three OC12-resistant cells exhibited viability under olaparib treatment at concentrations of 1 µM and 0.5 µM, whereas the sensitive cells did not endure the lowest olaparib concentration of 0.5 µM. In the case of the OC14 cell lines, all three resistant cell lines demonstrated resilience even at the highest olaparib concentration of 10 µM. In contrast, none of the sensitive cell lines could withstand this concentration (Figure 12 A).

To further assess whether the acquired resistance to olaparib is stable or rather plastic, I passaged the olaparib-resistant and sensitive OC12 and OC14 cell lines for ten consecutive passages without any treatment. Subsequently, I conducted cell viability assays with the cell lines. All the resistant lines maintained their resistance to olaparib (Figure 12 B & C) with a slight decrease in the resistance compared to the results obtained directly after the treatment regimen (Figure 12 D & E and Figure 11 E & F), suggesting stable resistance.

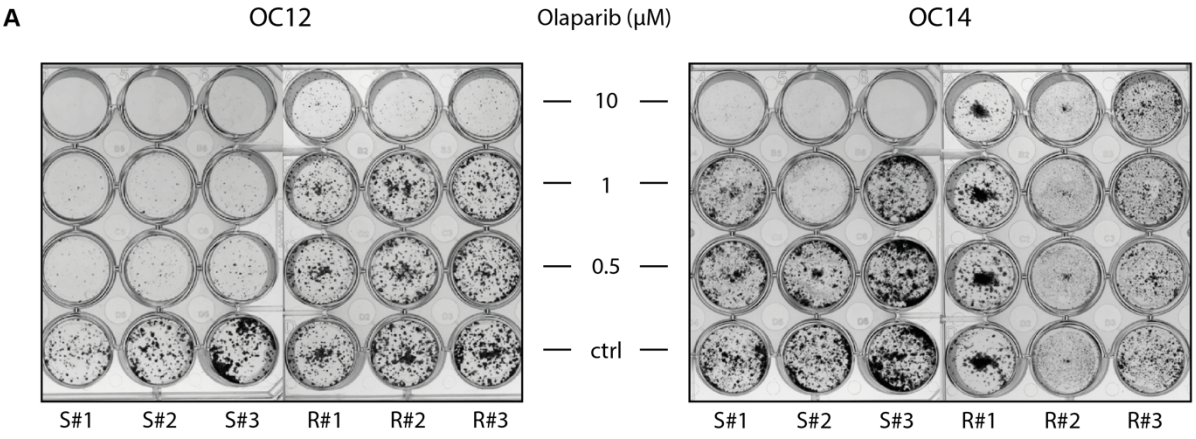

D

cell line	IC_{50} (µM)	cell line	IC_{50} (µM)	resistance score
OC12 S#1	0.3	OC12 R#1	50.1	68
OC12 S#2	0.8	OC12 R#2	51.3	70
OC12 S#3	1.1	OC12 R#3	14.5	20

E

cell line	IC_{50} (µM)	cell line	IC_{50} (µM)	resistance score
OC14 S#1	6.95	OC14 R#1	53.4	9
OC14 S#2	6.34	OC14 R#2	57.5	10
OC14 S#3	4.57	OC14 R#3	162	27

Figure 12 Olaparib-resistant cells remain resistant over several passages without any treatment.
A Colony-forming assay (CFA) results for OC12 and OC14 R and S cells. Cells were treated for four days with specified concentrations of olaparib, followed by a 2-day drug holiday. Subsequently, cells were fixed with 4 % PFA and stained with crystal violet (CV). **B** Cell viability assay results for three control (S) and three olaparib-treated (R) OC12 cell lines after 10 passages without treatment. Cells were treated for 5 days with indicated concentrations of olaparib, and relative cell viability was normalized to the corresponding DMSO control. **C** Cell viability assay results for three control (S) and three olaparib-treated (R) OC14 cell lines after 10 passages without treatment. Cells were treated for 5 days with specified concentrations of olaparib, and relative cell viability was normalized to the corresponding DMSO control. **D** Table displaying the calculated IC_{50} values and resistance scores of OC12 R and S cell lines after 10 passages without treatment. The resistance score was determined by dividing the IC_{50} value of the R cell line by the mean IC_{50} value of the three S cell lines. **E** Table showing the calculated IC_{50} values and resistance scores of OC14 R and S cell lines after 10 passages without treatment. The resistance score was calculated by dividing the IC_{50} value of the R cell line by the mean IC_{50} value of the three S cell lines. Data is presented as mean ± 95 % CI.

4.3 Olaparib-resistant cell lines are cross-resistant to other PARP inhibitors

Considering that all PARPis bind to the NAD^+ binding domain of PARP1, I conducted cell viability assays to investigate whether cells that had developed resistance to olaparib treatment would also exhibit cross-resistance to other PARPis. I treated the OCI12 and OCI14 cells with PARPis niraparib, talazoparib, and rucaparib for five days. The utilized PARPis differ in their ability to trap PARP1 onto the DNA, with talazoparib being the strongest PARP trapper. In contrast, niraparib and rucaparib promote the release of PARP1 from the DNA (in more detail 1.5).

The three olaparib-resistant OC12 cell lines were also resistant to the other tested PARPis, including talazoparib, niraparib, and rucaparib (Figure 13 A, C, E). To quantify the resistance, I calculated a resistance score for each PARPi as the ratio of the IC_{50} value of the resistant cell line and the mean IC_{50} value of the three sensitive (control) cell lines. For talazoparib, the resistance score between resistance and sensitive cells ranged from 21 (R#3) up to 331 (R#2) (Figure 13 B). For niraparib, the resistance score was 7 between resistant and sensitive cells (Figure 13 D). For rucaparib, a PARPi without trapping potential, the resistance score ranged from 7 (R#2) up to 9 (R#1) (Figure 13 F). These results indicate that cells treated with olaparib with subsequently developed resistance to the treatment also exhibited cross-resistance to other PARPis, regardless of their PARP1 trapping potential.

A

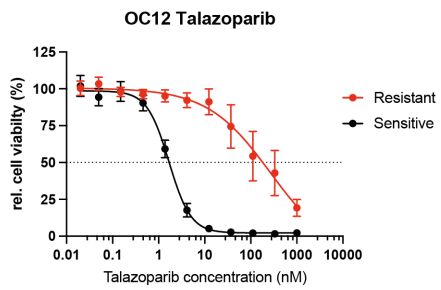

B

cell line	IC_{50} (nM)	cell line	IC_{50} (nM)	resistance score
OC12 S#1	1.4	OC12 R#1	160	92
OC12 S#2	1.7	OC12 R#2	576	331
OC12 S#3	2.1	OC12 R#3	36.3	21

C

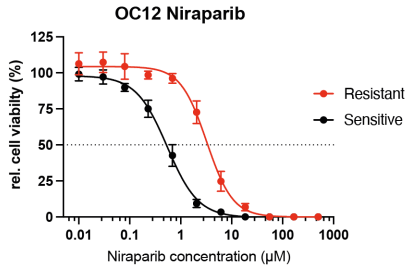

D

cell line	IC_{50} (µM)	cell line	IC_{50} (µM)	resistance score
OC12 S#1	0.5	OC12 R#1	3.8	7
OC12 S#2	0.5	OC12 R#2	3.4	7
OC12 S#3	0.6	OC12 R#3	3.2	7

E

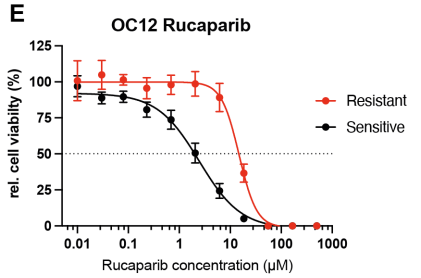

F

cell line	IC_{50} (µM)	cell line	IC_{50} (µM)	resistance score
OC12 S#1	1.8	OC12 R#1	16.4	9
OC12 S#2	1.4	OC12 R#2	12.9	7
OC12 S#3	2.18	OC12 R#3	14	8

Figure 13 Olaparib-resistant OC12 cells are also cross-resistant to other PARP inhibitors.
A, C, E Cell viability assay results for the three OC12 R and three OC12 S cell lines. Cells were treated for 5 days with specified concentrations of talazoparib (A), niraparib (C), and rucaparib (E), and relative cell viability was normalized to the corresponding DMSO control. Data is shown as mean ± 95 % CI. **B, D, F** Alongside each graph, tables display the calculated IC_{50} values and resistance scores to the respective PARPi. The resistance score was calculated by dividing the IC_{50} value of the R cell line by the mean IC_{50} value of the three S cell lines.

Testing the olaparib-resistant OC14 cell lines, I could also observe that they were cross-resistant to talazoparib and niraparib (Figure 14 A, C), as indicated by the resistance scores. For talazoparib, the resistance score was in a range from 21 (R#3) up to 178 (R#1) (Figure 14 B). Compared to talazoparib, the resistance of OC14 resistant cells to niraparib was lower, ranging from 2 (R#2) to 6 (R#3) (Figure 14 D). However, OC14 sensitive cells were not resistant to rucaparib. Here, the resistance score was only in the range of 1 (R#2) to 3 (R#3) (Figure 14 E, F). In summary, OC14 resistant cells were also cross-resistant to other PARPi but in contrast to OC12 remained sensitive to rucaparib, a PARPi that does not trap PARP1 onto the DNA.

A

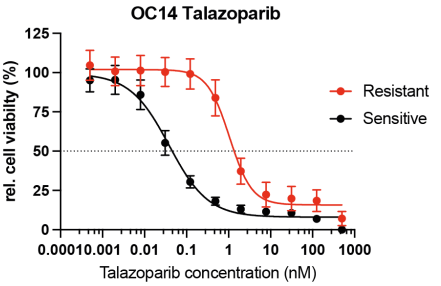

B

cell line	IC_{50} (nM)	cell line	IC_{50} (nM)	resistance score
OC14 S#1	0.1	OC14 R#1	11.8	178
OC14 S#2	0.05	OC14 R#2	1.2	18
OC14 S#3	0.04	OC14 R#3	1.4	21

C

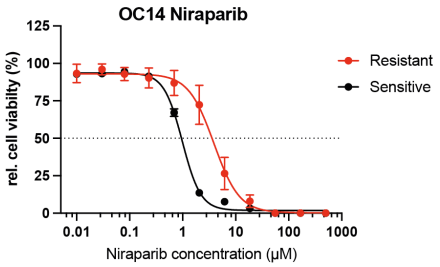

D

cell line	IC_{50} (µM)	cell line	IC_{50} (µM)	resistance score
OC14 S#1	1.1	OC14 R#1	4.2	4
OC14 S#2	0.9	OC14 R#2	2.1	2
OC14 S#3	0.9	OC14 R#3	5.9	6

E

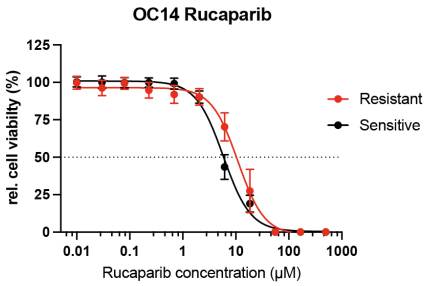

F

cell line	IC_{50} (µM)	cell line	IC_{50} (µM)	resistance score
OC14 S#1	6.8	OC14 R#1	9.4	2
OC14 S#2	7.7	OC14 R#2	7	1
OC14 S#3	4.3	OC14 R#3	20.9	3

Figure 14 Olaparib-resistant OC14 cells are cross-resistant to other PARP inhibitors.
A, C, E Cell viability assay results for the three OC14 R and three OC14 S cell lines. Cells were treated for 5 days with specified concentrations of talazoparib (A), niraparib (C), and rucaparib (E), and relative cell viability was normalized to the corresponding DMSO control. Data is shown as mean ± 95 % CI. **B, D, F** Alongside each graph, tables display the calculated IC_{50} values and resistance scores to the respective PARPi. The resistance score was calculated by dividing the IC_{50} value of the R cell line by the mean IC_{50} value of the three S cell lines.

4.4 Olaparib-resistant cells are not cross-resistant with DNA-damaging agents

Given how PARPis induce DNA double-strand breaks by hindering single-strand break repair and causing replication fork collapse, I hypothesized that PARP inhibitor-resistant cells might also exhibit cross-resistance to other DNA-damaging agents. Therefore, I conducted cell viability assays and CFA to investigate this. First, I treated olaparib-resistant and sensitive OC12 and OC14 cells with oxaliplatin (Figure 15 A-D). Oxaliplatin is a DNA cross-linking agent that induces intra- and inter-strand crosslinks in the DNA. DNA crosslinks inhibit transcription and replication by preventing DNA strand separation, and the resulting lesions are predominantly repaired through HR initiated by the Fanconi anemia pathway [140]. However, both PARP inhibitor-resistant cells OC12 and OC14 were not resistant to oxaliplatin treatment.

In detail, the response to oxaliplatin treatment was not significantly different from the sensitive cells (OC12 R: 50 μM, OC12 S: 27 μM; OC14 R:3.9 μM, OC14 S: 2.1 μM) (Figure 15 A-D).

In addition to oxaliplatin, I tested the DNA alkylating agent methyl methanesulfonate (MMS). MMS modifies both guanine (to 7-methylguanine) and adenine (to 3-methyladenine), leading to base mispairing. These mispairings are primarily repaired by the BER pathway. Furthermore, it has been shown that MMS can also induce DSBs. In line with the findings with oxaliplatin, MMS treatment did not induce a significant difference between olaparib-resistant and sensitive OC12 and OC14 cells in the cell viability assay (Figure 15 E, F). For resistant OC12 cells, the IC_{50} value was 0.001 % MMS, which was slightly increased compared to sensitive cells (IC_{50} 0.003 % MMS) (Figure 15 E).

Last, I tested paclitaxel, a taxane that stabilizes microtubules. Next to platinum-based chemotherapy, paclitaxel is the standard-of-care for primary ovarian cancer. Similar to the other DNA-damaging agents, when treating the cells with paclitaxel, I did not observe a significant difference in the treatment effect between olaparib-resistant and sensitive OC12 (R: 1.7 nM, S: 1.3 nM) and OC14 cells R: 4.5 nM, S: 10 nM) in the cell viability assay (Figure 15 G, H).

In summary, the generated olaparib-resistant cells exhibited cross-resistance to other PARPis but had not acquired a general resistance to DNA-damaging agents such as oxaliplatin and MMS or paclitaxel.

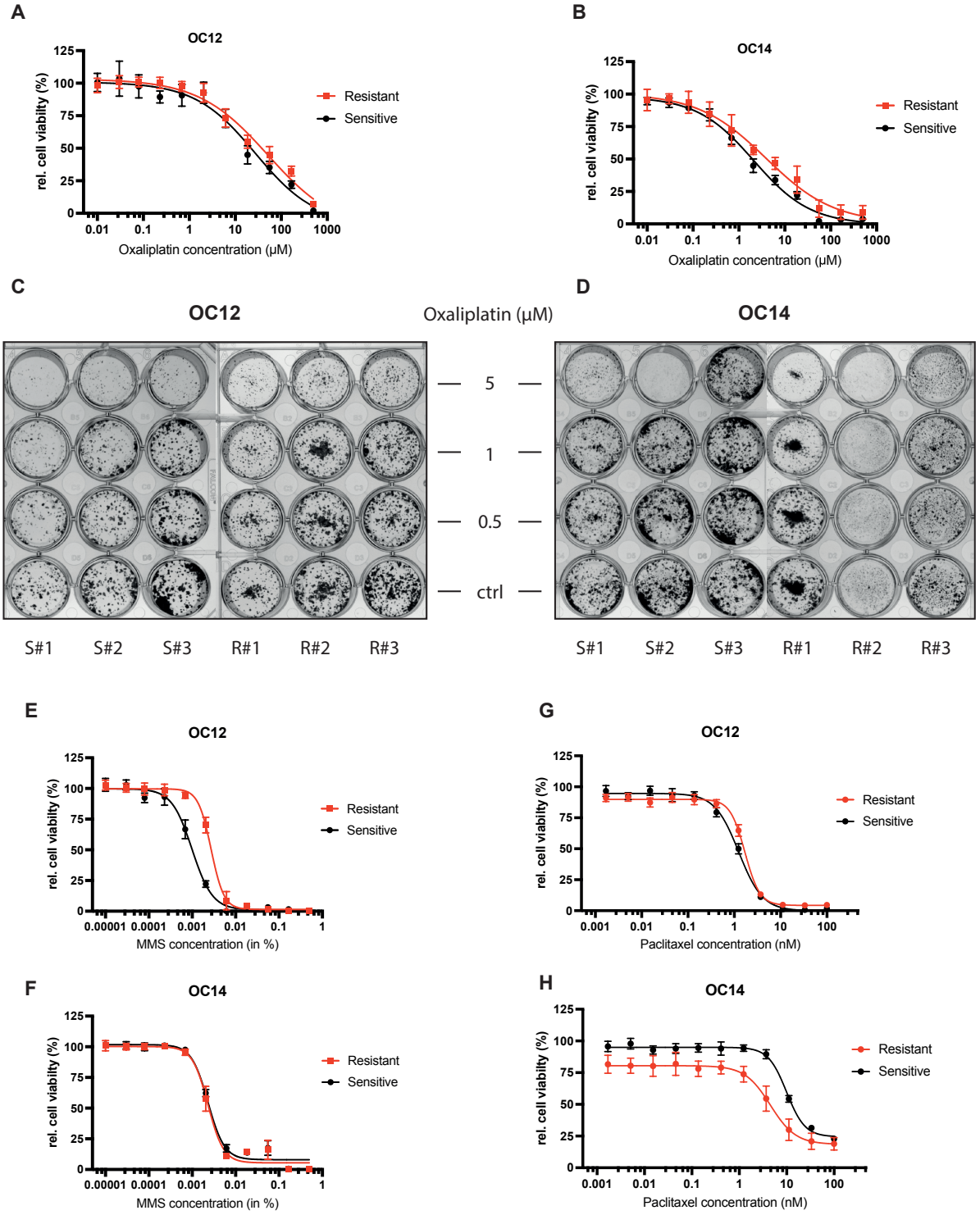

Figure 15 Comparative sensitivity to DNA damaging agents in Olaparib-resistant and sensitive OC12 and OC14 cell lines OC12.

A Cell viability assay for OC12 R (n=3) and S (n=3) cell lines. Cells were treated for 3 days with specified concentrations of oxaliplatin, and relative cell viability was normalized to the corresponding DMSO control. **B** Cell viability assay for OC14 R (n=3) and S (n=3) cell lines. Cells were treated for 3 days with specified concentrations of oxaliplatin, and relative cell viability was normalized to the corresponding DMSO control. **C** CFA results for OC12-resistant and sensitive cells. Cells were treated for four days with specified concentrations of oxaliplatin, followed by a 2-day drug holiday. Cells were fixed in 4 % PFA and stained with CV. **D** CFA results for OC14 resistant and sensitive cells. Cells were treated for four days with specified concentrations of oxaliplatin, followed by a 2-day drug holiday. Cells were fixed in 4 % PFA and stained with CV. **E** Cell viability assay for OC12 R and OC12 S cell lines. Cells were treated for 3 days with indicated concentrations of MMS, and relative cell viability was normalized to the corresponding control. **F** Cell viability assay for the three OC14 R and three OC14 S cell lines. Cells were treated for 3 days with specified concentrations of MMS, and relative cell viability was normalized to the corresponding control. **G** Cell viability assay for the three OC12 R and three OC12 S cell lines. Cells were treated for 3 days

with specified concentrations of paclitaxel, and relative cell viability was normalized to the corresponding DMSO control. **H** Cell viability assay for the three OC14 R and three OC14 S cell lines. Cells were treated for 3 days with indicated concentrations of paclitaxel, and relative cell viability was normalized to the corresponding DMSO control. Data is presented as mean ± 95 % CI.

4.5 Gene expression analysis indicated an upregulation of ABCB1 & 4 as well as APLF and TWIST in resistant OC12 cell lines

Next, I aimed to identify potential resistance mechanisms to olaparib in the resistant OC12 and OC14 cell lines based on gene expression analysis. I sequenced the RNA from the three resistant and three sensitive cell lines of OC12 and OC14, as well as from the parental (basal) cell lines. For an overview of the gene expression data among the three resistant, sensitive, and basal cell lines, I conducted a Principal Component Analysis (PCA). Based on the PCA results, I observed that the three resistant cell lines separated from the sensitive and basal cell lines for both OC12 and OC14 (see suppl. Figure 1 A & B). This initial observation suggests a significant difference in gene expression between the resistant and sensitive cell lines, warranting further exploration.

To investigate the resistance mechanism that could have arisen in all three biological replicates, I performed differential gene expression (DEG) analysis between the three resistant and three sensitive cells of OC12 and OC14 (Figure 16 A). In case of OC12, I could observe a downregulation of several *HOXA* genes (*HOXA2,4,5*), which are organized as a cluster on chromosome seven and play a fundamental role in the embryologic development; HOXA genes were reported to be differentially expressed in ovarian cancer [141]. The most down regulated gene in the resistant cells was Prostate Stem Cell Antigen *(PSCA*), which is found to be highly upregulated in prostate cancer [142]. The most upregulated genes in resistant OC12 cells were the gene encoding for the cytoskeleton protein Adducin 2 (*ADD2*) and Regulating Synaptic Membrane Exocytosis 2 (*RIMS2*) gene. For OC14, the most downregulated gene in resistant cells was the gene encoding for Nitric Oxide Synthase Trafficking protein (*NOSTRIN*), which is involved in the production of nitric oxide [143] and was also linked to colon cancer progression [144].

For a more focused analysis, I analyzed the gene expression of specific subsets of genes, in particular DNA repair-associated genes (Human Gene Set: HALLMARK_DNA_REPAIR) and known PARPi resistance-inducing genes (*ABCB1, ABCB4, PARP1, DYNLL1, PARG, TRIP13, SHLD1, SHLD2, MAD2L2, TP53BP1*). In this focused analysis, I identified a significant (p_{adj} < 0.01?) upregulation of the multidrug resistance genes ATP Binding Cassette Subfamily B Member 1 (*ABCB1*) with a log2-fold change (log_2FC) of 7.2 and ATP Binding Cassette Subfamily B Member 4 (*ABCB4*) with a log_2FC of 4.7 in the resistant OC12 cell lines (Figure 16 C). As introduced in 1.6.2, the upregulation of *ABCB1* is a known and well-studied resistance mechanism to PARPi treatment.

To validate whether the high expression of *ABCB1* is already induced at early time points in the treatment regimen, I conducted gene expression analysis using Real-time PCR (qPCR). The results confirmed a significant upregulation of *ABCB1* gene expression (16-fold) at treatment round five in the olaparib-treated cells compared to control cells (Figure 17 A). This effect became even more pronounced at treatment round 10, with a 327-fold upregulation of *ABCB1* (OC12 R#1) compared to the sensitive cells (Figure 17 A). This suggests that *ABCB1* upregulation goes hand in with the acquisition of PARPi resistance.

In addition to the upregulation of *ABCB1* and *ABCB4*, I also observed a significant (p_{adj} < 0.001) upregulation of transcription factor Twist Family BHLH Transcription Factor 1 (*TWIST1*) with a log_2FC of 4.8 and Aprataxin and PNKP Like Factor (*APLF*) that is involved in NHEJ with a log_2FC of 3.1 (Figure 16 D). These data suggest that PARPi resistance is associated with increased efflux pump as well as NHEJ activity.

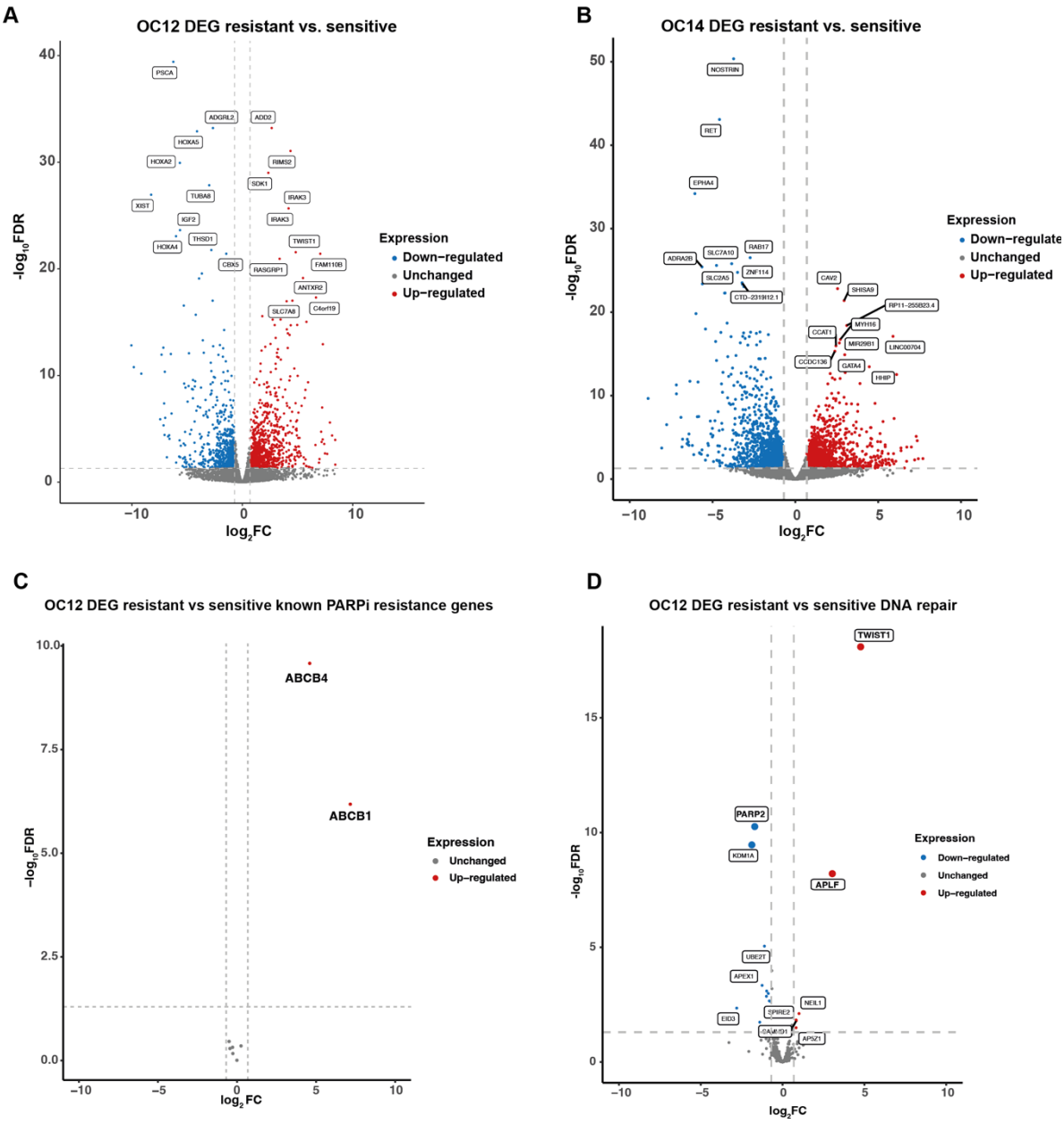

Figure 16 Differential gene expression analysis after treatment regimen between resistant and sensitive OC12 & OC14
A Volcano plot depicting all differentially expressed genes (DEG) between R and S OC12 cells immediately after the treatment regimen. **B** Volcano plot depicting all DEG between olaparib-resistant and sensitive OC14 cells immediately after the treatment regimen **C** Volcano plot representing a subset of DEG composed of known PARP inhibitor (PARPi) resistance-inducing genes between olaparib resistant and sensitive OC12 cells. **D** Volcano plot displaying a subset of DEG consisting of DNA repair-related genes between olaparib-resistant and sensitive OC12 cells.

4.6 Individual upregulation of ABCB1/4, APLF, and TWIST1 is not responsible for acquired PARPi resistance in OC12 cells

To validate whether the upregulation of *ABCB1/4*, *APLF,* or *TWIST1* in the resistant OC12 cells resulted in the acquired PARPi resistance, I performed CRISPR/Cas9-guided knockouts (KO) of the four target genes in OC12, due to the fact that they were not differentially regulated in OC14 cells. I verified the successful KO of *ABCB1* in the OC12 R#1 cell lines based on protein expression analysis in a Western Blot (WB). ABCB1 protein was abolished in the KO cells compared to the non-targeting (NT) control of OC12 R#1 (Figure 17 B). Moreover, the WB analysis validated the differences in ABCB1 expression between olaparib-resistant and sensitive cells on the protein level, as initially indicated by qPCR analysis (Figure 17 A).

To investigate whether ABCB1 deficient resistant OC12 R#1 cells could be re-sensitized to olaparib treatment, I performed a cell viability assay, comparing ABCB1 wildtype (WT) with ABCB1 deficient cells (ABCB1 KO). Interestingly, the R#1 ABCB1 KO cells (IC_{50} 25 μM) showed the same resistance phenotype as the R#1 WT control cells (IC_{50} 26 μM) (Figure 17 C). To further confirm this observation, I performed a CFA with the three olaparib-resistant and sensitive OC12 cell lines. I treated the cells for 4 days with 10, 20, or 40 μM olaparib, with or without 300 nM elacridar, a potent ABCB1 inhibitor, followed by 2 days drug holiday. Similar to the results with the ABCB1 KO cells, there was no observable difference between elacridar-treated and untreated olaparib-resistant OC12 cells in their response to olaparib (Figure 17 D).

Furthermore, I conducted cell viability assays with OC12 R#1 cells, treating them with various concentrations of olaparib, alone or in combination with 300 nM elacridar, for five days. Similar to the CFA results, I did not observe any differences between olaparib-resistant OC12 cells treated with the combination of elacridar (IC_{50} 4.8 μM) and olaparib and the cells only treated with olaparib (IC_{50} 7 μM) (Figure 17 E). It is worth noting that acquired resistance to PARP inhibitors might be influenced by combined amplification of both *ABCB1* and *ABCB4* gene expression, as indicated in the analysis of the DEGs analysis (Figure 16 C).

Consequently, I performed a double KO of both *ABCB1* and *ABCB4.* However, as there is no suitable antibody available for WB analysis of ABCB4, I utilized Sanger sequencing to estimate the KO efficacy of *ABCB4.* The double KO resulted in an editing efficacy of 95 % for OC12 R#1

and 85 % for OC12 S#1 (suppl. Figure 1 E, F). These numbers were comparable with the single KO efficacy of ABCB1 in OC12 R#1 (92 %) and S#1 (90 %) (suppl. Figure 1 C, D), for which I could validate the findings by WB analysis (Figure 17 B).

Using the double KO cells, I performed cell viability assays, treating the resistant OC12 R#1 and sensitive S#1 ABCB1/4 double KO as well as resistant OC12 R#1 and sensitive S#1 WT control cells with indicated concentrations of olaparib for five days. For the resistant OC12 R#1 cells, I observed a reduction of the IC_{50} values from 26 μM to 6 μM in the ABCB1/4 double KO cells (Figure 17 F). A similar effect was detected for the sensitive OC12 S#1 cells, where the ABCB1/4 double KO reduced the IC_{50} value for the control cells from 0.7 μM to 0.1 μM (Figure 17 F). Even though the ABCB1/4 double KO markedly reduced the IC_{50} values of the resistant cells, they were not sensitized to the IC_{50} values of the sensitive cells, suggesting that ABCB1/4-driven drug efflux is not the sole driver of PARPi resistance.

To further assess this, I performed a cell viability assay using pamiparib, a potent and specific PARP1 and PARP2 inhibitor. Pamiparib is designed not to be a substrate for ABC transporters, offering a potential treatment option for tumors that have developed PARPi resistance by upregulating ABCB1 and ABCB4. I treated the three olaparib-resistant and sensitive OC12 cells with different concentrations of pamiparib for five days. In line with the double KO data, the resistant cells were also resistant to pamiparib with an IC_{50} value of 14 μM (Figure 17 G), which is 10.8-fold higher than the concentration pamiparib should inhibit PARP1 function (1.3 nM) [104].

In summary, the upregulation of both drug efflux pumps has a small impact on the observed PARPi resistance but is not alone responsible for the observed resistance. This conclusion is supported by the minor changes in IC_{50} values when knocking out *ABCB1* and *ABCB4*, as well as the resistance of olaparib-resistant cells to the treatment with pamiparib, which is not a substrate for ABCB transporters. Indicating that the acquired resistance to PARP is not driven by an upregulation of ABCB1.

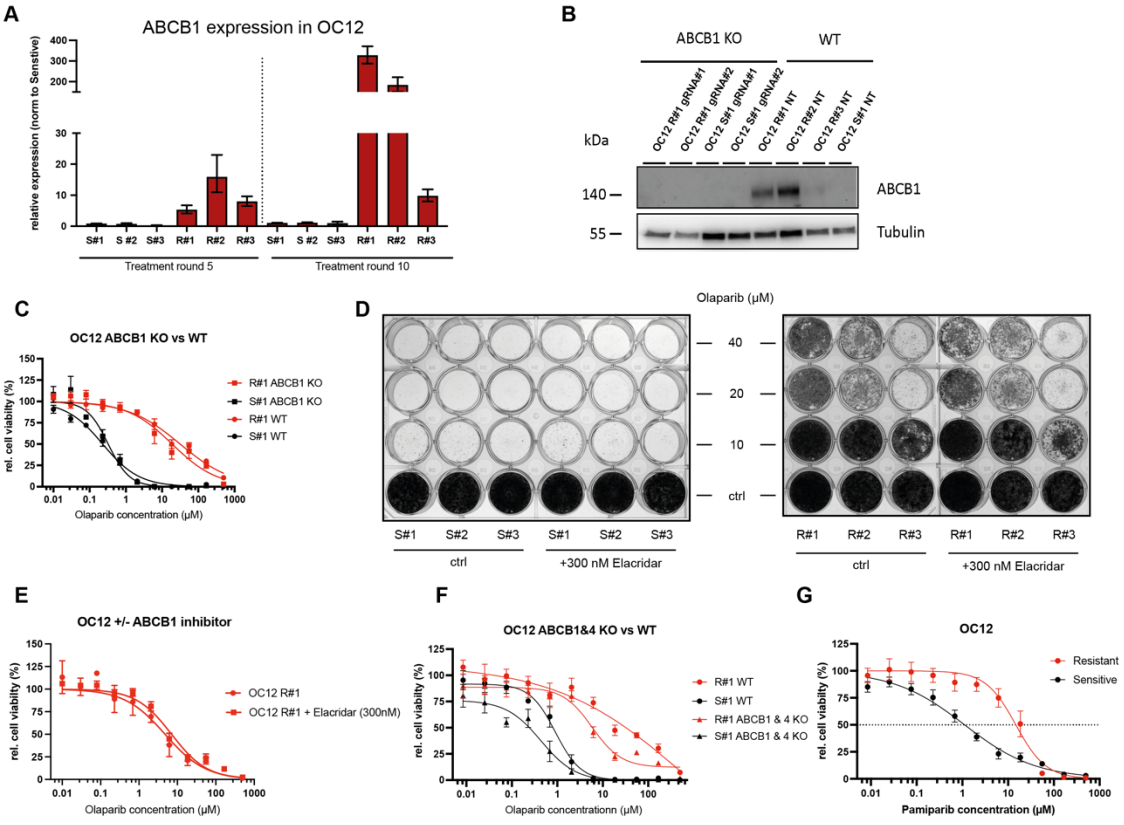

Figure 17 The drug efflux pumps ABCB1 & ABCB4 are upregulated in OC12 R cells; double KO of ABCB1/4 could only slightly reduce the PARPi resistance.
A ABCB1 expression was assessed through qRT-PCR analysis in OC12 R and S cells at treatment rounds 5 and 10. **B** Western blot analysis of ABCB1 protein expression in OC12 R and S cells with CRISPR Cas9 KO and WT. **C** Cell viability assay of OC12 R#1 and S#1 cell lines (WT and ABCB1 KO). Cells were treated for 5 days with specified concentrations of olaparib, and relative cell viability was normalized to the corresponding DMSO control. **D** CFA of OC12 resistant and sensitive cells. Cells were treated for four days with specified concentrations of olaparib and 300 nM of the ABCB1 inhibitor elacridar. This was followed by a 2-day drug holiday, after which cells were fixed in 4 % PFA and stained with CV. **E** Cell viability assay of OC12 R#1 cell lines. Cells were treated for 5 days with indicated concentrations of olaparib, with one replicate additionally receiving 300 nM elacridar. Relative cell viability was normalized to the corresponding DMSO control. **F** cell viability assay of OC12 R#1 and S#1 cell lines (WT and double KO of ABCB1 and ABCB4). Cells were treated for 5 days with indicated concentrations of olaparib, and relative cell viability was normalized to the corresponding DMSO control. **G** Cell viability assay of OC12 R and S cell lines. Cells were treated for 5 days with specified concentrations of pamiparib, and relative cell viability was normalized to the corresponding DMSO control. Data is presented as mean ± 95 % CI.

Besides upregulation of *ABCB1* and *ABCB4*, I observed that the transcription factor *TWIST1* and the DNA repair enzyme *APLF* were upregulated in the OC12 resistant cells compared to the sensitive cells (Figure 18 A). To evaluate the potential role of these two candidates, I performed CRISPR/Cas9-guided KOs of both genes and validated the KO efficacy by Sanger sequencing. The APLF KO had a 78 % KO efficacy in resistant OC12 R#1 cells and 91 % in sensitive OC12 S#1 cells. The TWIST1 KO was less effective, with a KO efficacy of 75 % in resistant OC12 R#1 cells and 53 % in sensitive OC12 S#1 cells (suppl. Figure 1 G-J).

To investigate whether reducing APLF or TWIST1 expression could re-sensitize resistant OC12 R#1 cells to olaparib treatment, I conducted a cell viability assay utilizing APLF KO and TWIST1 KO cells (OC12 R#1 APLF KO and OC12 S#1 APLF KO; OC12 R#1 and S#1 TWIST1 KO) as well as NT control cell lines (OC12 R#1 NT and S#1 NT; OC12 R#1 NT and S#1 NT). The cells were exposed to various concentrations of olaparib for 5 days. The IC_{50} value did not differ between the resistant OC12 R#1 APLF KO cells (10.8 µM) and the resistant OC12 R#1 NT cells (9.1 µM) (Figure 18 B). Depletion of TWIST1 had a similar result. There was no significant change in the IC_{50} value for olaparib between OC12 R#1 TWIST1 KO (10.8 µM) and OC12 R#1 NT (9.1 µM) cells (Figure 18 C), suggesting that PARPi resistance is not driven by upregulation of APLF or TWIST1.

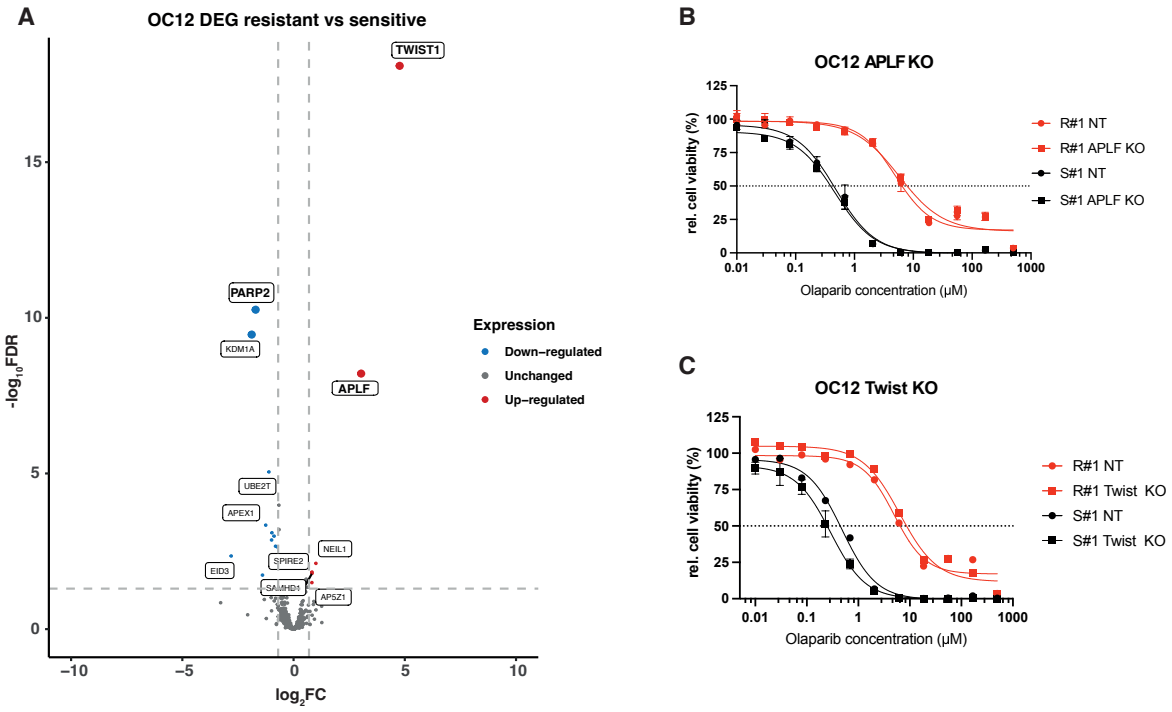

Figure 18 TWIST1 and APLF are upregulated in OC12 R cells but are not responsible for the acquired resistance.
A Volcano plot illustrates a subset of DEG related to DNA repair between olaparib-resistant and sensitive OC12 cells. **B** Cell viability assay results for OC12 R#1 and S#1 cell lines (NT and APLF KO). Cells were treated for 5 days with specified concentrations of olaparib, and relative cell viability was normalized to the corresponding DMSO control. **C** Cell viability assay results for OC12 R#1 and S#1 cell lines (NT and Twist1 KO). Cells were treated for 5 days with indicated concentrations of olaparib, and relative cell viability was normalized to the corresponding DMSO control. Data is presented as mean ± 95 % CI.

In summary, my investigation did not substantiate the notion that the upregulation of drug efflux pumps ABCB1 and ABCB4, or the increased expression of transcription factor TWIST1 and DNA repair enzyme APLF, serves as the primary cause behind the observed resistance to olaparib in OC12 cell lines.

4.7 Prolonged olaparib treatment results in chromosomal rearrangements and the acquisition of functional mutations

As shown by others, secondary -mutations of *BRCA1/2* [84, 145] or mutation of specific genes, including DNA-repair genes, can result in a resistance to PARPi treatment [41, 91, 146] . For this reason, I was also interested to assess whether a mutation could explain the acquired resistance to PARPi. Therefore, I performed Whole Genome Sequencing (WGS) of all three resistant, three sensitive and the basal OC12 and OC14 cell lines. I found a small set of functional mutations and copy number alterations that were present in olaparib-resistant OC12 (Table 20 and Table 21) and OC14 (Table 22 and Table 23) cell lines compared to basal and sensitive cell lines. However, none of these alterations were likely candidates driving olaparib resistance as they did not affect DNA damage-related genes.

In theory, a mutation in the PARP1 gene, which might either reduce the affinity to the PARPi or sustain the endogenous protein function when bound to the inhibitor, would also lead to resistance to PARPis [107]. However, I could not find a mutation of PARP1 based on WES and WGS in OC12 and OC14 resistant cells (Table 20-23).

To further characterize the impact of prolonged olaparib treatment on the genomic stability of OC12 and OC14 cell lines, I performed M-FISH analysis with Prof. Anna Jauch to assess chromosomal rearrangements. I identified extensive chromosomal aberrations in OC14 R#1 cells compared to S#1 cells; most of the chromosomes were amplified in the olaparib-resistant cells, resulting in a polyploid (n 84 – 96 chromosomes) genotype accompanied by multiple translocations (suppl. Figure 7). Interestingly, the sensitive cells already had a triploid genotype, possibly due to the patient's pre-treatment with chemotherapy or a *TP53* mutation, both of which are known to cause genomic rearrangements and amplifications [147, 148]. Indeed, both OC12 and OC14 cell lines carried a *TP53* mutation (see Figure 10) and were pretreated with chemotherapy (as shown in Table 2). These findings suggest further clonal evolution under olaparib treatment of OC14 cells from the triploid basal cell lines.

For OC12 R#1, I could not detect any chromosomal amplifications. Of note, in the case of OC12, the sensitive cells were already triploid (suppl. Figure 8). However, I could observe some chromosomal losses in R#1 cell line compared to S#1, three copies of chromosome. 1 (chr. 1) in R#1 compared to 4 copies in S#1; (chr.4: R#1 3x, S#1 4x; chr.6: R#1 2x, S#1 3x; chr9: R#1 4x,

S#1 3x; chr 20: R#1 der(20,17,2) 1x, S#1 der(20,17,2) 2x, chr.22: R#1 1x, S#1 2x) (suppl. Figure 8).

4.8 Olaparib treatment has only a minimal effect on the gene expression of PARPi-resistant cells

To assess the direct impact of olaparib treatment on the gene expression in resistant and sensitive cells, I exposed the olaparib-sensitive (S#1,2,3) and resistant (R#1,2,3) OC12 and OC14 cell lines to olaparib concentrations corresponding to their IC50 values (as shown in Figure 11 E, F). I harvested RNA before adding the drug (T0), and after 12 h (T1), 72 h (T2) and 120 h (T3) olaparib exposure (a graphical scheme of this experiment is displayed in Figure 19 A).

The following analysis of the RNA-seq data was performed together with Dr. Aino-Maija Leppä.

Based on the PCA, I observed that the three olaparib-resistant OC12 cell lines clustered apart from the sensitive cells, independent of the additional exposure to olaparib. Interestingly, I did not observe big changes in the gene expression between untreated (T0) and the early treatment time point (T1) in either resistant or sensitive OC12 cells (Figure 19 B). However, the gene expression at later time points of treatment showed more global differences in resistant and sensitive OC12 cells compared to early time points, as indicated by the shift in the PCA plot (Figure 19 B).

Like the OC12 cell lines, the three OC14 resistant cell lines clustered apart from the sensitive cell lines. However, the differences between the resistant cell line replicates were more abundant in OC14, suggesting larger biological variation as a result of treatment pressure (Figure 19 C). In contrast to OC12, OC14 cells did not show changes in the gene expression at the different time points (T0 -T3) in either resistant or sensitive cells under olaparib treatment (Figure 19 C), suggesting that the olaparib treatment has no direct impact in the gene expression in OC14 cells.

To first analyze which molecular pathways differ between olaparib-resistant and sensitive OC12 and OC14 cell lines, I performed Gene Set Enrichment Analysis (GSEA) using the normalized read counts ranked based on log2fold change between resistant and sensitive cells at each timepoint (T0-T3) and called the top 30 Hallmark gene sets. In the case of OC12, I observed a significant downregulation (p.adj < 0.05) of MYC-targeted V1 and V2 pathways at T0 in the resistant cells, indicating a baseline difference between resistant and sensitive cells even in the absence of additional treatment (Figure 20 A). On the other hand, I observed a significant upregulation of KRAS signaling pathways in the resistant cells, which was also in line with the downregulation of the "KRAS signaling down" pathway (Figure 20 A). As T1 did not show a marked change in gene expression to T0, I focused the GSEA only on the later treatment time points (72h (T2) and 120h (T3) under olaparib treatment). Interestingly, the same pathways were differentially regulated between olaparib-resistant and sensitive OC12 cell lines at later time points, mirroring observations from early time points (T0, T1). Specifically, the MYC targets V1 and V2 were significantly downregulated, whereas KRAS signaling was upregulated in the resistant compared to the sensitive cells (Figure 20 C, E). This shows that the differentially regulated pathways between resistant and sensitive cells is caused by the resistant phenotype and not triggered by direct olaparib exposure.

In the case of the OC14 cell lines, I observed significant (padj < 0.05) upregulation of several immune response-related pathways, such as TNFA signaling, Complement, Allograft rejection, and Inflammatory response pathways in the olaparib-resistant OC14 cells at T0 (Figure 20 B). Besides the immune response pathways, JAK-STAT3, NOTCH, and Apoptosis signaling were also upregulated in the resistant cells (Figure 20 B). Consistent with the findings in OC12 cell lines, I also observed in OC14 that the same pathways remained differentially regulated between resistant and sensitive cell lines across various time points of olaparib treatment (Figure 20 D, F and suppl. Figure 4).

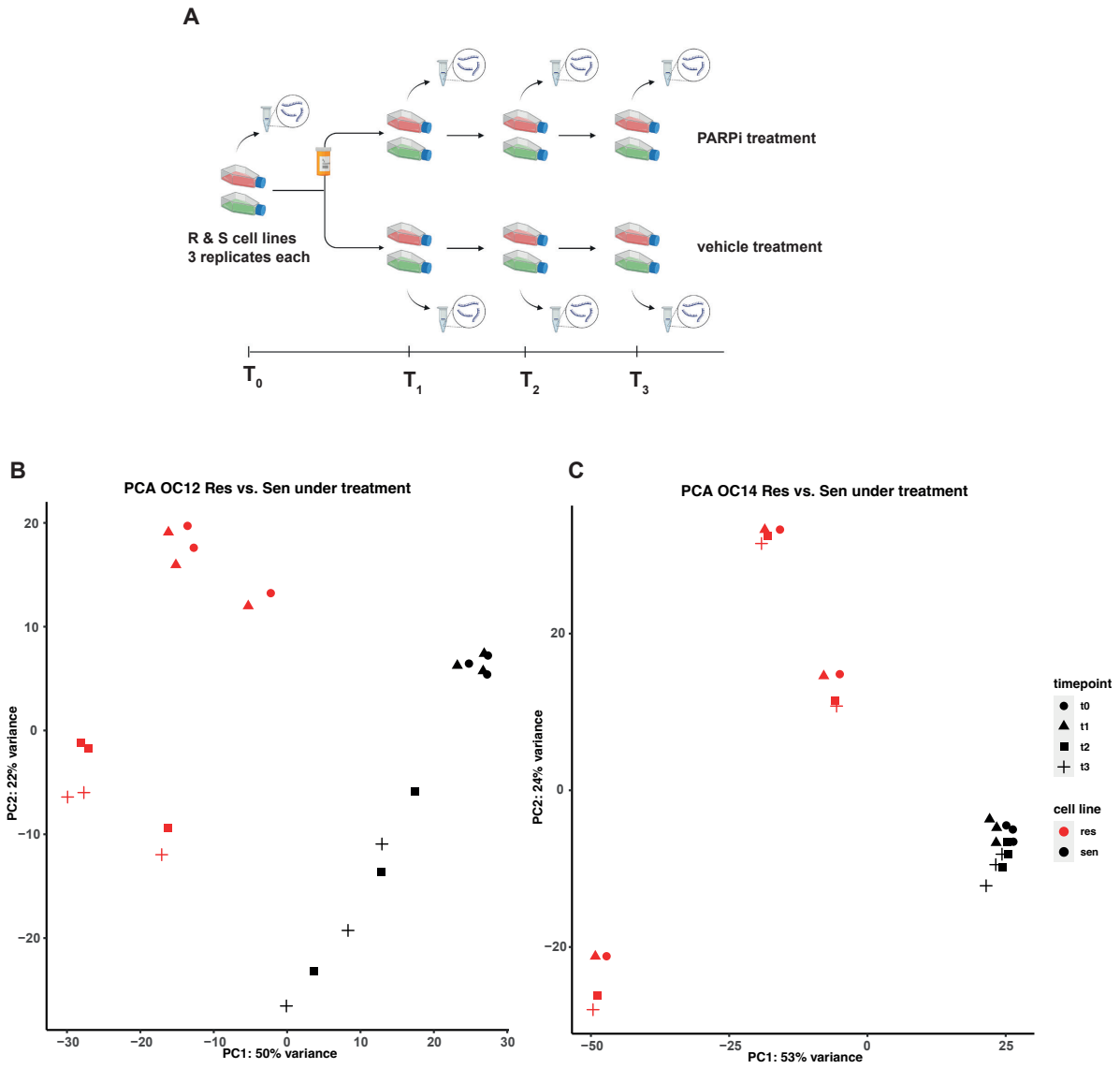

Figure 19 Gene expression analysis of OC12 and OC14 R and S cells under olaparib treatment indicates only slight changes in gene expression between different treatment time points.
A Schematic overview of RNA analysis conducted under olaparib and control treatment, with RNA extraction at various time points. **B** Principal Component Analysis (PCA) of OC12 R and S cells at different time points under olaparib treatment. **C** PCA of OC12 R and S cells at different time points under olaparib treatment. Timepoints indicated as follows: t0 = without any treatment, t1 = 12 hours, t2 = 72 hours, t3 = 120 hours of treatment.

This analysis showed that the differentially regulated pathways present already at steady state (T0) between resistant and sensitive cell lines, were also regulated upon olaparib treatment (suppl. Figure 4 C, E). Interestingly, in the sensitive cells, I observed a significant downregulation of known cell cycle-related pathways such as E2F and G2M checkpoint (suppl. Figure 4 E). For OC14, I observed a similar trend. The OC14 resistant and sensitive cells showed a significant downregulation of MYC targets V1 and V2, E2F, and G2M checkpoint pathways when I compared the gene expression between T3 and T0 (suppl. Figure 4 D, F).

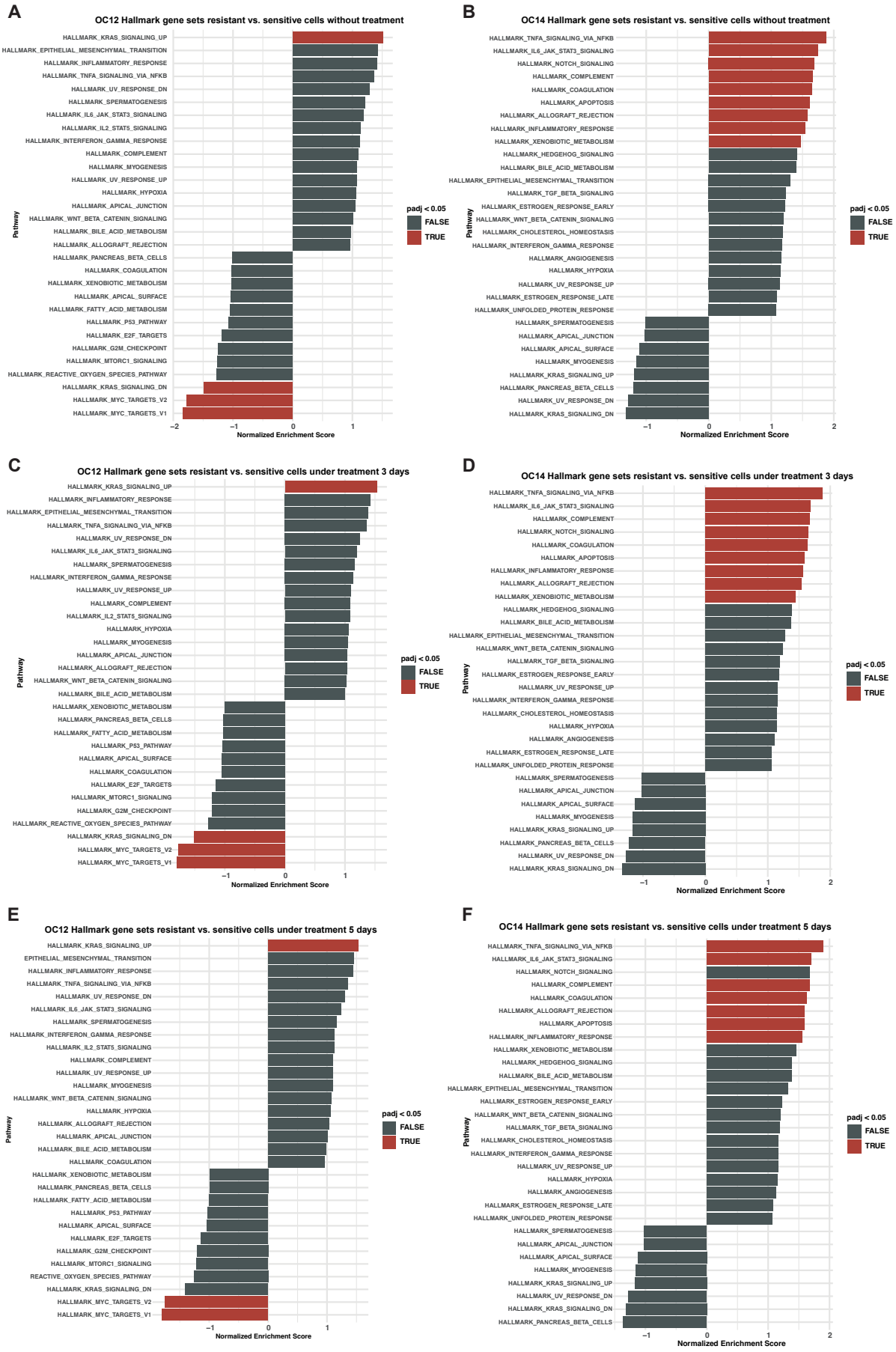

Figure 20 Consistency of RNA Expression in PARPi-Resistant Cells Across Treatment Time Points.

A Gene set enrichment analysis (GSEA) was performed on DEGs between the three OC12 R and S cells without olaparib treatment; displayed are the top 30 Hallmark gene sets. **B** GSEA was performed on DEG between OC14 R (n=3) and S (n = 3) cells without olaparib treatment; the top 30 Hallmark gene sets are shown here. **C** GSEA was performed on DEG between OC12 R (n=3) and S (n = 3) cells after 72h of olaparib treatment; displayed are the top 30 Hallmark gene sets. **D** GSEA was performed on DEG between OC14 R (n=3) and S (n = 3) cells after 72h of olaparib treatment; the top 30 Hallmark gene sets are shown. **E** GSEA was performed on DEG between OC12 R (n=3) and S (n = 3) cells after 120h of olaparib treatment; the top 30 Hallmark gene sets are shown. **F** GSEA was performed on DEG between OC14 R (n=3) and S (n = 3) cells after 120h of olaparib treatment; the top 30 Hallmark gene sets are shown. Statistical significance was evaluated through 10,000 permutations on the phenotype. DEGs were pre-ranked according to their adjusted p-value.

In summary, I identified significant changes in the gene expression between resistant and sensitive cells in both, OC12 and OC14 cell lines. However, under treatment, there were no significant additional changes observed compared to the steady state of the cell lines. This implies that the acquired resistance represents a lasting alteration in the gene expression of the cell lines and is not a reversible plastic response induced by olaparib treatment (suppl. Figure 4 C, E).

4.9 PARPi-resistant cells proliferate and resist senescence under olaparib treatment

Based on the results from the genomic and gene expression analyses of resistant and sensitive cells, the acquired resistance in olaparib-resistant cells is not triggered simply by amplifying or deleting a single gene. It is more likely that the resistance is caused by a phenotypic change affecting multiple molecular pathways. As several cell cycle-related pathways were downregulated in the resistant cells, a plausible explanation for the acquired resistance may involve the induction of senescence in the resistant cells during treatment. Following drug removal, these cells may then subsequently resume to proliferate again. Publications have already shown that olaparib treatment can induce a reversible senescent-like cell state, allowing the cells to re-initiate cell proliferation upon drug removal [149-151].

To investigate whether olaparib treatment induces a senescent-like state in the OC12 or OC14-resistant cell lines, I performed cell proliferation assays with and without olaparib treatment. The cell number was estimated by CTB signal and determined every second day. At first, I performed the assay without treatment to compare the basal proliferation of resistant and sensitive cells. I did not observe a significant difference in cell proliferation as evident in similar doubling times (T_d) between resistant (T_d 2.5) and sensitive (T_d 2.35) OC12 and resistant (T_d 3.5) and sensitive (T_d 3.1) OC14 cells (Figure 21 A, C).

Even though the cell proliferation was similar between resistant and sensitive cells, I observed that both OC12 and OC14 resistant cells showed a change in their phenotype regarding their cell size. Flow cytometry-based experiments showed an increased forward scatter in resistant OC12 and OC1 cells compared to sensitive cells (Figure 21 B, D), indicative of bigger cell size. In addition to flow cytometry, this finding was supported by brightfield microscopy of the cell lines (suppl. Figure 2 A, B).

Having established that there was no disparity in the basal cell proliferation between resistant and sensitive OC12 and OC14 cells, I next aimed to determine whether the resistant cells undergo senescence upon olaparib treatment or persist in continuous proliferation. To test this hypothesis, I treated the three OC12 and OC14 resistant and sensitive cell lines for four days with 2 μM (OC12) or 10 μM olaparib (OC14), killing around 20 % of the cells in the cell viability assay (see Figure 12). DMSO-treated cells were used as control. The cell number at five days under treatment was not significantly different between olaparib-treated resistant cells compared to DMSO-treated resistant and sensitive OC12 (Figure 21 E) and OC14 cell lines (Figure 21 F). In contrast, the cell numbers of the olaparib-treated OC12 and OC14 sensitive cell lines were significantly lower compared to DMSO-treated cells (p = xxx) (Figure 21 E, F). This shows that the resistant cell lines did not undergo senescence during olaparib treatment. Instead, they continued to proliferate while the sensitive cells either ceased to proliferate or underwent cell death under olaparib treatment. Furthermore, there was no significant difference in the cell number detectable three days after drug removal between olaparib-treated resistant and DMSO-treated resistant or sensitive OC12 and OC14 cell lines (Figure 21 E, F). However, the cell number of olaparib-treated OC12 and OC14 resistant cells was lower compared to the DMSO-treated cells on the final day of the experiment (Figure 21 E, F).

To further test if the sensitive cell lines undergo apoptosis or become irreversible senescent under olaparib treatment, I measured the apoptosis rate of each cell line (OC12 R/S#1,2,3 and OC14 R/S#1,2,3). I treated the cells for three days with 10 μM olaparib or DMSO as control and analyzed the percentage of cells undergoing apoptosis by Annexin V/PI staining using flow cytometry (Figure 22 A, D).

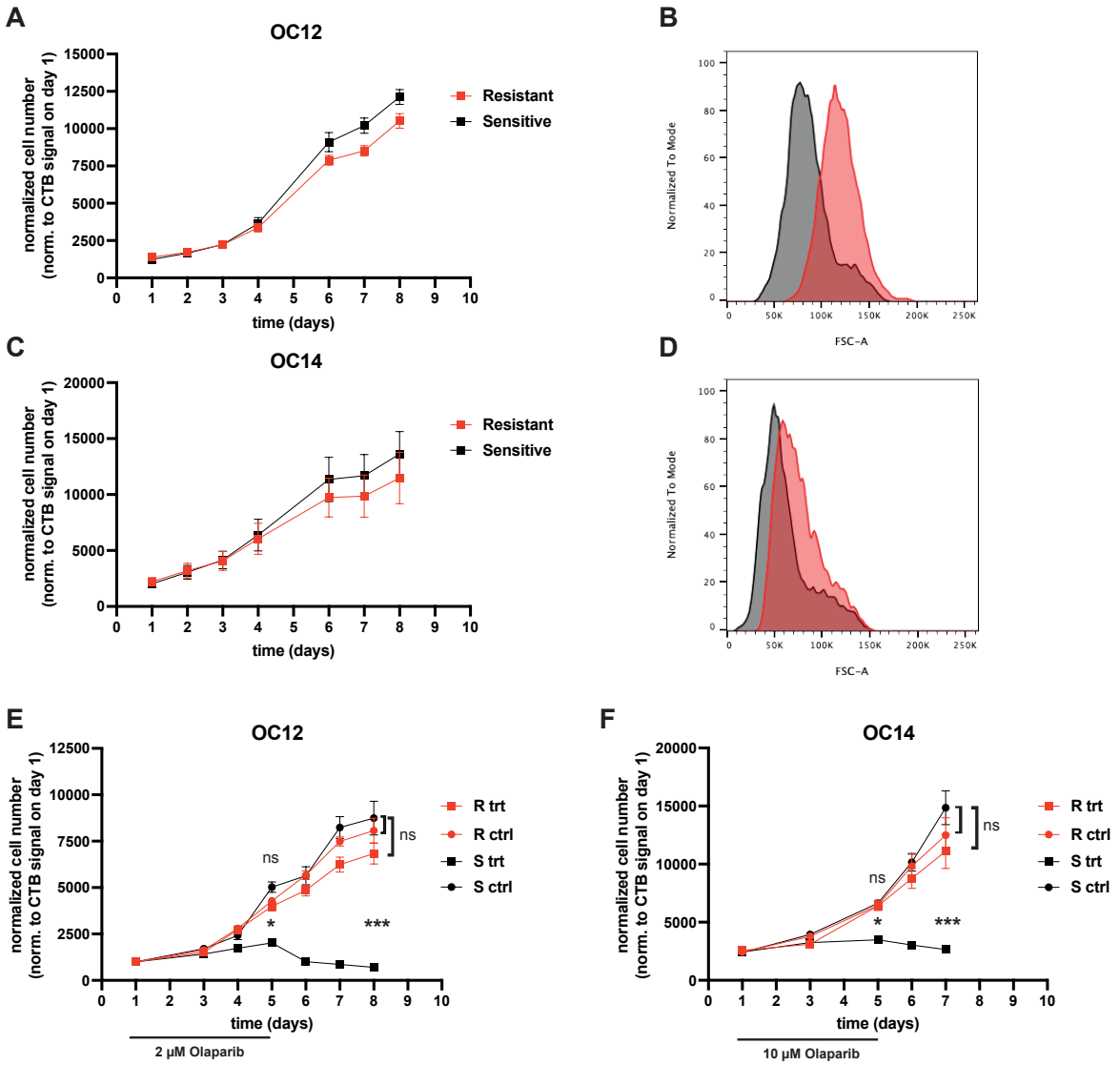

Figure 21 No difference in basal cell proliferation between sensitive and olaparib-resistant cells; under treatment, resistant cells proliferate at the same rate as the sensitive cells.
A Cell count determined by CTB signal readout of OC12 R and S untreated cells at various time points after seeding. The CTB signal was normalized to the CTB signal on day 1. **B** Cell size of OC12 R and S cells was measured using the forward scatter area in flow analysis. **C** Cell count was assessed through CTB signal readout of OC14 R and S untreated cells at different time points after seeding. The CTB signal was normalized to the CTB signal on day 1. **D** Cell size of OC14 R and S cells determined by the forward scatter area in flow analysis. **E** Cell count based on CTB signal readout of OC12 R and S cells, either treated with 2 µM olaparib or DMSO as a control for 4 days (indicated by the black bar below the plot). After 4 days, the drug was removed, and cells were cultured in media um without any treatment. The CTB signal was normalized to the CTB signal on day 1. **F** Cell count based on CTB signal readout of OC14 R and S cells, either treated with 10 µM olaparib or DMSO as a control for 4 days (indicated by the black bar below the plot). After 4 days, the drug was removed, and cells were cultured in media um without any treatment. P-values were calculated for each time point using a nonparametric Mann-Whitney test; * $p < 0.05$, ** $p < 0.01$, *** $p < 0.001$; ns, insignificant.

As expected, only a minor fraction of OC12 (Figure 22 A -C) and OC14 (Figure 22 D - F) resistant cells (20 – 25 %) underwent apoptosis upon olaparib treatment. The observation that 1/5 of the resistant cells undergo apoptosis under treatment could potentially account for the reduced cell number of the resistant cells at the end of the cell proliferation assay compared to untreated cell lines (Figure 21 E, F). In contrast, over 70 % of the sensitive OC12 and OC14

cells underwent cell death via apoptosis when treated with 10 µM olaparib (Figure 22 C, F). These results indicate that olaparib treatment induced in both OC12 and OC14 resistant cells significantly less apoptosis compared to sensitive cells.

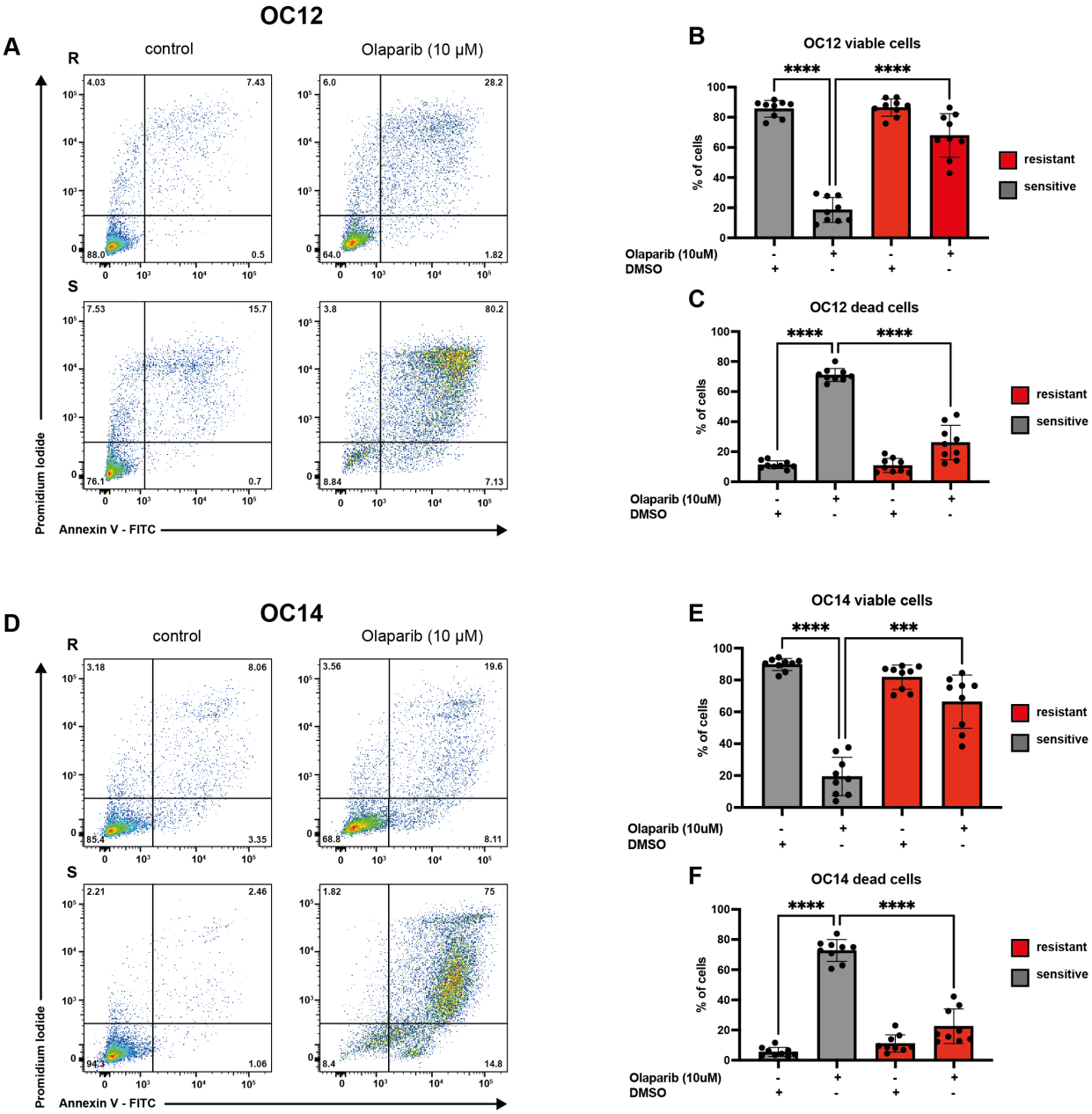

Figure 22 Reduced apoptosis in OC12 and OC14 R cells compared to S cells.
Scatter plots and quadrants of Annexin V and Propidium Iodide (PI) staining for OC12 R (top row) and S (bottom row) cells with and without olaparib treatment. Cells were treated for 3 days with 10 µM olaparib or DMSO as a control. **B** Percentage of viable OC12 R and S cells with and without olaparib treatment. **C** Percentage of apoptotic/dead OC12 R and S cells with and without olaparib treatment. **D** Scatter plots and quadrants of Annexin V and PI staining of OC14 R (top row) and S (bottom row) cells with and without olaparib treatment. Cells were treated for 3 days with 10 µM olaparib or DMSO as control. **E** Percentage of viable OC12 R and S cells with and without olaparib treatment. **F** Percentage of apoptotic/dead OC12 R and S cells with and without olaparib treatment. P-values were calculated using a one-way ANOVA test with Geisser-Greenhouse correction; * $p < 0.05$, ** $p < 0.01$, *** $p < 0.001$; ns, insignificant

4.10 Sensitive cell lines are stalled in the G2M phase upon olaparib treatment

It has been shown that cells treated with DNA-damaging agents are arrested in the G2M phase of the cell cycle to repair acquired DNA damage before entering the S-phase. To investigate this for OC12 and OC14 cells, I performed a cell cycle analysis based on 5-Brom-2'-deoxyuridine (BrdU) incorporation to determine if resistant or sensitive cells are arrested in a specific cell cycle phase. I treated the three resistant and three sensitive OC12 and OC14 cell lines for 24h or 72h with 10 μM olaparib or DMSO as a control. The cells were incubated with BrdU for 2h, fixed and stained with a FITC anti-BrdU antibody, and analyzed by flow cytometry.

The distribution of OC12 and OC14 resistant cells in each cell cycle state (G1, S, G2M-phase) remained stable during olaparib treatment for 24h and 72h (Figure 23 A, Figure 24 A). The proportion of cells present in the G2M phase upon olaparib treatment was only slightly increased for OC12-resistant cells (ctrl: 20 %, 24h: 30 %, 72h: 30 %) (Figure 23 C, E), and the same was true for OC14 resistant cells (ctrl: 20 %, 24h: 25 %, 72h: 25 %) (Figure 24 A – C). In the case of the sensitive cells, I observed a significant increase in the number of cells in the G2M phase upon olaparib treatment. After 24h of treatment, 60 % of the OC12 sensitive cells (Figure 23 B, C) and 40 % of the OC14 sensitive cells (Figure 24 B, C) were in the G2M phase compared to 20 % in the control setting. This observation was even stronger after 72h of olaparib treatment, at which 80 % of the OC14 sensitive (Figure 24 D, E) cells and 55 % of the OC12 sensitive cells (Figure 23 D, E) were in the G2M phase, compared to 15 % (OC14) and 20 % (OC12) in the control setting.

In summary, olaparib treatment resulted in a stalling of sensitive cells in the G2M phase of the cell cycle. In contrast, the proportion of olaparib-resistant cells in each cell cycle state did not change significantly, indicating that resistant cells are still actively cycling under treatment. These findings also align with the previous cell viability assay (see 4.2) and cell proliferation assays (see 4.9), in which most of the sensitive cells did not proliferate and finally underwent apoptosis when treated with olaparib.

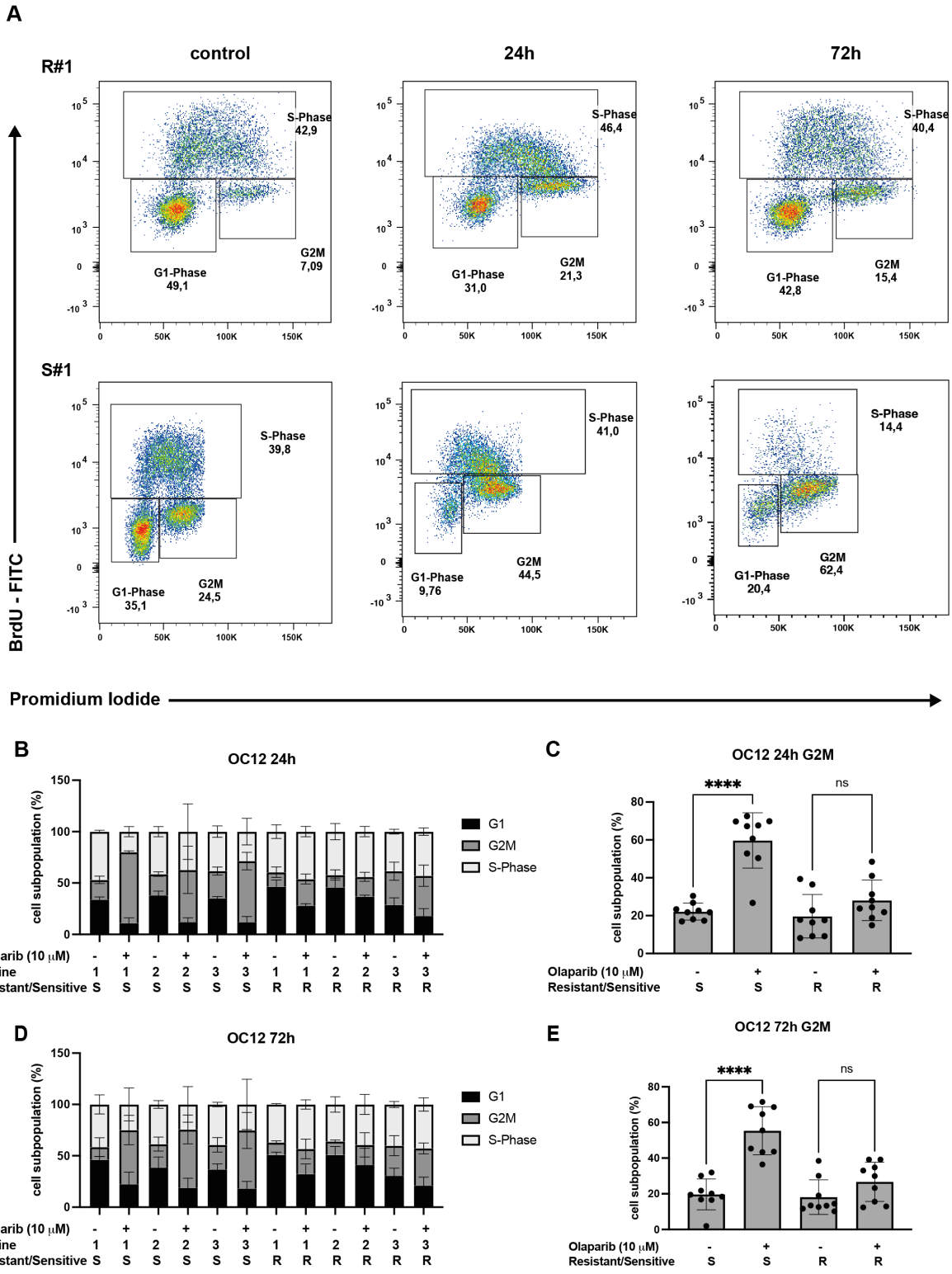

Figure 23 Differential cell cycle responses: OC12 S cells stalled in G2M phase, R cells continue cycling under treatment. **A** Scatter plots of BrdU and Propidium Iodide (PI) staining, with gates indicating G1-, S- and G2M cell cycle phases based on staining characteristics. Cells were treated for 24 and 72 hours with 10 µM olaparib or DMSO as a control. **B** Quantification of cell cycle phase distribution of OC12 R and S cells after 24h of treatment. **C** Quantification of OC12 R and S cells, which are in the G2M phase after 24h of treatment. **D** Quantification of cell cycle phase distribution of OC12 R and S cells after 72h of treatment. **E** Quantification of OC12 R and S cells in the G2M phase after 72h of treatment. P-values were calculated using a one-way ANOVA test with Geisser-Greenhouse correction; * $p < 0.05$, ** $p < 0.01$, *** $p < 0.001$; ns, insignificant.

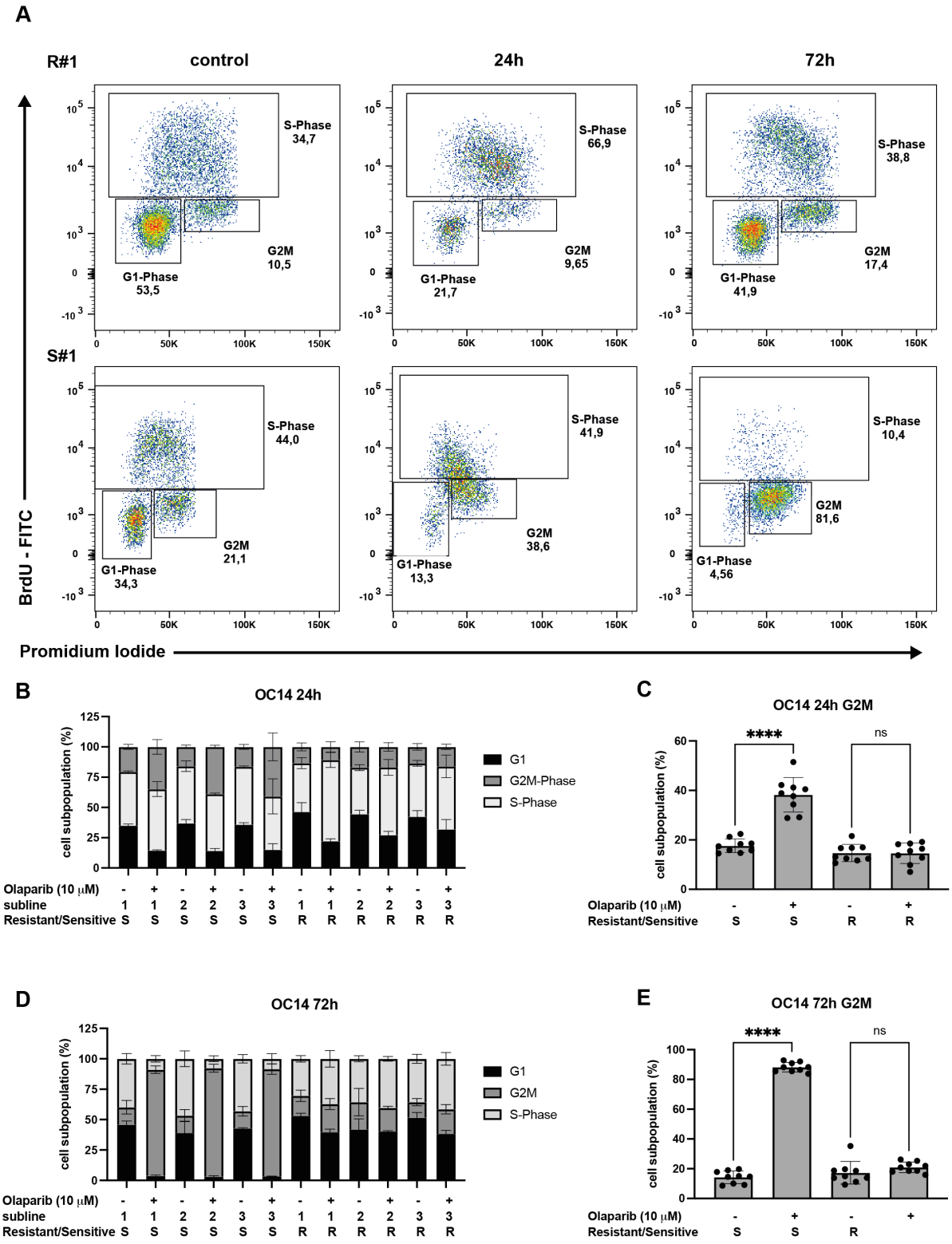

Figure 24 Differential cell cycle responses: OC14 S cells stalled in G2M phase, R cells continue cycling under treatment. **A** Scatter plots of BrdU and PI staining are provided, with gates indicating G1-, S-, and G2M cell cycle phases based on staining characteristics. Cells were treated for 24 and 72 hours with 10 µM olaparib or DMSO as a control. **B** Quantification of cell cycle phase distribution of OC14 R and S cells after 24h of treatment. **C** Quantification of OC14 R and S cells in the G2M phase after 24h of treatment. **D** Quantification of cell cycle phase distribution of OC14 R and S cells after 72h of treatment. **E** Quantification of OC14 R and S cells in the G2M phase after 72h of treatment. P-values were calculated using a one-way ANOVA test with Geisser-Greenhouse correction; * $p < 0.05$, ** $p < 0.01$, *** $p < 0.001$; ns, insignificant.

4.11 Olaparib-resistant OC12 cells have a significantly higher maximal respiration rate compared to sensitive cells

Based on the GSEA results between olaparib-resistant and sensitive OC12 and OC14 cell lines, oxidative phosphorylation was down-regulated in the olaparib-resistant cells compared to the sensitive OC12 and OC14 cells (Figure 25 A, B). To functionally validate these results, I performed Mito Stress assays measuring mitochondrial respiration activity using Agilent Seahorse technologies. The Mito Stress assay allows for simultaneous measurement of multiple parameters of cell metabolism, including basal and maximal respiration activity. Differences in metabolic activity between resistant and sensitive cells might contribute to olaparib resistance. The protocol involves three serial injections of inhibitors and activators (oligomycin, FCCP, and rotenone/antimycin A) targeting different complexes of the electron transport chain in mitochondria (oligomycin – inhibits ATP Synthase; FCCP – activates PINK1; rotenone/antimycin A – inhibit complex I and II).

The first replicate of this experiment was conducted in cooperation with Dr. Sarah-Jane Neuberth.

I conducted the assay with the three OC12 and OC14 resistant and sensitive cell lines and treated the cells with 10 μM olaparib or DMSO for 72 h. The first three measurements of the assay indicate the cells' basal oxygen consumption rate (OCR) (Figure 25 C, D). In OC12 resistant cells, I observed a slight but insignificant increase in basal OCR compared to sensitive cells (FC of 1.5) (Figure 25 C, E). Interestingly, this observed effect was independent of olaparib or DMSO treatment. The maximal respiration rate, measured at the three time points after FCCP injection, was significantly increased (FC of 2) in olaparib-resistant cells compared to sensitive cells (Figure 25 C, G), again independent of olaparib treatment. This significant change in the maximal respiration rate might indicate a change in the energy metabolism between OC12 resistant and sensitive cells. Resistant cells may rely more on oxidative phosphorylation already at their steady state compared to sensitive cells that use glycolysis to meet their ATP demand. In OC14 cells, I did not observe any significant effect between resistant and sensitive cells in regard to oxidative phosphorylation, only OC14 R#2 showed higher basal and maximal respiration rates compared to the sensitive and the other two resistant OC14 cell lines (Figure 25 F, H). These results show that only one out of three olaparib-resistant OC14 cell lines (R#2) switched the metabolic phenotype compared to the sensitive cell lines. In contrast, all three olaparib-resistant OC12 lines showed a metabolic shift

toward an increased oxidative phosphorylation. These data suggest that metabolic re-wiring may in some cells contribute to olaparib resistance but not in all cells.

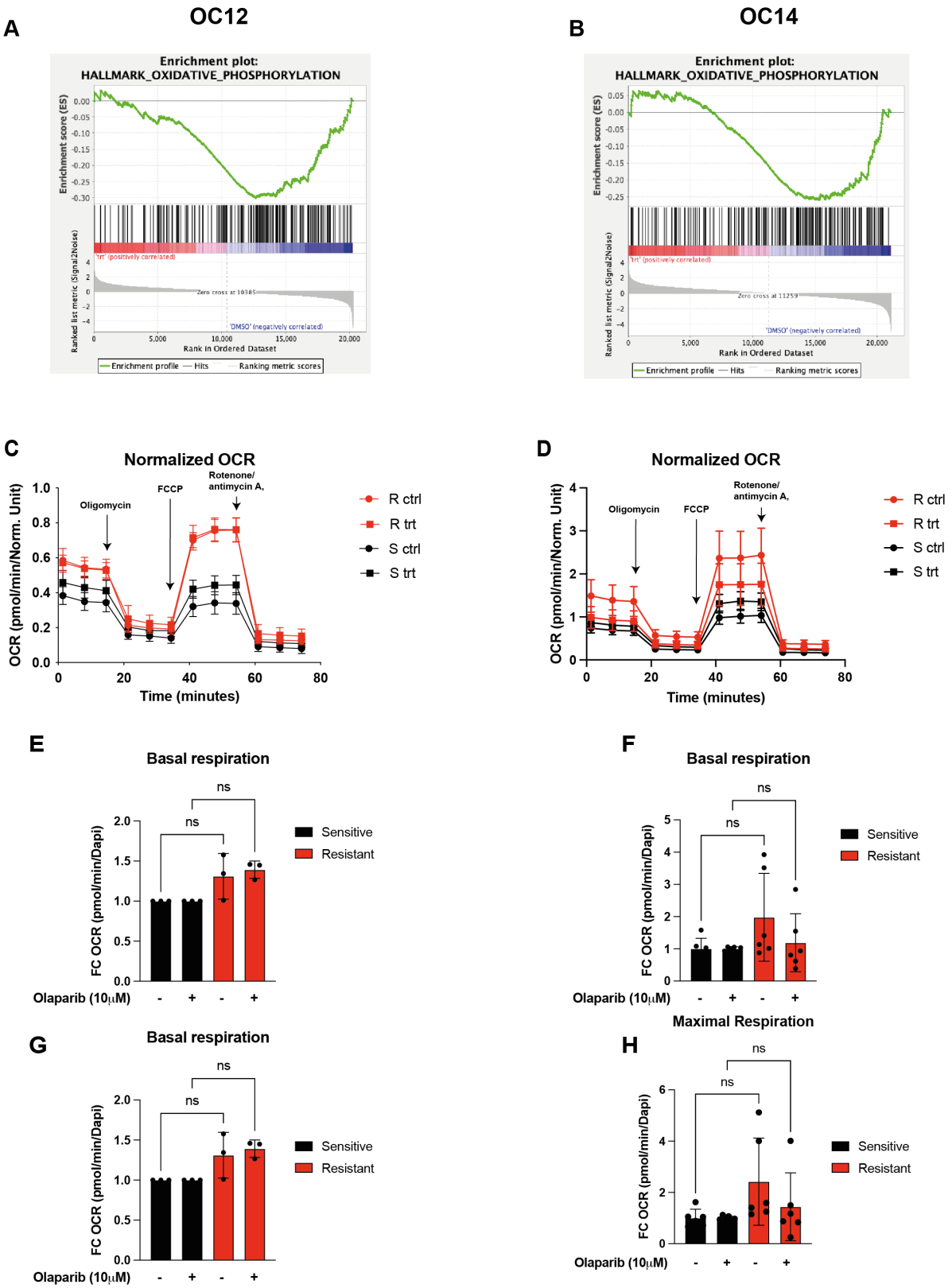

Figure 25 OC12 R cells show an increased maximal respiration rate compared to S cells.
A GSEA was conducted between the three R and three S OC12 cells, Hallmark Oxidative Phosphorylation gene set is shown. Statistical significance was assessed with 10,000 permutations on the phenotype, and all differentially expressed genes were pre-ranked based on the adjusted p-value. **B** Gene Set Enrichment Analysis between the three R and three S OC14 cells,

focusing on the Hallmark Oxidative Phosphorylation gene set. **C** Representative Mito Stress experiment in OC12 R and S cells (n = 3 groups with 6 replicates/group) treated with 10 µM olaparib or DMSO as a control for 24 hours. Three inhibitors, oligomycin, FCCP, and rotenone/antimycin A, were serially injected at indicated time points. Error bars represent the mean ± SD. OCR stands for oxygen consumption rate. **D** Representative Mito Stress experiment in OC14 R and S cells (n = 3 groups with 6 replicates/group) treated with 10 µM olaparib or DMSO as a control for 24 hours. **E** Quantification of basal respiration of OC12 R and S cells with and without olaparib treatment. **F** Quantification of basal respiration of OC14 R and S cells with and without olaparib treatment. **G** Quantification of maximal respiration of OC12 R and S cells with and without olaparib treatment. **H** Quantification of maximal respiration of OC12 R and S cells with and without olaparib treatment. P-values were calculated for three independent experiments using a one-way ANOVA test; * $p < 0.05$, ** $p < 0.01$; ns, insignificant.

4.12 No difference in DNA damage repair capacity between olaparib-resistant and sensitive cells

Since many PARPi resistance mechanisms are caused by alterations to DNA damage repair, such as the reintroduction of HR in HR deficient cells, inhibition of NHEJ, or stabilization of the replication fork. I wanted to investigate further DNA repair-related aspects in olaparib-resistant and sensitive OC12 and OC14 cells. I performed multiple complimentary assays to analyze DNA damage response, including comet assay, RAD51 & yH2A.X IF staining, DNA repair reporter assay, and western blot analysis.

The comet assay enables the detection of damaged DNA. Due to its negative charge, DNA can be separated in an agarose gel by electrophoresis. Cells with a high amount of DNA damage will exhibit numerous small DNA fragments, which migrate faster away from the nucleus towards the positively charged anode. Following electrophoresis, the DNA is stained with a DNA dye; in my case using SYBR Green. Afterward, fluorescence microscopy is employed to analyze the gel, measuring the amount of fluorescence in the head (nucleus) and the tail (fragmented DNA). The readout is directly proportional to the extent of DNA damage. I calculated the Olive Tail Moment (OTM) as an arbitrary-unit measure of DNA strand breaks, calculated by the percentage Tail DNA content multiplied by the Tail Moment Length. The comet assay is a valuable tool for detecting DNA damage from SSBs and DSBs, and allows the analysis of DNA repair speed and capacity in cells [152].

The comet assays were performed with Dr. Ali Bakr from AG Plass at the DKFZ.

As I induced resistance to PARPi by treating the cells with escalating doses of olaparib, distinct cell populations might be present within the parental OC12 and OC14 cell lines with differing levels of endogenous DNA damage. Cells with lower levels of endogenous DNA damage may have a greater resistance to PARPi treatment than cells with higher levels of endogenous DNA

damage. Assuming that the sensitive cells would have massively more endogenous DNA damage compared to the resistant cell lines, the treatment with DNA damaging agents would have a stronger effect on those cells with higher levels of DNA damage.
To test this hypothesis, I conducted a comet assay to assess the extent of endogenous DNA damage in both resistant and sensitive OC12 and OC14 cell lines. By calculating the OTM, I observed no difference in the level of DNA damage between the OC12 (Figure 26A - C) and OC14 resistant and sensitive cell lines (Figure 26 A, D, E) under control conditions without any treatment. This finding indicates that there is no difference in endogenous DNA damage between the resistant and sensitive cell lines, suggesting that this factor does not account for the observed resistance to olaparib.

As previously mentioned, the comet assay is valuable for assessing cellular responses to DNA damage, including DNA repair capacity and speed. Therefore, I induced DNA damage through ionizing radiation (IR), applying a uniform dose of 4 Gray (Gy) to ensure simultaneous DNA damage in all cells. This approach facilitates a simultaneous induction of DNA repair compared to the use of DNA-damaging drugs. To elucidate the kinetics of DNA repair in both resistant and sensitive cells, I calculated the OTM of 200 nuclei at five different time points (1, 10, 20, 30, and 60 minutes post-irradiation).

I did not detect a striking difference between resistant and sensitive OC12 and OC14 cells in their OTM 1-minute post-IR (OC12 R#1: 29.9, S#1: 28.6; OC14 R#1 39.7, S#1 39) (Figure 26). In OC12, the OTM decreased in both resistant (R#1) and sensitive (S#1) cell lines ten minutes post-IR (R#1: 21, S#1: 16) and continued to reduce over time, reaching 60 min post-IR an OTM of 9.9 and 7.1 in resistant (R#1) and sensitive (S#1) cells, respectively (Figure 26 B, C). In OC14, the OTM for sensitive cells (S#1) remained at 39.25, while for resistant cells (R#1) it decreased to 27. At 20 minutes post-IR, both cell lines exhibited a similar OTM, 22.2 and 16.4 in sensitive (S#1) and resistant (R#1) cells, respectively. By the final time point (OC14 30 min; OC12 60 min), both cell lines demonstrated similar OTMs, with sensitive cells (S#1) at 19.8 and resistant cells (R#1) at 18.9 (Figure 26 D, E). These findings indicate that both resistant and sensitive OC12 and OC14 (R#1 and S#1) cell lines are proficient in DNA repair induced by IR.

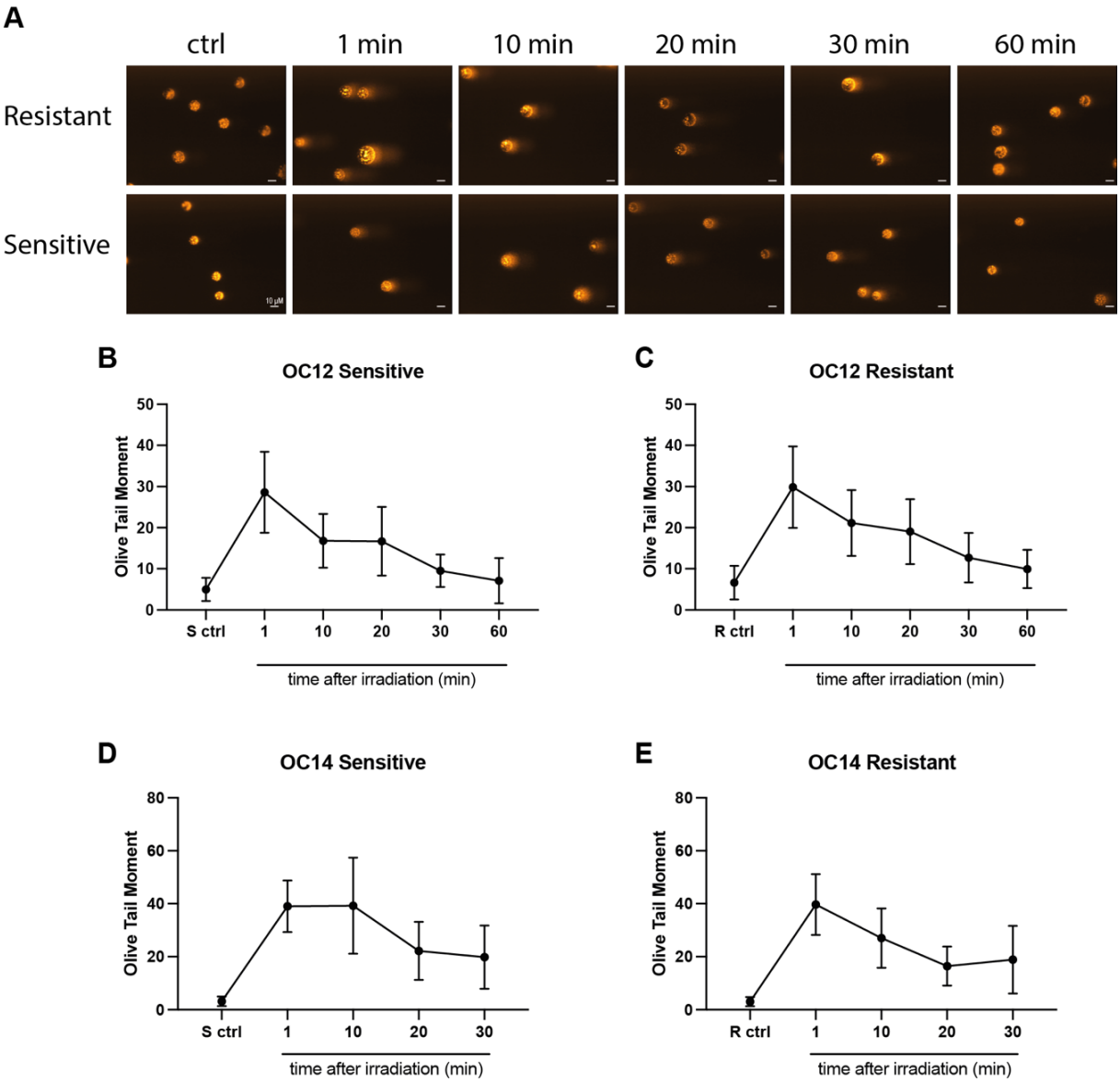

Figure 26 There was no difference in DNA damage response between resistant and sensitive OC12 and OC14 cell lines after irradiation.
A Representative images of the alkaline comet assay conducted on OC12 R#1 and S#1 cells. The time indicated is the duration after irradiation (4 Gy), at which point cells were fixed in agarose. Subsequently, fixed cells underwent electrophoresis, followed by DNA labeling with SYBR Green. Scale bar = 10 μm. **B and C** Quantification of Olive tail moment measured from 200 cells/timepoint of OC12 S (B) and R cells (C). **D and E** Quantification of Olive tail moment measured from 200 cells/timepoint of OC14 S (B) and R cells (C). Data is represented as mean ± SD.

The mechanism of action for PARPis is based on a deficiency in HR, rendering the cells susceptible to the induction of DSB as they then rely on the error-prone NHEJ pathways. WGS results (Figure 10) indicated the absence of mutations in HR genes for both OC12 and OC14 cells. However, it is known that epigenetic modifications, such as promoter region methylations of HR genes, can also contribute to HRD [153-155]. To investigate whether OC12 and OC14 cell lines are HR proficient or HR deficient, I performed fluorescence microscopy staining for RAD51 and γH2AX, which are well-established markers for DSBs and HR repair. Following DSB induction, histone H2A.X undergoes phosphorylation at Ser139 by PI3K kinases

(ATM, ATR, and DNA-PK) within minutes, making it a suitable marker for DSBs in cells. RAD51, a crucial player in homologous strand exchange, represents one of the key and final steps during HR and is widely utilized as a marker for proficient HR repair [156].

The first replicate of IF staining for RAD51 and γH2A.X was performed with Dr. Ali Bakr from AG Plass at the DKFZ.

To assess the proficiency or deficiency of HR in the resistant and sensitive cells, I performed IF staining for RAD51 and γH2A.X, treating the cells with either ionizing radiation (IR) as a positive control or 10 µM olaparib for 24 h or 48 h and DMSO treatment for 48 h as a control.

In the case of OC12 cells (R#1 and S#1), there was no significant difference in the number of γH2A.X foci upon IR treatment between resistant (8.6 foci/nucleus) and sensitive cells (9.5 foci/nucleus) (Figure 27 A, B). Treatment with 10 µM olaparib for 24 or 48 hours led to an increase in γH2A.X foci in both resistant (24 h: 16.5 foci/nucleus; 48 h: 16.8 foci/nucleus) and sensitive cells (24 h: 11.3 foci/nucleus; 48 h: 14.1 foci/nucleus) (Figure 27 B), indicating comparable DNA damage induction by IR and olaparib in both cell types.

Analysis of RAD51 foci upon DNA damage induction by IR revealed no significant difference between olaparib-resistant (6.1 foci/nucleus) and sensitive (5.7 foci/nucleus) OC12 cells (Figure 27 C). Furthermore, after 24 h or 48 h treatment with 10 µM olaparib, no significant difference was observed in the number of RAD51 foci between olaparib-resistant (24 h: 10.6; 48 h: 13.1 foci/nucleus) and sensitive cells (24 h: 12.3; 48 h: 20.1 foci/nucleus) (Figure 27 C). These findings suggest that both olaparib-resistant and sensitive cells are generally proficient in HR. Notably, at 48 h of olaparib treatment, I detected a strong but insignificant difference ($p = 0.057$) between resistant and sensitive cells (R#1 13.1 vs S#1 20.1 foci/nucleus). This may indicate a potential shift to NHEJ in resistant cells after 48 h of olaparib treatment, as the levels of γH2A.X foci at 48 h are similar in both olaparib-resistant and sensitive cell lines (Figure 27 B).

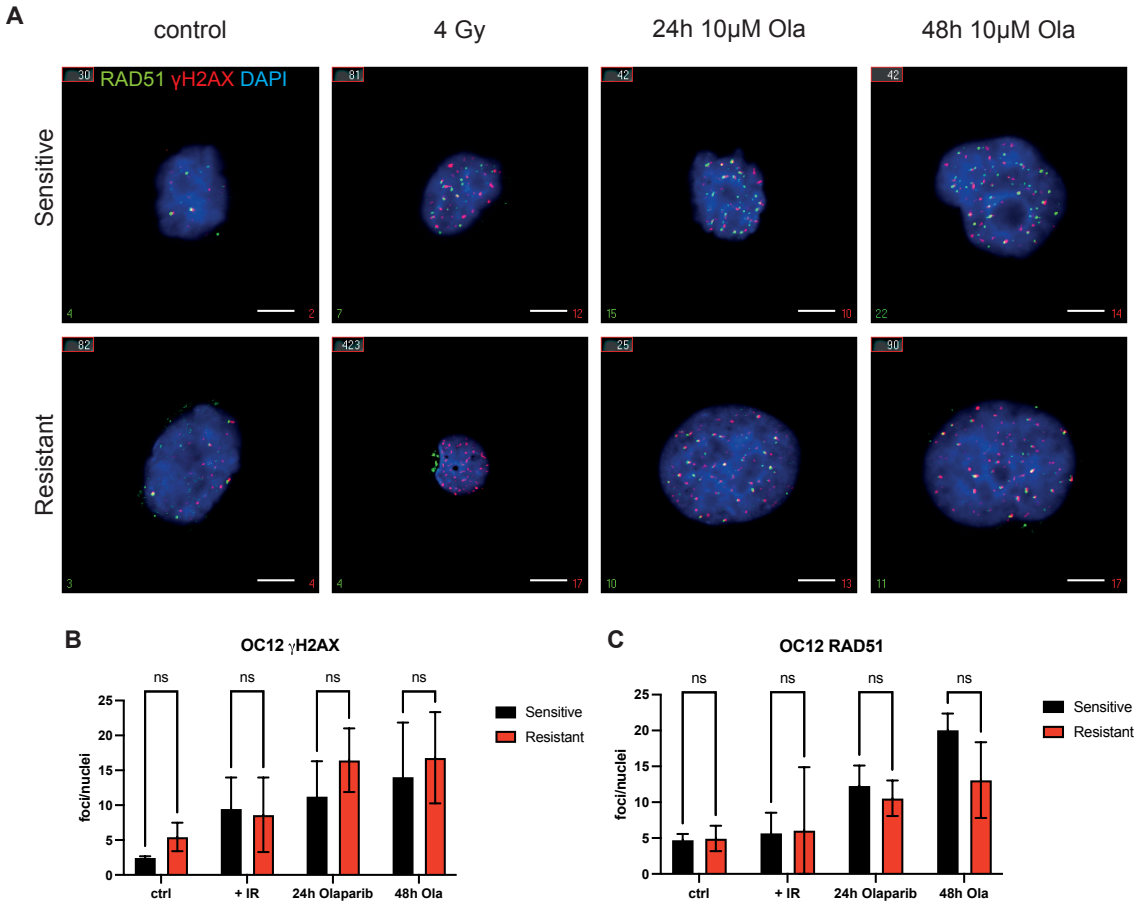

Figure 27 No significant difference in HR DNA repair between the R and S OC12 cells after olaparib treatment.
A Representative images of OC12 R#1 and S#1 cells stained for Rad51- and γH2A.X foci. Cells were either untreated, irradiated with 4 Gy, or treated with 10 µM olaparib for 24 h or 48 h. Cells were fixed in 4 % PFA and stained as outlined in the methods section 3.15. Scale bar = 10 µM, images were additionally sharpened for better visualization (see methods section), and foci quantification was based on original pictures. **B** Quantification of γH2A.X foci in OC12 R#1 and S#1 cells based on 3 experiments with 500 nuclei analyzed per condition. **C** Quantification of Rad51 foci in OC12 R#1 and S#1 cells based on 3 experiments with 500 nuclei analyzed per condition. Statistical analysis was performed using an unpaired, nonparametric Mann-Whitney test.

For OC14 resistant (R#1) and sensitive (S#1) cells, the analysis of γH2A.X foci following irradiation (4 Gy) revealed a slight, non-significant difference (p = 0.11). Resistant cells (R#1) had 7.8 foci/nucleus, while sensitive (S#1) had only 3.3 foci/nucleus (Figure 28 A, B). Under olaparib treatment (24 or 48 h), I did not observe any visible difference in the number of γH2A.X foci/nuclei (Figure 28 A, B).

Analyzing RAD51 foci in both resistant and sensitive OC14 cells following irradiation (4 Gy), I did not detect a significant difference between resistant (R#1) (9.8 foci/nucleus) and sensitive cells (S#1) (10.6 foci/nucleus) (Figure 28 A, C). Following olaparib treatment (10 µM for 24 h), the sensitive cells (S#1) showed a slight but insignificant increase in RAD51 foci/nucleus (20.3 foci/nucleus) compared to resistant cells (R#1) (14.7 foci/nucleus) (Figure 28 C). In contrast,

after 48 h of olaparib treatment, resistant cells (R#1) showed a slightly higher number of RAD51 foci (11.5 foci/nucleus) compared to sensitive cells (S#1) (6.9 foci/nucleus) (Figure 28 C).

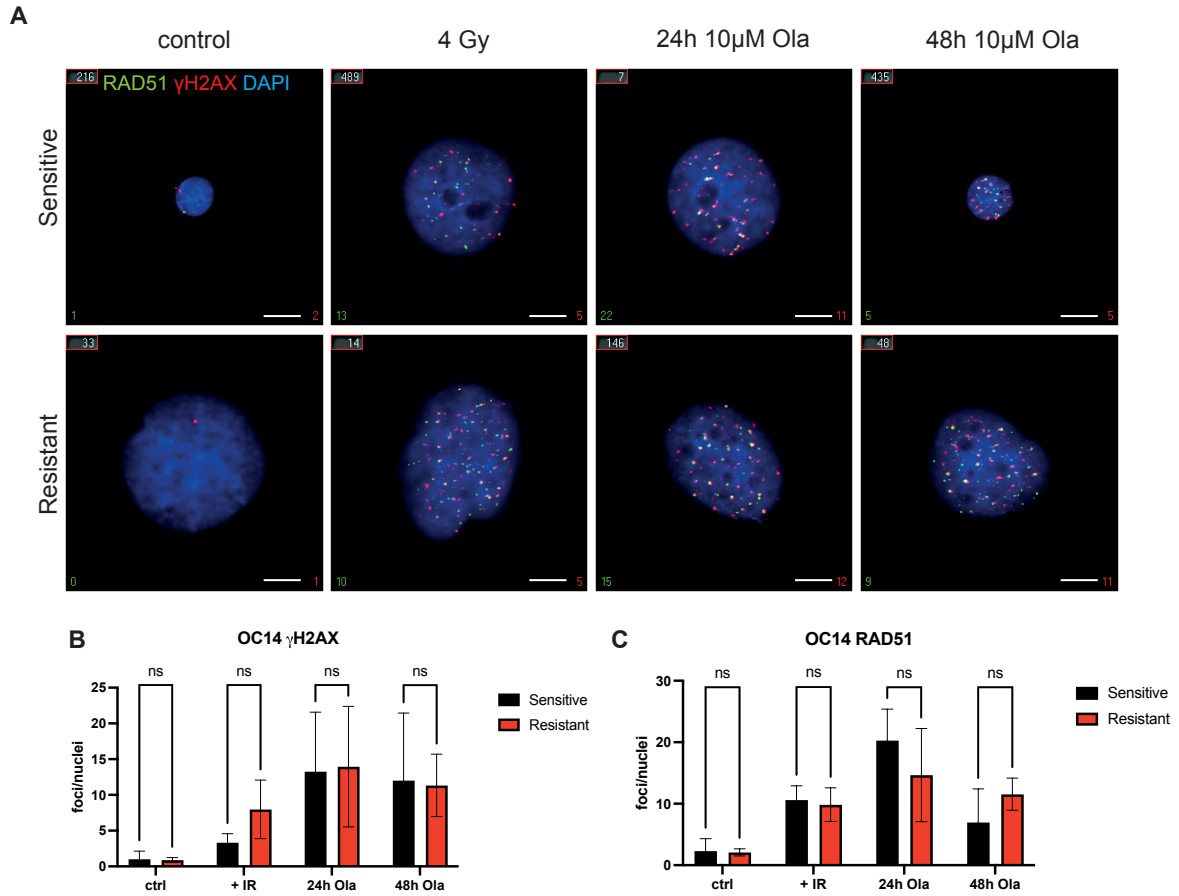

Figure 28 No significant difference in HR DNA repair between the R and S OC14 cells after olaparib treatment.
A Representative images of OC14 R#1 and S#1 cells stained for Rad51- and γH2A.X foci. Cells were either untreated, irradiated with 4 Gy, or treated with 10 µM olaparib for 24 or 48 h. Cells were fixed in 4 % PFA and stained as outlined in the methods section 3.15. Scale bar = 10 µM, images were additionally sharpened for better visualization (see methods section), and foci quantification was based on original pictures. **B** Quantification of γH2A.X foci in OC14 R#1 and S#1 cells based on 3 experiments with 500 nuclei analyzed per condition. **C** Quantification of Rad51 foci in OC14 R#1 and S#1 cells based on 3 experiments with 500 nuclei analyzed per condition. Statistical analysis was performed using an unpaired, nonparametric Mann-Whitney test.

In summary, these results suggest proficiency in HR for both OC14 resistant (R#1) and sensitive (S#1) cells, as indicated by RAD51 foci upon DNA damage induction. However, no significant difference was observed in the number of RAD51 foci, indicating comparable HR performance in the two cell lines.

In addition to RAD51 and γH2A.X analysis based on IF microscopy, I took advantage of a reporter cassette system termed “traffic light” which gives information about the DNA repair pathway the cells employ to repair an induced DSB. The reporter system is based on a reporter cassette containing a nuclease cleavage site (I-SceI), and repair of this break leads to distinct fluorescence signals upon DNA repair via HR (*eGFP*) with an exogenous donor template or via NHEJ (*mCherry*), which can be measured and analyzed by flow cytometry [157].

I utilized the traffic light reporter system in resistant and sensitive OC12 (R#1 and S#1) cells to examine the DNA repair pathway activated following DSB induction. I introduced the I-SceI nuclease via viral transduction, inducing a DSB at a specific locus within the reporter cassette (see Figure 29 A). I confirmed the successful transduction of the nuclease-carrying virus by the expression of blue fluorescent protein (BFP), serving as a marker for the analyzed cell population (see Figure 29B). Additionally, the viral construct contained the donor template essential for HR repair of the induced DSB.

Theoretically, an increase in virus carrying the donor templates is expected to enhance DNA repair through HR relative to NHEJ. Indeed, when I increased the amount of virus delivering the donor template, OC12 resistant (R#1) and sensitive (S#1) cells increasingly utilized HR for repairing the induced DSBs (Figure 29 C, D). At a multiplicity of infection (MOI) of 5, 0.5 % of resistant (R#1) and sensitive (S#1) cells utilized HR for DSB repair, and at an MOI of 50, 1 % of the resistant (R#1) and sensitive (S#1) cells performed HR. Notably, at the highest MOI of 100, 1.25 % of sensitive (S#1) and 1.5 % of resistant (R#1) cells engaged HR for DSB repair (Figure 29 D). The difference between resistant (R#1) and sensitive (S#1) cells utilizing HR was marginal and evident only at the highest MOI of 100, suggesting comparable HR proficiency in both OC12 cell lines.

Interestingly, OC12 resistant (R#1) cells demonstrated a higher tendency for NHEJ compared to sensitive (S#1) cells (MOI of 5: R#1 1 %, S#1 0.6 %; MOI of 100: R#1 1.5 %, S#1 1 %) (Figure 29E). This observation suggests that the olaparib-resistant OC12 cells may exhibit HR proficiency similar to sensitive cells but have an increased capacity for NHEJ in DSB repair. This elevated NHEJ capability might enhance their ability to manage PARPi-induced DNA damage, conferring greater resistance to PARPi than sensitive cells.

To also assess whether chromatin bound DNA-repair proteins change upon DNA damage induction, I exposed olaparib-resistant and sensitive OC12 and OC14 cells (R#1, S#1) to 4 Gy IR and harvested the chromatin bound protein fraction 1, 2 and 6 h post-IR, with untreated samples serving as control. I observed that all analyzed DNA-repair proteins were already present in the control setting as well as in the DNA-damage samples (suppl. Figure 5 OC12: A, OC14: B), supporting the findings of the “traffic light” assay.

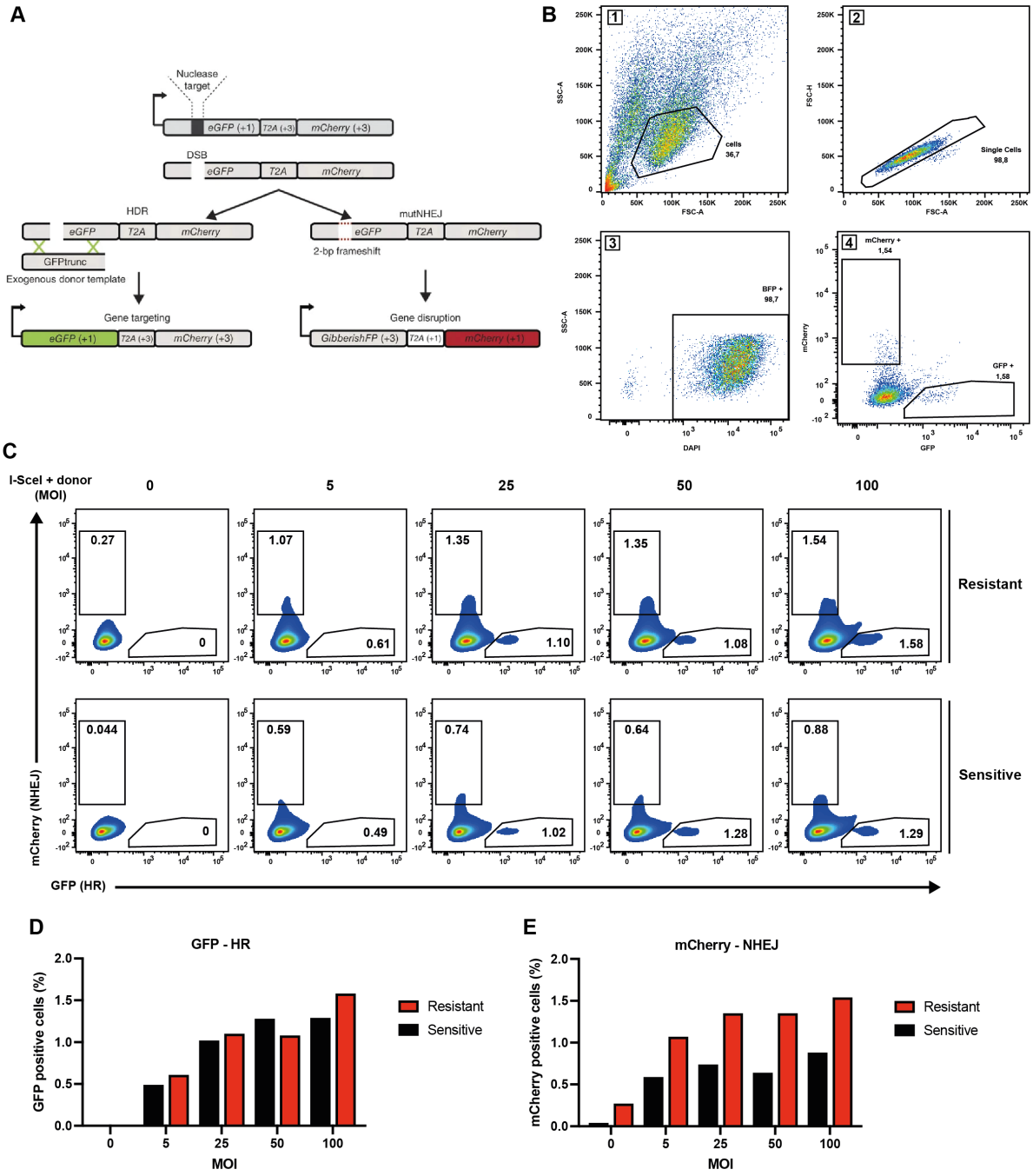

Figure 29 OC12 R and S cells show similar DNA damage responses to induced DSBs.
A schematic overview of the traffic light reporter system, displaying the different outcomes after induction of a DSB. If the DSB is repaired via HR, the entire *eGFP* sequence will be reconstituted, and cells will become green. If the cells undergo NHEJ to repair the induced DSB, *eGFP* will be out of frame, the *mCherry* sequence will be in frame, and the cells will become red. The figure was adapted from [157]. **B** Flow cytometry gating strategy to analyze only the cells that have been successfully transduced, indicated by expression of *BFP*. **C** Flow cytometry analysis of OC12 R#1 and S#1 TLR-*Sce* cells 72h after

transduction with the I-SCE + donor lentiviral construct with indicated MOIs. Numbers shown inside the plots indicate percentages of live *BFP-positive* cells. **D** Quantification on data from (C), bar plots represent the percentage of GFP positive cells indicating HR-directed repair of induced DSB. **E** Quantification on data from (C), bar plots represent the percentage of *mCherry* positive cells indicating DSB repair via NHEJ.

In summary, both OC12 and OC14 resistant and sensitive cells demonstrated HR repair of DSBs. This was proven by several DNA repair assays (γH2A.X and RAD51 staining, Comet assay, Western Blot analysis, and traffic light reporter assay), in which resistant and sensitive cell lines showed similar responses to induced DNA damage. Moreover, DNA damage was induced by different approaches, such as chemotherapy and IR. Overall, the olaparib resistance in OC12 and OC14 cells was not driven by an improvement in DNA repair in the resistant cell lines compared to the sensitive ones. These data suggest that the resistant cells are more likely to be specifically resistant to PARPi and not DNA-damaging agents, such as MMS, Oxaliplatin, and IR.

4.13 Combination treatments as a strategy to treat cells with acquired olaparib resistance

As previously described in 1.4, PARP1 utilizes NAD+, cleaving it into nicotinamide (NAM) and ADP-ribose, that are attached to target proteins as poly- or mono-ADP-ribose chains. These PAR chains can be enzymatically broken down by PARG into NAM. NAM is mostly recycled into NAD+ by the NAD+ salvage pathway via the nicotinamide phosphoribosyl transferase (NAMPT) and other enzymes (Figure 30 A). As described earlier, PARPi acts by mimicking NAD+ and compete with NAD+ for the catalytic domain of PARP1, thereby preventing synthesis of PAR chains and trapping PARP1 onto the DNA. A recent study demonstrated that combining a NAMPT inhibitor, daporinad, with olaparib could sensitize olaparib-resistant cells again to the treatment [158].

Noticing a shift in metabolic pathways, particularly in all three olaparib-resistant OC12 cells, I hypothesized that this would have an impact on NAD+ levels in the resistant cells. To explore this, I measured the intracellular NAD+ levels in both OC12 and OC14 cells with and without olaparib treatment, utilizing the NAD/NADH Glo™ from Promega. In short, the NAD/NADH glo reagent contains the NAD cycling enzyme, which converts NAD+ to NADH. In the presence of NADH, the enzyme reductase reduces a pro-luciferin substrate to form luciferin, which can be measured with a luminometer.

For the OC12 resistant (R#1) and sensitive (S#1) cell lines I could not observe any difference in the NAD+ levels without olaparib treatment (Figure 30 B). This suggests that the metabolic changes between resistant and sensitive cells did not impact the NAD+ levels. Interestingly, when I treated the cells for 24 h with 10 μM olaparib, the NAD+ levels in the resistant (R#1) cells were significantly reduced compared to the control condition ($p = 0.01$), while they were not significantly reduced in the sensitive (S#1) cells.

In contrast in OC14 resistant (R#1) and sensitive (S#1) cells, the NAD+ levels were similar in the untreated condition and remained unchanged when I treated the cells with 10 μM olaparib for 24 h (Figure 30 C). These results might suggest that, at least in the OC12 resistant (R#1) cells, NAD+ is utilized under the induction of DNA damage by PARPi, this might be also in line with the previous finding that OC12 R cells switched their metabolic phenotype (see 4.11). This observation could indicate that PARP1 remains active in the resistant OC12 cells compared to the sensitive ones.

As NAD+ was consumed under olaparib treatment in olaparib-resistant OC12 cells, I next investigated whether the resistant OC12 cells could be rendered sensitive to olaparib treatment using the NAMPT inhibitor daporinad, which blocks NAD+ synthesis via the salvage pathway. First, to observe the impact of daporinad alone on cell viability in resistant and sensitive OC12 cells, I performed a CFA. I exposed the cells to different daporinad concentrations ranging from 0.01 nM to 100 nM for four consecutive days, followed by a two-day drug holiday. At low concentrations (0.01 – 0.1 nM), daporinad minimally affected cell viability in both resistant and sensitive OC12 cells (Figure 30 D, E). However, at higher concentrations (> 1 nM), a strong decrease in cell viability occurred, with 50 % or more of the cells dying, and at 100 nM daporinad, all cells (both resistant and sensitive) were dead (Figure 30 D, E). Notably, there was no significant difference in cell viability at each daporinad concentration among the three sensitive and three resistant OC12 cell lines (Figure 30 D, E).

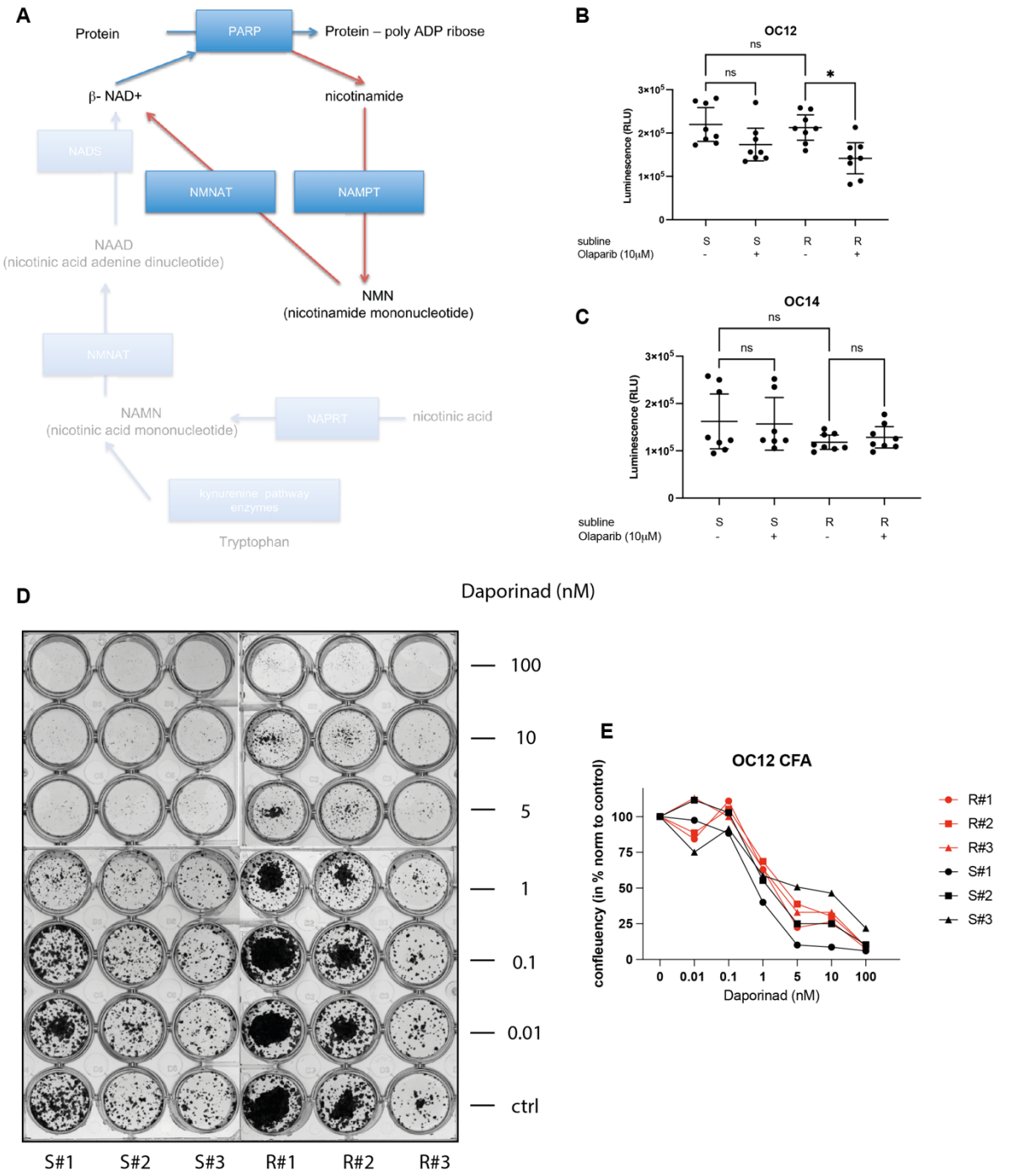

Figure 30 Inhibition of the Nicotinamide phosphoribosyl transferase (NAMPT) by daporinad alone has no diverse effect between resistant and sensitive OC12 cells.

A Schematic overview of NAD metabolism in human cells. Metabolites are represented in plain text, and enzymes are depicted in blue boxes. Enzyme abbreviations are as follows: PARP (poly(ADP-ribose) polymerase), NAMPT (nicotinamide phosphoribosyl transferase), NMNAT (nicotinamide mononucleotide adenylyl transferase), NAPRT (nicotinic acid phosphoribosyl transferase), NADS (NAD synthase). PARP reactions require β-NAD+ as a substrate and generate nicotinamide as a by-product of the PARylation of proteins. In cells with highly active PARPs, β-NAD+ is primarily supplied through a salvage pathway utilizing nicotinamide. Nicotinamide is converted back to β-NAD+ by two enzymes, NAMPT and NMNAT, with NAMPT catalysis representing the rate-limiting step in this process. Shown in half transparency: Alternatively, β-NAD+ can be synthesized de novo from either nutritional tryptophan (via the kynurenine pathway) or via nicotinic acid (NA), which is processed by NAPRT, NMNAT, and NADS. The figure was adapted from [159]. **B** NAD+ levels based on relative Luminescence signal in OC12 R#1 and S#1 cells treated with 10 μM olaparib or DMASO as control for 24h. The graph displays the result from 3 experiments with 3 replicates/cell line. **C** NAD+ levels based on relative Luminescence signal in OC14 R#1 and S#1 cells treated with 10 μM olaparib or DMASO as control for 24h. **G** The graph displays the result from 3 experiments with 3 replicates/cell line. P-values were calculated for three independent experiments using a one-way ANOVA test; * $p < 0.05$; ns, insignificant. **D** CFA for resistant and sensitive OC12 cells, treated for four days with indicated concentrations of daporinad,

followed by a 2-day drug holiday. Afterwards cells were fixed in 4 % PFA and stained with CV. **E** Quantification of cell confluency from D. The confluency was normalized to the confluency of the corresponding control well.

To assess the combined effect of olaparib and daporinad, I performed a CFA. The cells were exposed to various olaparib concentrations ranging from 0.25 µM to 20 µM, both with and without 0.2 nM daporinad. Treatment was applied for four consecutive days, followed by a two-day drug holiday (Figure 31 A). Consistent with previous observations, resistant OC12 cells demonstrated the ability to cope with higher concentrations of olaparib compared to sensitive cells (Figure 31 A, B and Table 19). In the co-treatment setting, both sensitive and resistant cell lines showed increased sensitivity to the treatment, indicated by reduced IC_{50} values (Figure 31 A, C and Table 19). The reduction in the IC_{50} values between olaparib alone and olaparib + daporinad treatment ranged from 20 to 100 times in the sensitive cells and 2 to 5 times in the resistant cells (Figure 31 D, E and Table 19).

Table 19 IC_{50} values of resistant and sensitive OC12 cells based on the CFA from Figure 31 A.

Cell lines	treatment	IC_{50} (µM)
OC12 S#1	olaparib	0.1
OC12 S#2	olaparib	0.3
OC12 S#3	olaparib	0.4
OC12 S#1	olaparib + daporinad	0.001
OC12 S#2	olaparib + daporinad	0.001
OC12 S#3	olaparib + daporinad	0.02
OC12 R#1	olaparib	9.5
OC12 R#2	olaparib	8.6
OC12 R#3	olaparib	3.8
OC12 R#1	olaparib + daporinad	2.8
OC12 R#2	olaparib + daporinad	1.6
OC12 R#3	olaparib + daporinad	2.3

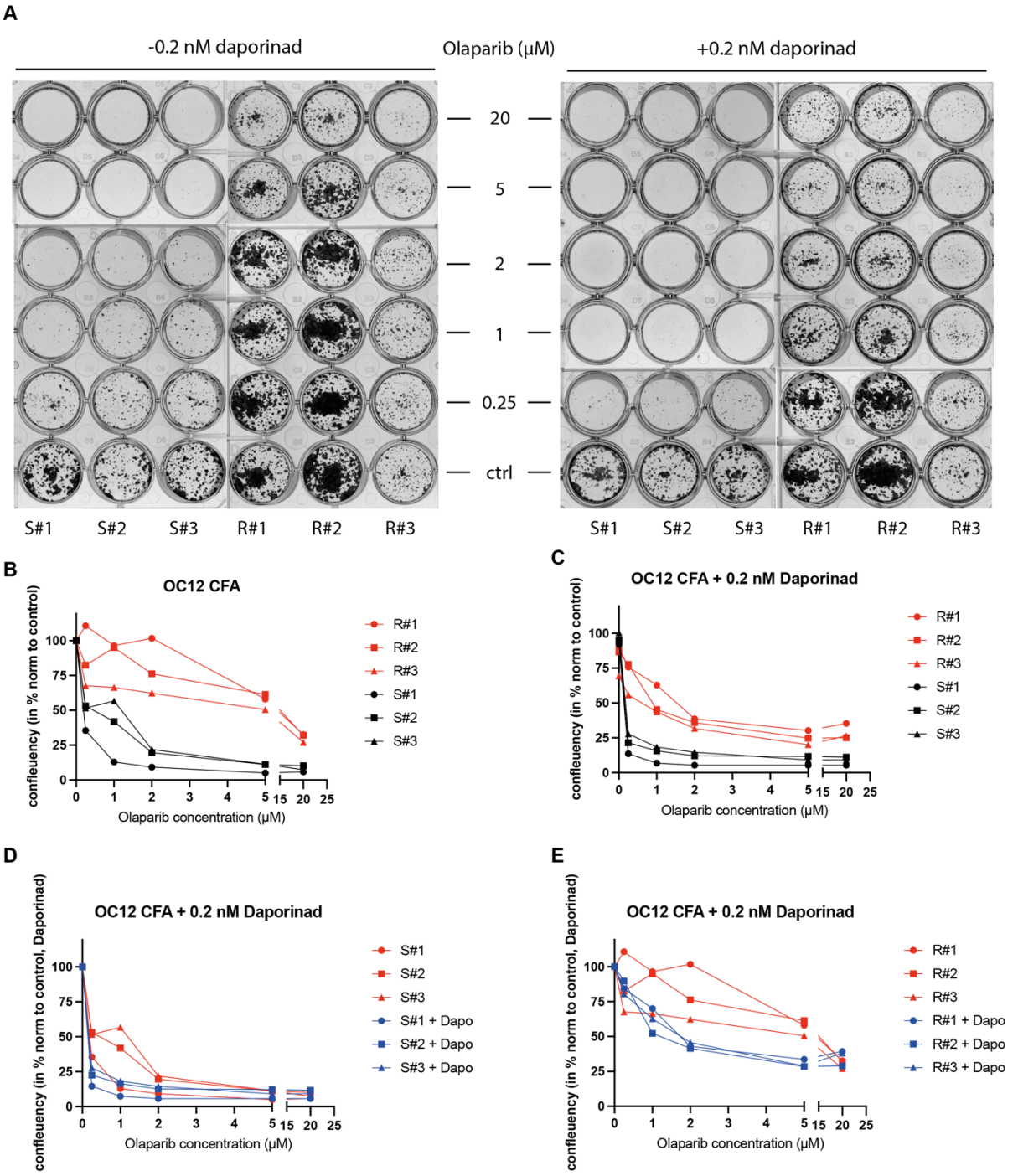

Figure 31 Inhibition of the Nicotinamide phosphoribosyl transferase (NAMPT) by daporinad sensitizes cells in general to olaparib treatment.

A CFA for resistant and sensitive OC12 cells, treated for four days with indicated concentrations of olaparib only (left CFA) and different olaparib concentrations plus 0.2 nM daporinad (right CFA), followed by a 2-day drug holiday. Afterwards cells were fixed in 4 % PFA and stained with CV. **B** Quantification of cell confluency from A (olaparib only). The confluency was normalized to the confluency of the corresponding control well. **C** Quantification of cell confluency from A (olaparib + 0.2 nM daporinad). The confluency was normalized to the confluency of the corresponding control well without any drug. **D** Quantification of cell confluency form the three sensitive OC12 cell lines treated with olaparib +/- 0.02 nM daporinad. The confluency was normalized to the confluency of the corresponding control well, in case of the daporinad treated cell confluency was normalized to the control well without olaparib + 0.2 nM daporinad. **E** Quantification of cell confluency form the three resistant OC12 cell lines treated with olaparib +/- 0.02 nM daporinad. The confluency was normalized to the confluency of the corresponding control well, in case of the daporinad treated cell confluency was normalized to the control well without olaparib + 0.2 nM daporinad.

These data suggest that daporinad can enhance the sensitivity of cells to PARP inhibitor treatment. Notably, the impact is not specific to olaparib-resistant cells, as the reduction in IC_{50} values was more pronounced in the sensitive cell lines.

In addition to the co-treatment of olaparib and daporinad, I also tested several other combination treatments. These included olaparib with ATM inhibitor [160], ATR inhibitor [64, 65] and PI3K/mTOR inhibitor [161], all of which are currently in clinical trials. To validate whether the combination treatments have a synergistic effect on the cell lines (OC12 and OC14 R#1, S#1), I performed cross titrations for 72 h. The two drugs were tested at multiple different concentrations. Afterwards, the cell viability for each combination was normalized, and the zero-interaction potency (ZIP) score model with baseline correction was calculated utilizing SynergyFinder [162].

I did not detect an overall synergistic effect for the combination of olaparib and the PI3K/mTOR inhibitor (dactolisib) in OC12 and OC14 resistant (R#1) and sensitive (S#1) cells (suppl. Figure 9). The same was true for the combination of olaparib and the ATM inhibitor (KU60019) (suppl. Figure 10), as well as for the combination of olaparib and the ATR inhibitor (Ceralasertib) (suppl. Figure 11).

5. Discussion

In this study, I induced resistance to PARPis in previously sensitive patient-derived ovarian cancer cell lines by administering increasing concentrations of olaparib over multiple treatment rounds. Subsequently, I initiated the characterization of these olaparib-resistant cell lines based on molecular features, including gene expression analysis, cell viability, colony-forming assays, cell proliferation, and apoptosis assays. Leveraging these phenotypic characteristics, I aimed to elucidate the underlying mechanism behind the acquired olaparib resistance. This involved inhibition and CRISPR Cas9-based knockouts of potential targets and target genes, respectively, as well as co-treatments with other drugs to overcome or re-sensitize resistant cells to PARPi treatment.

Despite these efforts, the key mechanism of olaparib resistance in the two studied cell lines (OC12 and OC14) remained elusive. Yet, the acquired data enabled me to illustrate that even HR-proficient cell lines can exhibit sensitivity to PARPi treatment. Moreover, I uncovered that the resistance mechanism in HR-proficient cells appeared disconnected from DNA damage response. The olaparib-resistant cell lines demonstrated a broad resistance to PARPi, suggesting that acquired resistance in HR-proficient cells may not be due to a “classical” resistance mechanism to a single PARPi but rather induced by metabolic or epigenetic alterations prompted by the treatment.

5.1 Inducing PARPi resistance in patient-derived ovarian cancer cell lines

Most studies investigating PARPi resistance in ovarian cancer typically employ commercially available cell lines with predetermined genetic characteristics or induced knockouts (KOs), such as BRCA1, to achieve HRD cells [76, 89, 94, 95, 107, 163, 164]. Additionally, many of these cell lines are cultured in media supplemented with Fetal Calf Serum (FCS), known for its considerable variability in growth factor composition between batches and its potential undesired effects on cells [165]. Prolonged cultivation of cells in FCS-supplemented media has been associated with the acquisition of genomic and phenotypic alterations [166, 167]. Moreover, the heterogeneity in the primary patient sample tends to diminish during the culturing process with an FCS-containing medium due to clonal selection [168]. To mitigate the potential impact of FCS on patient-derived cell lines, I cultured the cell lines in the

laboratory using a defined serum-free medium. This approach aimed to preserve the heterogeneity observed in the primary patient sample, even during prolonged cultures.

Several studies have applied whole-genome or targeted-CRISPR screens to pinpoint new targets inducing resistance to PARPi treatment [94, 95, 108, 122, 146]. Nevertheless, a notable observation is that many of these identified mechanisms are not commonly observed in clinical settings. Only a minority of these mechanisms have been successfully validated in clinical contexts, such as the re-mutation of mutant *BRCA1* and the reintroduction of an open reading frame [78, 82, 164]. In addition to carefully selecting cell lines and considering culture conditions, I subjected the sensitive patient-derived cell lines to long-term treatment with olaparib to induce resistance and to subsequently study the emergence and generation of PARPi resistance in a more realistic setting.

In the two key publications from 2005, the effect of PARP1 inhibition was investigated in cells bearing mutations in *BRCA1* or *BRCA2* [53, 54]. Subsequently, the first clinical trials of olaparib focused on ovarian cancer patients with *BRCA1* or *BRCA2* mutations, ultimately leading to the approval of olaparib monotherapy for patients with inherited *BRCA1* or *BRCA2*-mutated ovarian cancer [169]. In the following years, it was established that patients lacking a BRCA mutation but carrying mutations in other HR genes (*ATM, ATR, BAP1, CDK12, CHK2, FANCA, FANCC, FANCD2, FANCE, FANCF, PALB2, NBN, WRN, RAD51, MRE11, CHK1, BLM, BRIP*) could also benefit from PARPi treatment [154]. This phenomenon was termed "*BRCAness*" as these mutations mimic defects in one of the BRCA genes [170, 171]. Such discoveries facilitated the expansion of ovarian cancer treatment to include patients with deficiencies in HR repair, which are 50 % of all ovarian cancer patients [154, 172].

Surprisingly, when I characterized the eight patient-derived ovarian cancer cell lines previously established in our laboratory, I discovered that neither OC12 nor OC14 harbored a mutation in an HR gene (Figure 10). Unfortunately, it was impossible to call the HR deficiency status of the cell lines by the previously published pipeline that depends on a germline control [173, 174]. Instead, I validated the DNA repair potential of OC12 and OC14 through various experiments, confirming that both cell lines were proficient in HR (see 4.12).

Indeed, it has been demonstrated that epigenetic changes, such as promoter methylation, can induce HR deficiency, even in cells considered HR-proficient based on their mutational status [153, 175]. Additionally, certain genes unrelated to HR have been associated with conferring sensitivity to PARPis. Notable instances include translocations involving transmembrane protease serine 2 (TMPRSS2)-ERG in prostate cancer [176] and Ewing sarcoma-associated translocations associated with PARPi sensitivity [177]. Interestingly, mutations in *PTEN* leading to genomic instability have also been connected to PARPi sensitivity [178, 179]. However, the precise mechanism(s) behind the induction of a PARPi-sensitive phenotype remain elusive [154]. This discovery is particularly intriguing, considering the basal OC12 and OC14 cell lines exhibit genomic instability and chromosomal rearrangements according to M-FISH and WGS data (see 4.7). Whether genomic instability is why both cell lines were HR-proficient and simultaneously sensitive to PARPi – something typically considered mutually exclusive – warrants further investigation.

Exploring the mechanisms by which HR-proficient cells, such as OC12 and OC14, exhibit sensitivity to PARPi treatment holds considerable promise. Identifying these mechanisms or signatures could potentially pave the way for extending PARPi treatment to HR-proficient patients, which is a significant portion (50 %) of all ovarian cancer patients) [1]. This research avenue presents an exciting prospect for expanding the therapeutic benefits of PARPi beyond the currently recognized genetic markers, offering new avenues for precision medicine in ovarian cancer treatment.

By applying increasing concentrations of olaparib treatment in both cell lines, I induced resistance to the treatment, as evidenced by the remarkable up to 170-fold increase in the resistance score in OC12-resistant cells and a 118-fold increase in OC14-resistant cells (Figure 11). This compellingly demonstrates that the approach to simulate the clinical situation in the laboratory resulted in the acquisition of PARPi resistance in previously sensitive ovarian cancer cell lines. These findings are in contrast with a recent study led by Fedier *et al.* where they treated seven ovarian cancer cell lines with olaparib for 48 hours over two to eight cycles [180]. They did not observe the acquisition of olaparib resistance in all seven treated lines, as indicated by resistance scores below 2 in all seven cell lines after the treatment regimen [180]. The relatively short treatment period of 48 h and the lower number of treatment cycles, in

comparison to the treatment regimen employed in this thesis (96 hours of olaparib treatment for more than 10 cycles), might account for the disparate outcomes between their study and the findings presented in this thesis.

I demonstrated that OC12 and OC14 cell lines become resistant to olaparib and the stability of the acquired resistance over extended periods without ongoing olaparib treatment. Even though the resistance score reduced slightly compared to the time point immediately after the treatment regimen, the resistant cells maintained at least a 20-fold (OC12) and 9-fold (OC14) higher resistance than the sensitive cells. These findings contradict studies showing that resistance induced by various chemotherapeutic drugs can be transient. For instance, such transience can occur through the induction of the expression of ABCB1 drug efflux pumps in the presence of the drug [181] or the upregulation of epidermal growth factor receptor (EGFR) in the presence of BRAF or MEK inhibitors in melanoma patients. This phenomenon is reversed upon discontinuation of the drug treatment [182]. However, this transient nature of drug resistance was not present in OC12 and OC14-resistant cells, in which the drug resistance was permanent over long periods without any drug exposure.

5.2 Cross-resistance to other PARP inhibitors

The chemical structure of PARPis enables them to bind to the NAD binding pocket of PARP1, situated in the catalytic domain of PARP1, competing with NAD for binding [72, 183]. However, despite their similar capacity to inhibit the catalytic domain of PARP1, different PARPis exhibit variable levels of cytotoxicity [70, 71]. The primary distinction among PARPis lies in their ability to trap PARP1 onto DNA, a property that is independent of their potency in inhibiting PARP catalytic activity [71]. Consequently, it was interesting to investigate whether ovarian cancer cells treated exclusively with one PARPi, in this case, olaparib, would develop cross-resistance to other PARPis with higher or lower trapping potencies than olaparib. Indeed, both OC12 and OC14-resistant cells demonstrated cross-resistance to talazoparib, characterized by the strongest trapping potential, and niraparib, which exhibits a higher trapping potential than olaparib. However, it is noteworthy that only OC12-resistant cells demonstrated cross-resistance to rucaparib, the weakest trapper among the four PARPis tested in this study.
Conversely, OC14-resistant cells exhibited comparable IC_{50} values to the sensitive cells when treated with rucaparib. This observation implies that the resistance mechanism in OC14 cells

may be specifically linked to PARPis, which traps PARP on the DNA. Furthermore, it suggests that these cells remain sensitive to PARPis, which primarily blocks the enzymatic activity of PARP1 without trapping the enzyme.

5.3 PARPi-resistant and sensitive cells are affected similarly by DNA-damaging agents

Given the mechanism of PARPis, trapping PARP onto the DNA leads to replication fork collapse and, ultimately, DSBs. An important question was whether PARPi-resistant cells also showed resistance to other DNA-damaging agents, including platinum salts, MMS, paclitaxel, and irradiation. Ovarian cancer patients typically undergo pre-treatment with platinum salts and show initial response to such treatment [184, 185]. In the case of OC12 and OC14, both patients were pre-treated with platinum compounds, OC12 with cisplatin, and OC14 with carboplatin (see. Table 2).

Upon treating the resistant and sensitive OC12 and OC14 cell lines with oxaliplatin, no discernible shift in the IC_{50} of the PARPi-resistant cells compared to the sensitive cells was observed. The concentrations of oxaliplatin used in the assays spanned from 0.01 µM to 500 µM, covering physiologically relevant concentrations, as the maximum plasma concentration in patients is approximately 3.6 µM [186]. This suggests that the acquired PARPi resistance did not confer additional resistance to platinum drugs. It is noteworthy, that oxaliplatin induces platinum-DNA adducts, including mono adducts, intrastrand, and interstrand cross-links [187-189]. NER typically repairs DNA damage induced by platinum salts, whereas PARPi-induced DNA damage is typically repaired by HR or end-joining pathways [130, 140, 190].

In addition to oxaliplatin, I evaluated the response to the DNA alkylating agent MMS. MMS induces modifications in both guanine (to 7-methylguanine) and adenine (to 3-methyladenine), resulting in base mispairing. These mispairings are predominantly repaired by the BER pathway [21]. Furthermore, it has been shown that MMS can also induce DSBs [191]. Upon treating OC12 and OC14 resistant and sensitive cells with MMS, no significant differences in the response to MMS treatment were observed between OC12 and OC14 resistant and sensitive cells (see Figure 15). These findings suggest that the acquired PARPi resistance mechanism does not affect MMS treatment.

The third compound I tested was Paclitaxel. Paclitaxel, a taxane, stabilizes microtubule and is a standard-of-care treatment for ovarian cancer patients, commonly used alongside platinum-based chemotherapy [192]. The patient from whom we obtained the OC14 cell line had received paclitaxel as part of the first-line chemotherapy. However, when treating both OC12 and OC14 resistant and sensitive cells with paclitaxel, no difference in response was observed between the resistant and sensitive cells. The paclitaxel concentration ranged from 0.001 nM to 100 nM, partially within the range of the peak plasma concentration of paclitaxel in humans (~11.7 µM, after 1 day ~23 nM)[193, 194].

Radiation was the final DNA-damaging agent I tested in this thesis, specifically in OC12-resistant and sensitive cells. Gamma rays are known to induce DNA breaks, particularly DSBs. Additionally, IR triggers the generation of reactive oxygen species and various forms of DNA damage, including SSBs and abasic sites [195]. By inducing multiple types of DNA damage through IR, I aimed to explore whether there is a differential response to DNA damage between PARPi-resistant and sensitive OC12 and OC14 cells. Consistent with the observations from previously discussed DNA damaging agents, there was no significant difference in response to IR between OC12 and OC14 resistant and sensitive cells, as assessed by comet assay, RAD51, and γH2A.X staining (see Figure 27, Figure 28).

In summary, the acquired resistance mechanism to PARPi in both OC12 and OC14 cell lines did not influence the response to DNA damage-inducing agents. Furthermore, these findings suggest that the resistance mechanism(s) in both cell lines do not impair the DNA repair capacity of the cells and are likely to be PARP-specific.

5.4 Exclusion of known PARPi resistance mechanisms

Since the approval of PARPi for the treatment of ovarian and breast cancer patients, there has been a significant focus on unraveling resistance mechanisms to PARPi therapy, a critical hurdle in achieving successful patient treatment [41, 196]. The most common and extensively studied resistance mechanism to PARPi treatment is secondary mutations in either *BRCA1* or *BRCA2*, reconstructing the open-reading frame of the gene and enabling the translation into a functional protein [80, 82, 84]. Secondary mutations in *BRCA1* or *BRCA2* have been documented in ovarian cancer patients in the clinic [77-84]. However, given that both OC12

and OC14 cells were wildtype for *BRCA1* and *BRCA2*, a secondary mutation can be ruled out as the underlying cause of the observed resistance to PARPis. Reversion mutations are not exclusive to *BRCA1/2* and have also been identified in other HR-related genes, such as *RAD51C/D* and *PALB2*, which would restore DNA repair via HR Consistent with the absence of secondary mutations in *BRCA1/2*, both cell lines were HR proficient and did not harbor mutations in any of the HR genes.

In addition to secondary mutations in mutant HR genes, the loss of NHEJ genes has been associated with PARPi resistance. The loss of *53BP1*, for instance, restores end resection in *BRCA1*-deficient cells, facilitating HR repair of DSBs and ultimately conferring resistance to PARPi treatment [89, 90]. Furthermore, the loss of other proteins involved in DNA end resection, such as the shielding complex [94], DYNLL1 [95, 197], and MRE11 [95], has been demonstrated to impart PARPi resistance both *in vitro* and *in vivo*.

In addition to restoring HR repair in PARPi-resistant cells, several identified mechanisms related to PARP1 or PARPi usage can contribute to acquiring PARPi resistance. The first proposed resistance mechanism involves the upregulation of the drug efflux transporter *ABCB1*, also known as P-glycoprotein [98]. Upregulation of *ABCB1* is a well-established source of resistance to various chemotherapies, preventing the intracellular accumulation of substances [100, 101]. Indeed, when I analyzed the DEGs between OC12-resistant and sensitive cells, both *ABCB1* and *ABCB4* were significantly upregulated in the resistant cell lines (Figure 17). I further validated this upregulation through qPCR and Western Blot analysis. Surprisingly, neither the pharmacological inhibition of ABCB1 with a potent ABCB1 inhibitor, Zosuquidar [102] nor the CRISPR-based KO of *ABCB1* plus *ABCB4* resulted in a significant change in the response to olaparib treatment in OC12 resistant cells. Furthermore, I tested Pamiparib, a PARPi published in 2020 that is not a substrate for ABCB1, in both OC12-resistant and sensitive cells [104, 198]. However, the OC12-resistant cells demonstrated resistance to olaparib and Pamiparib, indicating that the upregulation of *ABCB1* and *ABCB4* alone is not the main source of PARPi resistance in OC12-resistant cells (Figure 17 G).
In theory, a mutation in the PARP1 gene, which might either reduce the affinity to the PARPi or sustain the endogenous protein function when bound to the inhibitor, could also lead to

resistance to PARPis [107]. However, I did not identify any mutation in PARP1 based on WES and WGS in either OC14-resistant or OC12-resistant cells.

In summary, I have demonstrated that none of the known PARPi resistance mechanisms can account for the acquired PARPi resistance observed in both OC12 and OC14 cell lines. This suggests an unknown resistance mechanism that is likely independent of DNA repair pathways and may be specific to the function of PARP itself.

5.5 Validation of potential target genes did not reveal the source of PARPi resistance

Since I could not find a known PARPi resistance mechanism, I analyzed the DEGs between resistant and sensitive cells to identify potential target genes differentially expressed in the resistant cells and might be responsible for the acquired resistance to PARPis. Interestingly, in my analysis of DEGs between OC12-resistant and sensitive cells, I observed an upregulation of *APLF*. APLF is known to be phosphorylated at Ser116 by ATM upon DNA damage and is involved in the repair of DSBs. Two studies from 2011 and 2012 demonstrated that APLF interacts with PARP3 and accelerates DNA ligation during NHEJ [35, 199]. Consequently, I hypothesized that the upregulation of *APLF* in PARPi-resistant OC12 cells could enhance DNA repair via NHEJ, potentially contributing to resistance to PARPi treatment. Additionally, APLF has been implicated in conferring resistance to IR in glioblastoma patients [200]. However, CRISPR-induced APLF depletion did not significantly affect OC12-resistant cells in response to olaparib treatment (Figure 18 B).

Moreover, I observed an upregulation of transcription factor *TWIST1* in OC12-resistant cells. TWIST1 is typically required for early mesoderm development but is usually silenced in adult tissues [201]. In many cancer types, TWIST1 is reactivated and drives epithelial to mesenchymal transition (EMT), leading to tumor metastasis. Besides its role in cancer progression, the upregulation of *TWIST1* has been associated with cisplatin resistance in epithelial ovarian cancer by promoting the expression of *GAS8* and *L1CAM*, leading to AKT phosphorylation and increased cell proliferation [202]. However, the CRISPR-based KO of *TWIST* did not significantly affect the response of OC12-resistant cells to olaparib treatment (Figure 18 C).

5.6 Characteristics of olaparib-resistant OC12 and OC14 cell lines

I conducted experiments to elucidate the molecular differences between olaparib-resistant and sensitive OC12 and OC14 cells. Given that the resistant cell lines exhibited downregulation of cell cycle pathways compared to the sensitive cells, I hypothesized that the resistant cells could potentially have a slower cell cycle rate than the sensitive counterparts. This potential difference in cell cycle dynamics could contribute to resistance to PARPi treatment, as PARPis predominantly affect proliferating cells [203].

Furthermore, chemotherapy has been demonstrated to induce a senescent-like state, which can lead to resistance to treatment [204, 205]. Additionally, it has been shown that PARPis induce senescence in cancer cells [149, 150]. I performed cell proliferation assays under olaparib treatment to test this hypothesis in OC12 and OC14-resistant cells. However, contrary to expectations, the resistant cells did not enter a senescent-like state under treatment. Instead, the resistant cells proliferated similarly to the control cells (see 4.9). This observation was consistent with the finding that the resistant cells exhibited a significantly lower apoptosis rate under treatment compared to the sensitive cells, which showed an apoptosis rate of up to 80 % (Figure 22).

Furthermore, when I analyzed the cell cycle state of resistant and sensitive cells under olaparib treatment, I observed that most sensitive cells were stalled at the G2/M checkpoint. In contrast, the resistant cells could be found in every phase of the cell cycle (see 4.10). The G2/M checkpoint is a major checkpoint in the cell cycle, preventing cells with unrepaired DNA damage from entering the M-phase and passing along damaged DNA to the daughter cells [125]. A study by Inbar-Rozensal and colleagues suggests a possible mechanism underlying G2/M arrest induced by PARPi through signal transduction pathways involving cell cycle proteins, such as p21, cyclins, and cdc2 [206]. However, I could not detect any change in the expression levels of cell cycle proteins between resistant and sensitive cells, which would explain why the resistant cells are not stalled at the G2/M checkpoint.

Another notable difference between resistant and sensitive cells, observed in all three resistant OC12 and one resistant OC14 cell lines, was a shift in energy metabolism from glycolysis to oxidative phosphorylation (OXPHOS) (see 4.11). Otto Warburg proposed in the 1920s that cancer cells primarily rely on glycolysis to produce ATP, in contrast to healthy cells, which predominantly use mitochondrial OXPHOS to meet their ATP needs [207]. However,

Warburg's hypothesis has been challenged recently, with evidence showing that cancer cells can still utilize OXPHOS to generate ATP [208].
Interestingly, several studies have demonstrated that chemotherapy induces OXPHOS in cancer cells, which may contribute to resistance to treatment [209-212]. Targeting OXPHOS has been suggested as a potential strategy to eliminate chemotherapy-resistant cancer cells. However, when I tried to treat the cells with the ATP synthase inhibitor Oligomycin, the treatment proved to be excessively toxic for both sensitive and resistant cells (data not shown), making it challenging to draw a clear conclusion about the impact of inhibiting OXPHOS. Since healthy cells predominantly rely on OXPHOS for their energy supply, treatment with OXPHOS inhibitors will be a huge hurdle in finding a tolerable dose for patients [213].

As the primary substrate of PARP enzymes is NAD+, I aimed to investigate whether differences in the availability of NAD+ could be detected in resistant compared to sensitive cells. Several studies have demonstrated that upon DNA damage and PARP1 activation, up to 90 % of the NAD+ pool is rapidly depleted within minutes by PARP1 activity. The NAD+ pool can be refueled by either de novo synthesis from the essential amino acid tryptophan or via the salvage pathway. However, the de novo pathway only contributes to a small fraction of the total NAD+ pool [214]. The primary source of NAD+ is through the salvage pathway, driven by the enzyme nicotinamide phosphoribosyltransferase (NAMPT). NAMPT converts nicotinamide to nicotinamide mononucleotide, which is then enzymatically converted to NAD+ in the final step of the pathway [215, 216].
Therefore, I analyzed NAD+ concentrations in resistant and sensitive OC12 and OC14 cells with and without olaparib treatment. Interestingly, the NAD+ concentrations significantly dropped in the resistant OC12 cells (see Figure 30). This finding might indicate that PARP1 is still active in the resistant cells and consumes NAD+ in the presence of olaparib [217, 218]. To further validate this finding, I aimed to deplete intracellular NAD+ from the cells and observe the effect of NAD+ depletion on the resistant cells.

Indeed, Daporinad (FK866, APO866), an inhibitor for NAMPT has been available since 2009, blocking the synthesis of NAD+ via the salvage pathway [219]. Co-treatment with daporinad and olaparib has demonstrated synthetic lethality in triple-negative breast cancer cells [159]. Even more interesting, the co-treatment of olaparib and daporinad induced synergistic effects in PARPi-resistant ovarian cancer cells and xenograft models, overcoming resistance to PARPi treatment [158].

Hence, it was interesting to investigate the effect of olaparib and daporinad co-treatment in resistant cells. A combination treatment of olaparib and daporinad (0.2 nM daporinad + 0.25, 1, 2, 5, 20 µM olaparib) the resistant cells reduced the IC_{50} value two to five times. However, this effect was even more prominent in the sensitive cells (20 to 100 times reduction in IC_{50}, see Figure 31). It is also worth mentioning that the IC_{50} value for daporinad alone, around ~2 nM, was already very low. This raises the question of whether a co-treatment of olaparib and daporinad is feasible in the clinic given the high cytotoxicity of daporinad alone (see Figure 30). Furthermore, I could not investigate the effects of daporinad alone and in combination with olaparib on healthy cells, leaving the question of daporinad's impact on normal cell viability unanswered.

Together, I have demonstrated that PARPi-resistant cells do not enter a senescent state under drug pressure. On the contrary, these resistant cells exhibit continued proliferation, while sensitive cells are arrested at the G2M checkpoint of the cell cycle, eventually undergoing apoptosis. Moreover, all three PARPi-resistant OC12 cells and one resistant OC14 cell line shifted their energy metabolism from glycolysis to OXPHOS. Additionally, under olaparib treatment, the resistant OC12 cells showed a significant reduction in intracellular NAD+ levels, suggesting ongoing PARP activity. However, inhibiting NAD+ synthesis through the salvage pathway affected resistant and sensitive cells. Nonetheless, the combination treatment appears to be a promising approach to enhance the efficacy of PARPis.

5.7 The molecular function of PARP1 in cells

Beyond their role in DNA repair, PARP enzymes are involved in various cellular processes such as transcriptional regulation, mitochondrial function, formation of subnuclear bodies, RNA interference, and cell division [33, 40, 217, 218]. For instance, PARP1 has been shown to regulate the activity of several TFs by recruiting co-regulators, which stimulates, in turn, the transcriptional activity of target genes [220]. Furthermore, PARP1 has been shown to localize to promoters of actively transcribed genes and delimitate the binding of histone H1 to DNA, promoting an open chromatin that supports transcription [221]. In addition to their role in transcriptional regulation, multiple PARP enzymes are associated with PAR-dependent protein ubiquitylation, resulting in proteolysis of target proteins [222]. Moreover, it has been shown that PARP1 can stimulate cell survival pathways such as NF_kB- and Wnt- signaling, which could contribute to resistance to cell death-inducing agents [223, 224]. Last but not least, it has been shown that several PARP enzymes are involved in the formation of RNA-rich cytoplasmic stress granules, which form under heat shock or other stress conditions [225].

Based on the multifaceted role in molecular pathways of the cell, the acquired PARPi resistance mechanisms, which I have observed in both OC12 and OC14 cell lines, are independent of PARP1's function in DNA repair but might be related to one of its other roles. Furthermore, it cannot be ruled out that the resistance is due to the inhibition of other PARP enzymes, which can cleave NAD+ into ADP ribose and nicotinamide (PARP1, 2, 3, 4, 5, 6, 10, 14, 15, 16) [33]. This this hypothesis is supported by the finding that the PARPi niraparib has shown clinical benefits in patients lacking *BRCA1/2* mutations or any HR deficiency [169, 226, 227].

5.8 Limitations of this study

As I mentioned in section 1.1, it was impossible to apply an HR deficiency score for the cell lines used in this study due to the lack of germline control, which is needed as a control input for such scores. This led in the beginning of this study to the opinion that OC12 and OC14 cell lines are HR-deficient, based on their sensitivity to olaparib treatment. During my PhD, I discovered that both cell lines are HR proficient, based on sequencing data, DNA repair assays, and Western blot analysis. If I had had this information at the beginning of my thesis, the question would have been: "Why are HR proficient cells capable of PARPi treatment?", which

is an important question also for the treatment of HR proficient patients in the clinic that might benefit from PARPi treatment, as already shown in some studies [169, 226-228].
Moreover, the gene expression analysis based on RNA-seq was performed in the three resistant and sensitive cell lines of OC12 and OC14. This allows to observe significant changes which are present in all three resistant or sensitive cell lines, however changes in the individual cell lines are not hidden by the lack of technical replicates and statistical power. As observed for the resistant OC14 cells, they clustered apart from each other in the PCA, indicating that they are different based on their transcriptional phenotype (see Figure 19).
In addition, or as a replacement for gene-expression analysis, the proteome analysis by proteomics or phosphoproteomics might give a deeper insight into which proteins or pathways are affected in the resistant compared to the sensitive cells.

5.9 Future outlook

Even though I was able to exclude several known resistance mechanisms to PARPi treatment, the question remains: what drives the resistance in OC12 and OC14 cell lines? One possible explanation could be that the resistant cells metabolize PARPi, and the drug becomes inactivated when it enters the cell. A protein family that is known for its drug metabolism is the cytochrome P450 family [229]. One of these family members is CYP3A5, which has been demonstrated to drive paclitaxel resistance in pancreatic cancer by metabolizing the drug [230]. It is also known that PARPis are metabolized by CYP family members [231]. Theoretically, it would be possible that PARPis are inactivated by CYP family members, inducing resistance to the treatment. Therefore, in collaboration with the Department of Clinical Pharmacology at the University Clinic of Heidelberg, we are investigating the intra-cellular concentration of active olaparib in resistant and sensitive cells. In addition, this approach would also answer the question of drug concentrations in the cells. Another explanation of PARPi resistance is the upregulation of drug efflux pumps (discussed in 1.6.2 and 5.4
). It might be possible that PARPis are substrates of other efflux pumps rather than ABCB1.
Furthermore, in 2022, a PARP1-specific inhibitor was published by Feld *et al.* [112], which would exclude any off-target effects on other PARP enzymes; as discussed earlier, the resistance of the cells might be induced by other PARP family member functions. However, I

have not tested this PARP1-specific inhibitor so far, but it would be interesting to see whether the cells are also resistant to this PARP1-specific inhibitor.
A recently published study investigated drug resistance in patient-derived colorectal cancer organoid lines. They demonstrated that most resistance mechanisms are not explained by genetic changes alone. Indeed, they could show that epigenetic changes accounted for the resistance to the treatment, and they could not detect any mutation, which could explain the resistance [232]. As I could not detect a genetic alteration, which would explain the acquired PARPi resistance in both OC12 and OC14 cell lines, epigenetic analysis of resistant cells would be a promising approach to detect potential targets, which could account for the observed resistance.

The most favorable scenario to investigate PARPi resistance in patients would be to study patients receiving PARPis as first-line therapy; this would exclude any bias from other chemotherapies, such as platinum- or taxol-based therapy. Furthermore, it would be desirable to receive longitudinal patient samples before the beginning of treatment and at the time of acquired tumor resistance. These matched samples would be suitable for a variety of analyses and would offer a significant chance to detect and investigate clinically relevant resistance mechanisms to PARPi treatment.

The finding that HR-proficient cells show sensitivity to PARPi treatment can broaden the treatment spectra of PARPi additionally to HR-proficient patients. In the future, it has to be shown whether these findings in this thesis are valid in other HR-proficient ovarian cancer cell lines. If so, the question would be if there are potential biomarkers to detect HR-proficient patients who will benefit from PARPi treatment.

6. Appendix

6.1 Supplementary figures

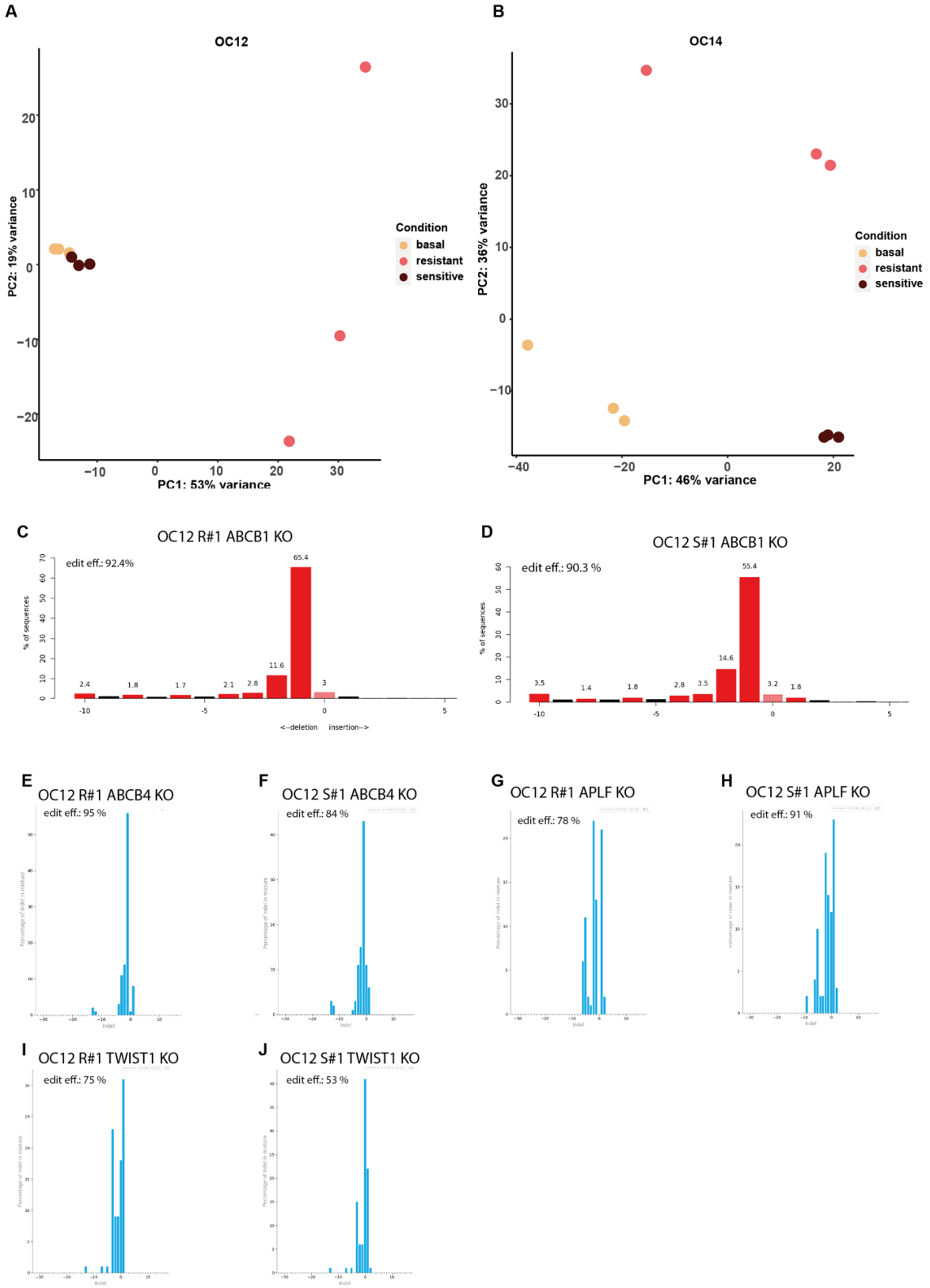

suppl. Figure 1 Principal component analysis (PCA)after treatment regimen and KO efficacy of *ABCB1* and *ABCB4* KO.
A PCA plot based on RNA-seq after treatment regimen of three replicates of basal, resistant and sensitive OC12 cell lines. **B** PCA plot based on RNA-seq after treatment regimen of three replicates of basal, resistant and sensitive OC14 cell lines. **C** ABCB1 KO efficiency in OC12 R#1 cells, based on sanger sequencing. **D** ABCB1 KO efficiency in OC12 S#1 cells, based on sanger sequencing. **E** ABCB4 KO efficiency in OC12 R#1 cells, based on sanger sequencing. **F** ABCB4 KO efficiency in OC12 S#1 cells, based on sanger sequencing. **G** APLF KO efficiency in OC12 R#1 cells, based on sanger sequencing. **H** APLF KO efficiency in OC12 S#1 cells, based on sanger sequencing. **I** TWIST1 KO efficiency in OC12 R#1 cells, based on sanger sequencing. **J** TWIST1 KO efficiency in OC12 S#1 cells, based on sanger sequencing.

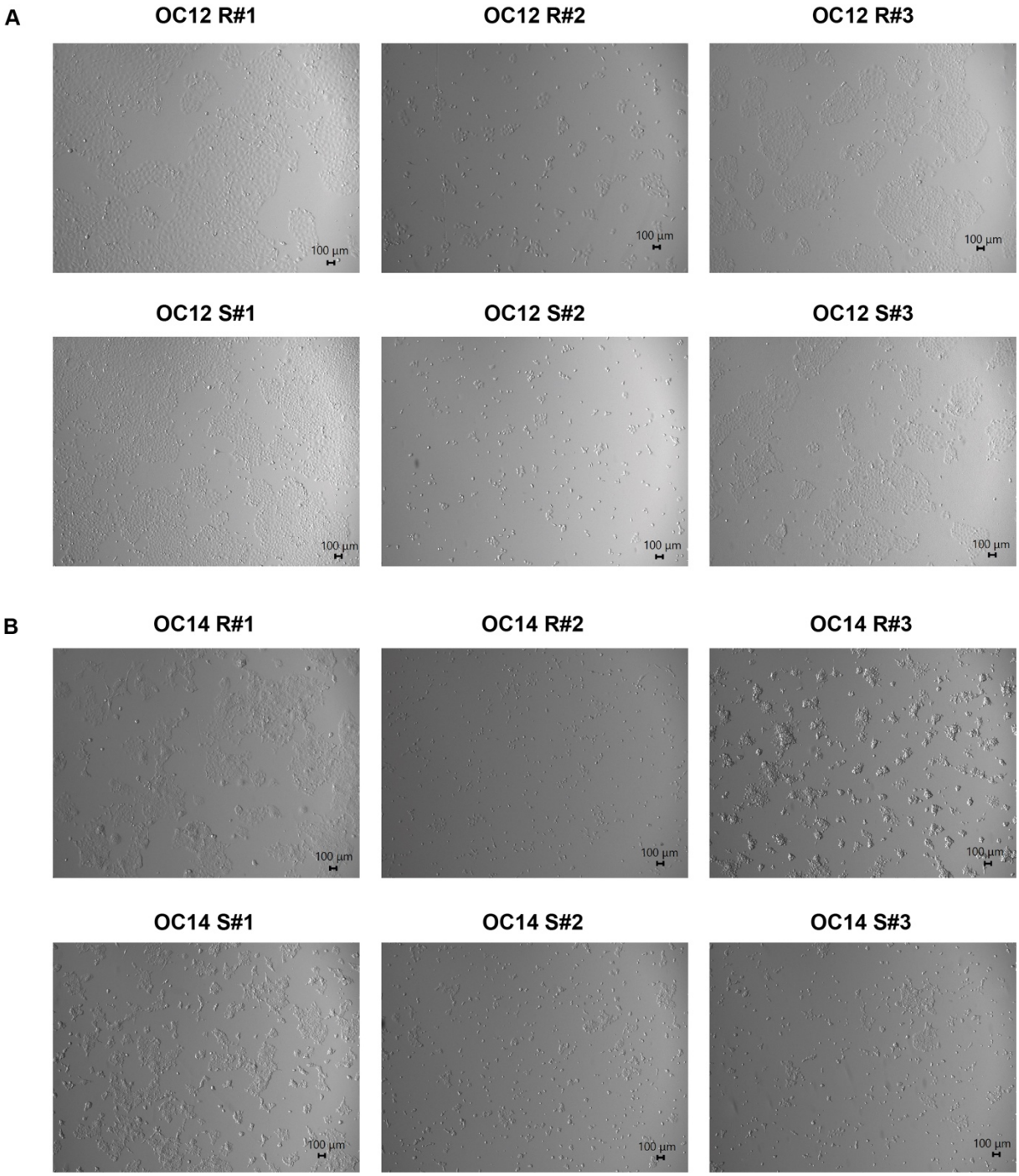

suppl. Figure 2 brightfield microscopy images of OC12 and OC14 cell lines.
A Representative brightfield microscopy images of OC12 R#1, R#2, R#3, S#1, S#2, S#3, cultured in CSC medium without treatment. **B** Representative brightfield microscopy images of OC14 R#1, R#2, R#3, S#1, S#2, S#3, cultured in CSC medium without treatment. Scale bar = 100 µm.

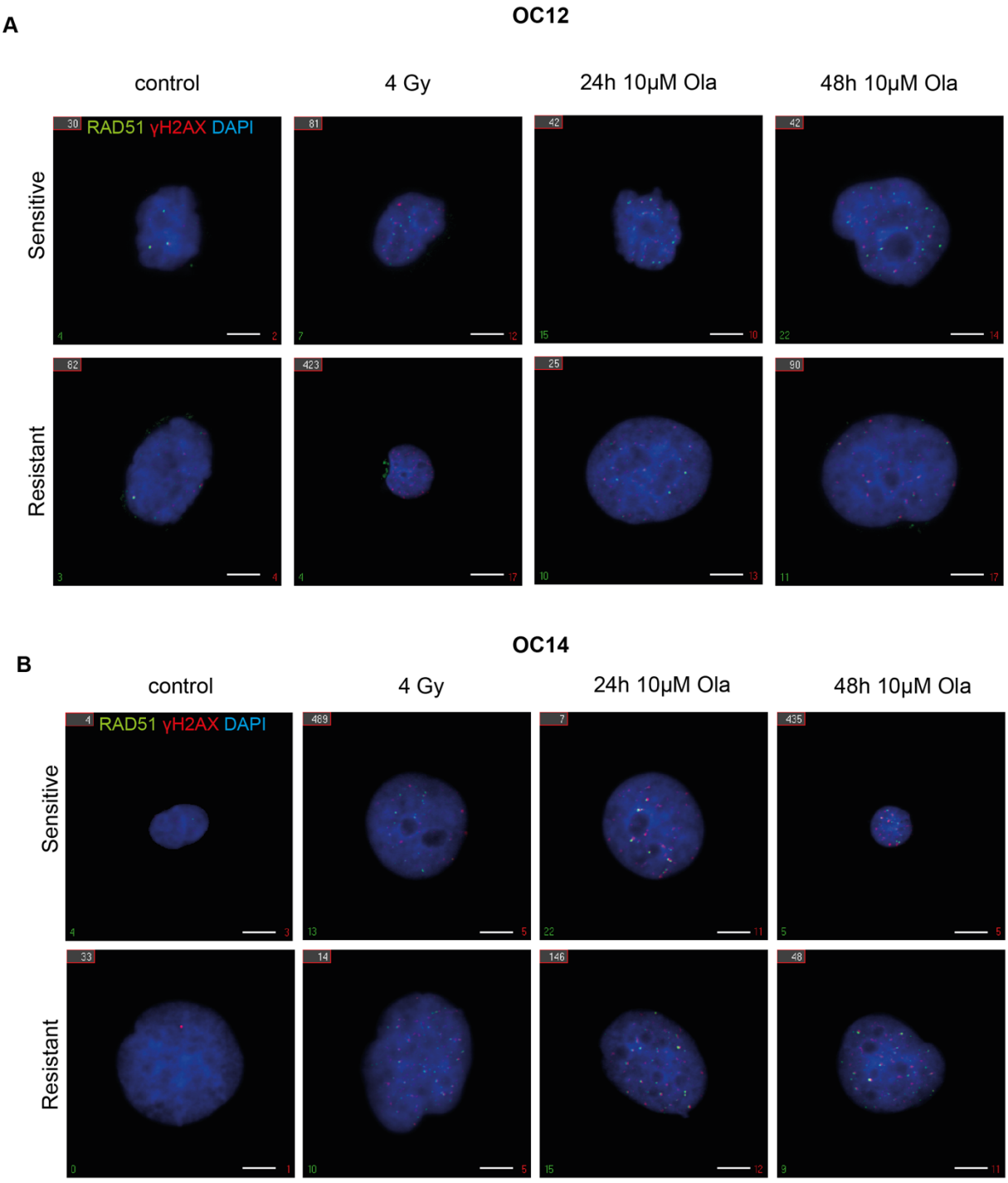

suppl. Figure 3 unmodified IF pictures of γH2AX and RAD51 foci staining.
A Representative images of OC12 R#1 and S#1 cells stained for Rad51- and γH2AX foci. Cells were either untreated, irradiated with 4 Gy, or treated with 10 µM olaparib for 24 or 48 h. Cells were fixed in 4 % PFA and stained as outlined in the methods section 3.15. **B** Representative images of OC14 R#1 and S#1 cells stained for Rad51- and γH2AX foci. Cells were either untreated, irradiated with 4 Gy or treated with 10 µM olaparib for 24 or 48 h. Cells were fixed in 4 % PFA and stained as outlined in the methods section 3.15. Scale bar = 10 µM.

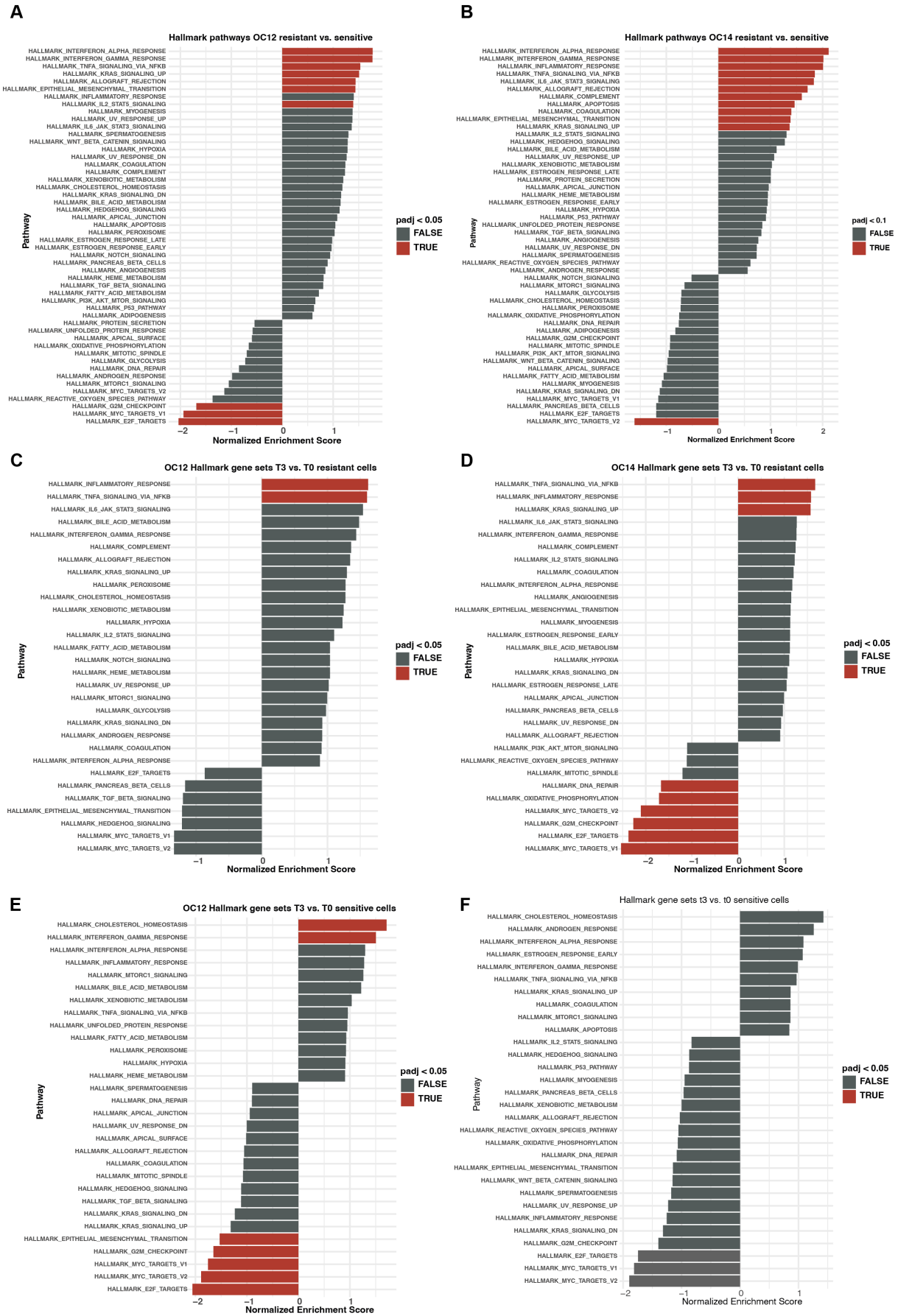

suppl. Figure 4 PARPi resistant and sensitive cells did not exhibit altered RNA expression over various time points during treatment, and the pathways are already present in the steady state without any treatment.

A GSEA on DEG between OC12 R (n=3) and S (n = 3) cells without olaparib treatment after the treatment regimen; displayed are the top 30 Hallmark gene sets. **B** GSEA was performed on DEG between OC14 R (n=3) and S (n = 3) cells without olaparib

treatment after the treatment regimen; the top 30 Hallmark gene sets are shown here. **C** GSEA was performed on DEG between OC12 R cells between T0 and T3 under olaparib treatment; the top 30 Hallmark gene sets are shown **D**. GSEA was performed on DEG between OC14 R cells between T0 and T3 under olaparib treatment; the top 30 Hallmark gene sets are shown **E**. GSEA was performed on DEG between OC12 S cells between T0 and T3 under olaparib treatment; the top 30 Hallmark gene sets are shown**. F** GSEA was performed on DEG between OC14 S cells between T0 and T3 under olaparib treatment; the top 30 Hallmark gene sets are shown. Statistical significance was assessed using 10,000 permutations on the phenotype. DEGs were pre-ranked based on their adjusted p-value.

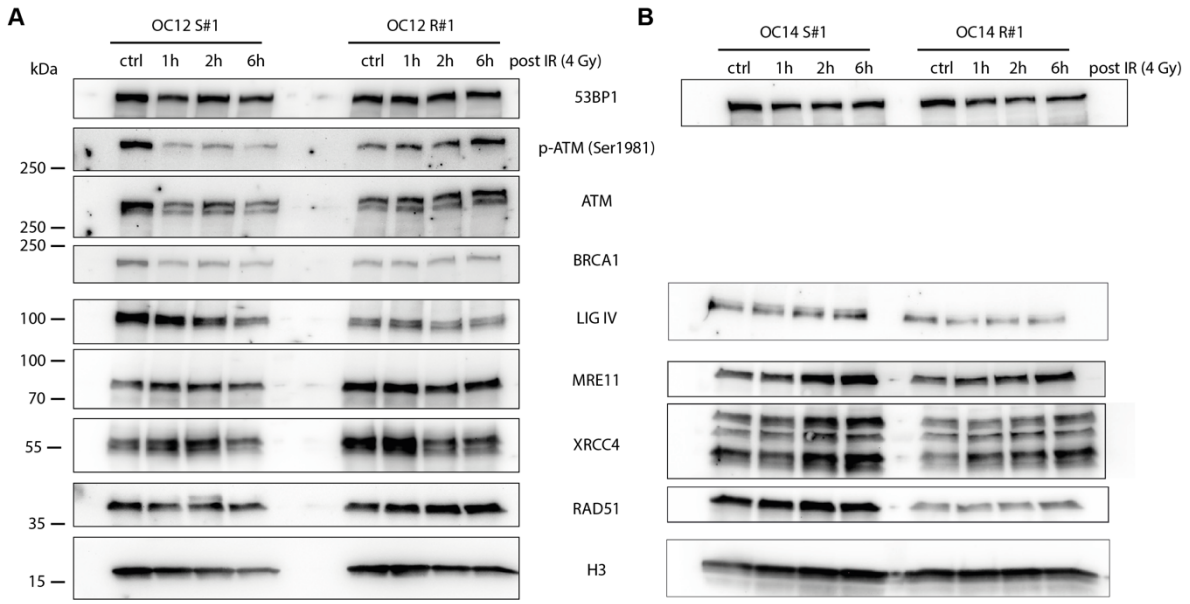

suppl. Figure 5 DNA repair kinetics upon IR in olaparib resistant and sensitive OC12 and OC14 cell lines.
A protein levels of chromatin bound proteins based on western blot analysis in OC12 S#1 and R#1 cells. The cells were treated with IR (4 Gy) and chromatin-bound protein was collected after 1,2 and 6 h post IR. Histone H3 was used as loading control. **B** protein levels of chromatin bound proteins based on western blot analysis in OC14 S#1 and R#1 cells. The cells were treated with IR (4 Gy) and chromatin-bound protein was collected after 1,2 and 6 h post IR. Histone H3 was used as loading control.

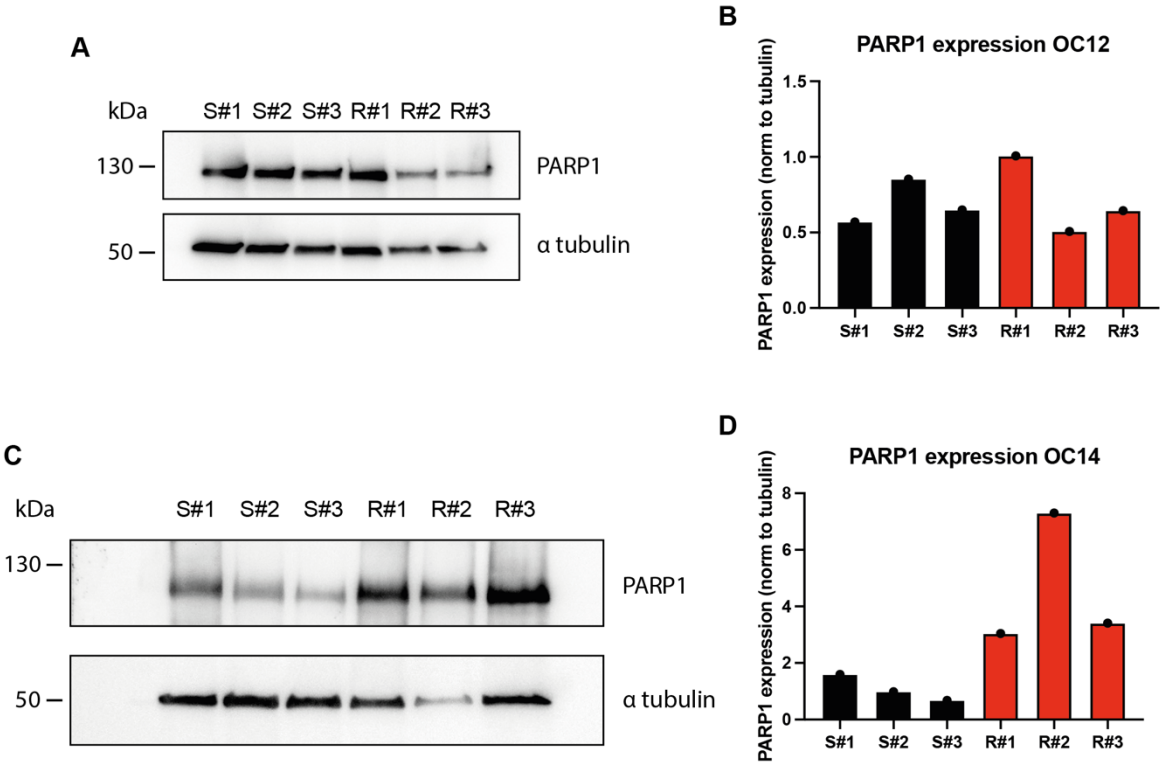

suppl. Figure 6 PARP1 protein expression levels in olaparib resistant and sensitive OC12 and OC14 cell lines based on western blot analysis.

A protein expression of PARP1 based on western blot analysis of olaparib resistant and sensitive OC12 cells (R/S#1.2.3); a-tubulin was used as loading control. **B** Quantification of PARP1 protein levels on OC12 cells detected in western blot analysis (A), PARP1 protein levels were normalized to the a-tubulin loading control. **C** protein expression of PARP1 based on western blot analysis of olaparib resistant and sensitive OC14 cells (R/S#1.2.3); a-tubulin was used as loading control. **D** Quantification of PARP1 protein levels in OC14 cells detected in western blot analysis (C), PARP1 protein levels were normalized to the a-tubulin loading control.

A

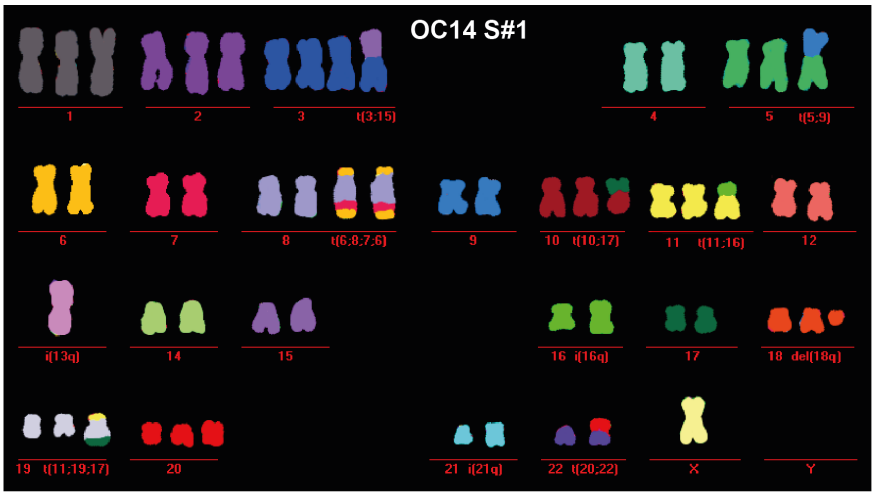

B

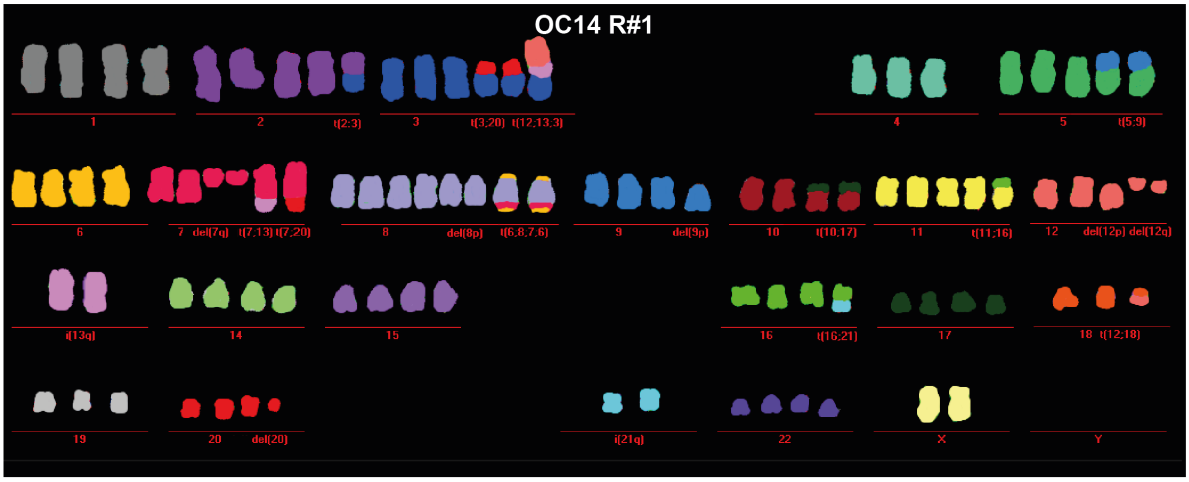

C

Chromosome	Sensitive 1 (n = 55-57)	Resistant 1 (n= 84-96)
3	3 x 2 der(3)t(3;15) x1	3 x4 der(3)t(3;20) x2
12	12 x3	12 x5 del(12q) x2
16	16 x2	16 x3 der(16)t(16;21) x1
19	19 x2 der(19)t(11;19;17) x1	19 x3
20	20 x3	20 x3 der(20)t(17;20) x1
X	X x1 del(Xp) x1	X x2

suppl. Figure 7 M-FISH analysis of OC14 S#1 and R#1 cell lines, indicating chromosomal rearrangements in olaparib-resistant cells.

A M-FISH analysis of OC14 S#1 cells. **B** M-FISH analysis of OC14 R#1 cells. **C** Table highlighting chromosomal differences between R#1 and S#1 cells. der = derivate, del = deletion, t = translocation.

A

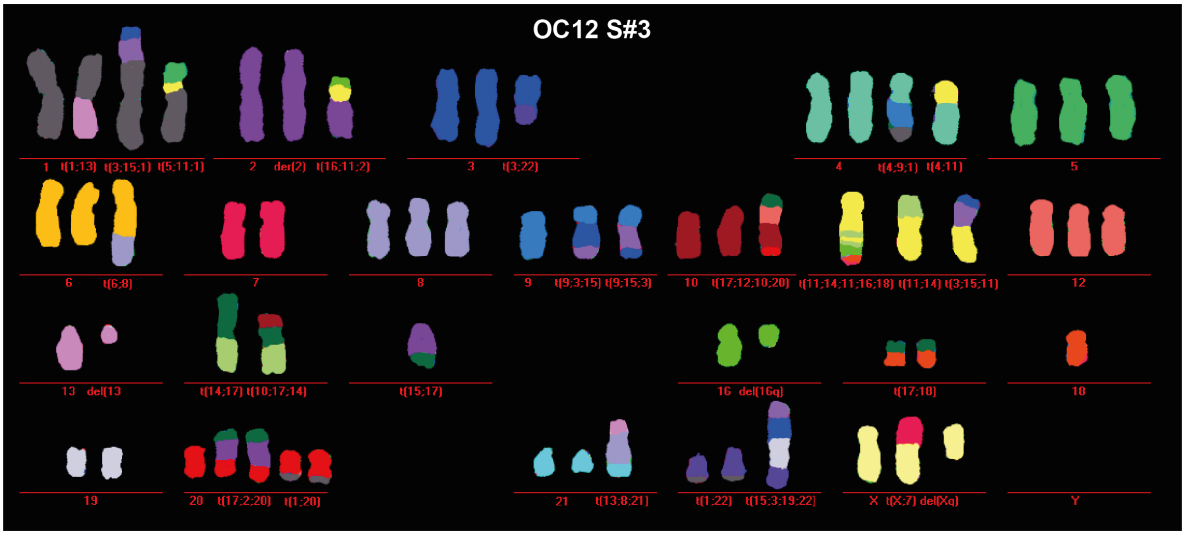

B

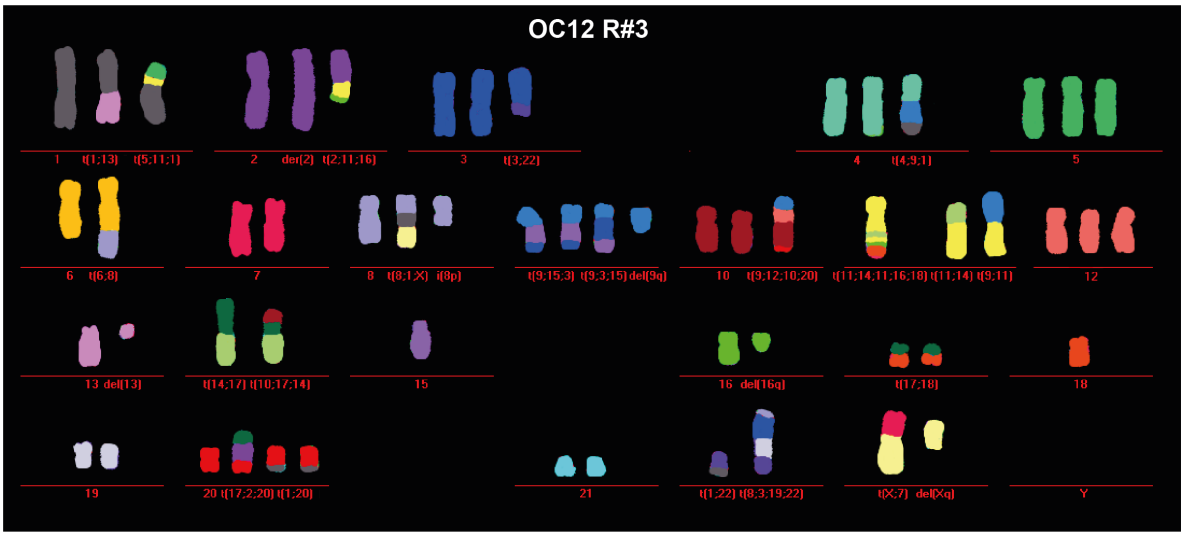

C

Chromosome	Sensitive 3 (n = 58-63)	Resistant 3 (n= 55-57)
1	1 x1 der(1)t(1;13) x1 der(1)t(5;11;1) x1 **der(1)t(3;15;1) x1**	1 x1 der(1)t(1;13) x1 der(1)t(5;11;1) x1 der(1)t(X;1) x1
13	13 x1 der(13)t(9;13) x1	13 x1 del(13) x1
15	der(15)t(15;20) x1 or der(15)t(3;15) x1	15 x1
21	21 x2 der(21)t(13;8;21) x1	21 x2

suppl. Figure 8 M-FISH analysis of OC12 R#3 and S#3 cell lines showing a triploid genotype.
A M-FISH analysis of OC12 S#3 cells. **B** M-FISH analysis of OC12 R#3 cells. **C** Table highlighting chromosomal differences between R#3 and S#3 cell lines. der = derivate, t = translocation.

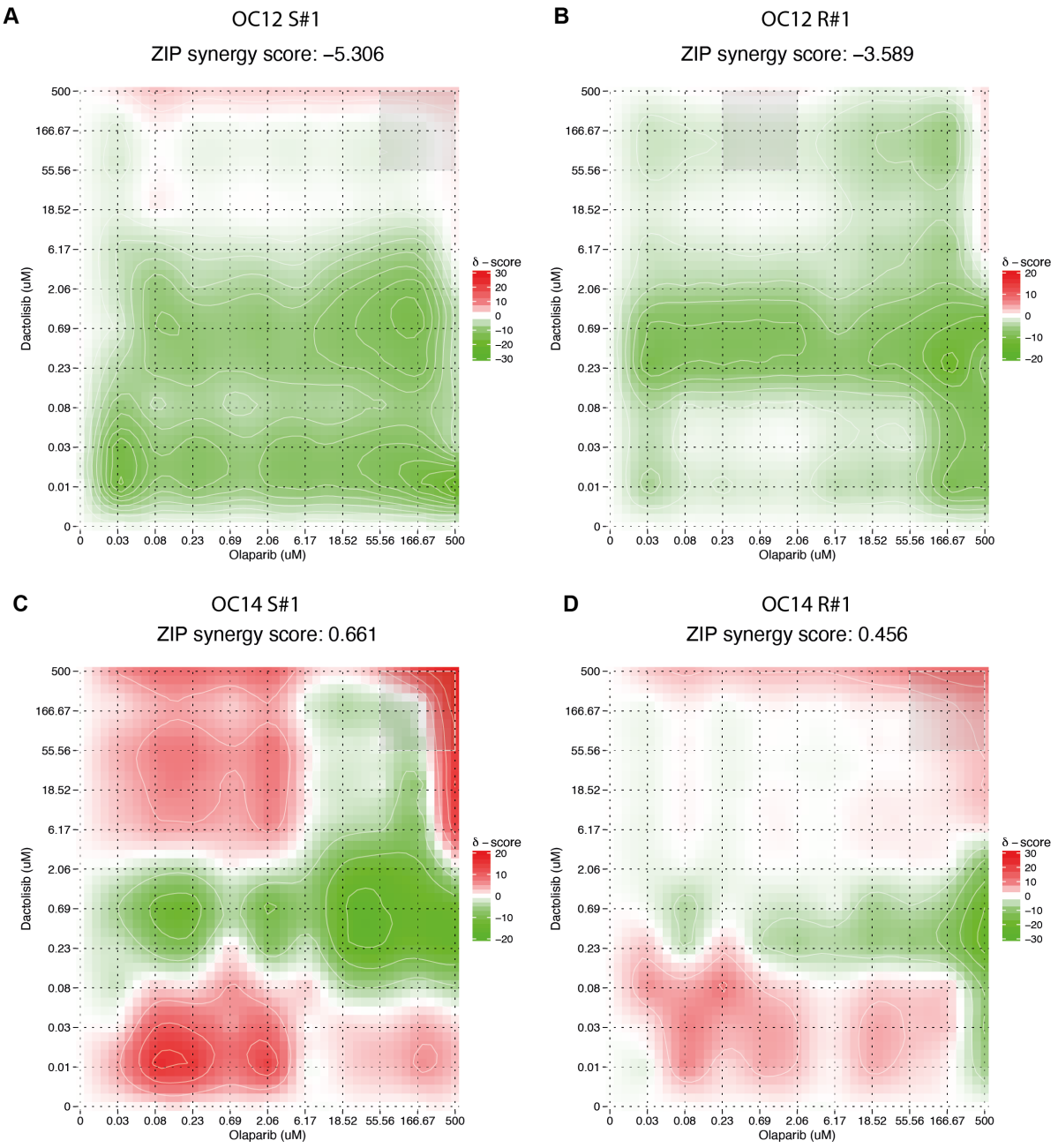

suppl. Figure 9 Cross titration with olaparib and the PI3K/mTOR inhibitor (dactolisib) revealed no synergy between both drugs in OC12 and OC14 R#1 and S#1.

A Synergy score matrix for OC12 S#1 following 72 h of combined olaparib and dactolisib treatment. Normalized cell viability was used to calculate combination effects utilizing the SynergyFinder [162] zero-interaction potency (ZIP) score model with baseline correction. **B** Synergy score matrix for OC12 R#1 following 72 h of combined olaparib and dactolisib treatment. Normalized cell viability was used to calculate combination effects utilizing ZIP score model with baseline correction. **C** Synergy score matrix for OC14 S#1 following 72 h of combined olaparib and dactolisib treatment. Normalized cell viability was used to calculate combination effects utilizing the ZIP score model with baseline correction. **D** Synergy score matrix for OC14 R#1 following 72 h of combined olaparib and dactolisib treatment. Normalized cell viability was used to calculate combination effects utilizing ZIP score model with baseline correction. Synergy scores (δ-scores) between 0 and 10 suggest the interaction between the two drugs is likely additive, while synergy scores larger than 10 indicate the interaction between the two drugs is probably synergistic.

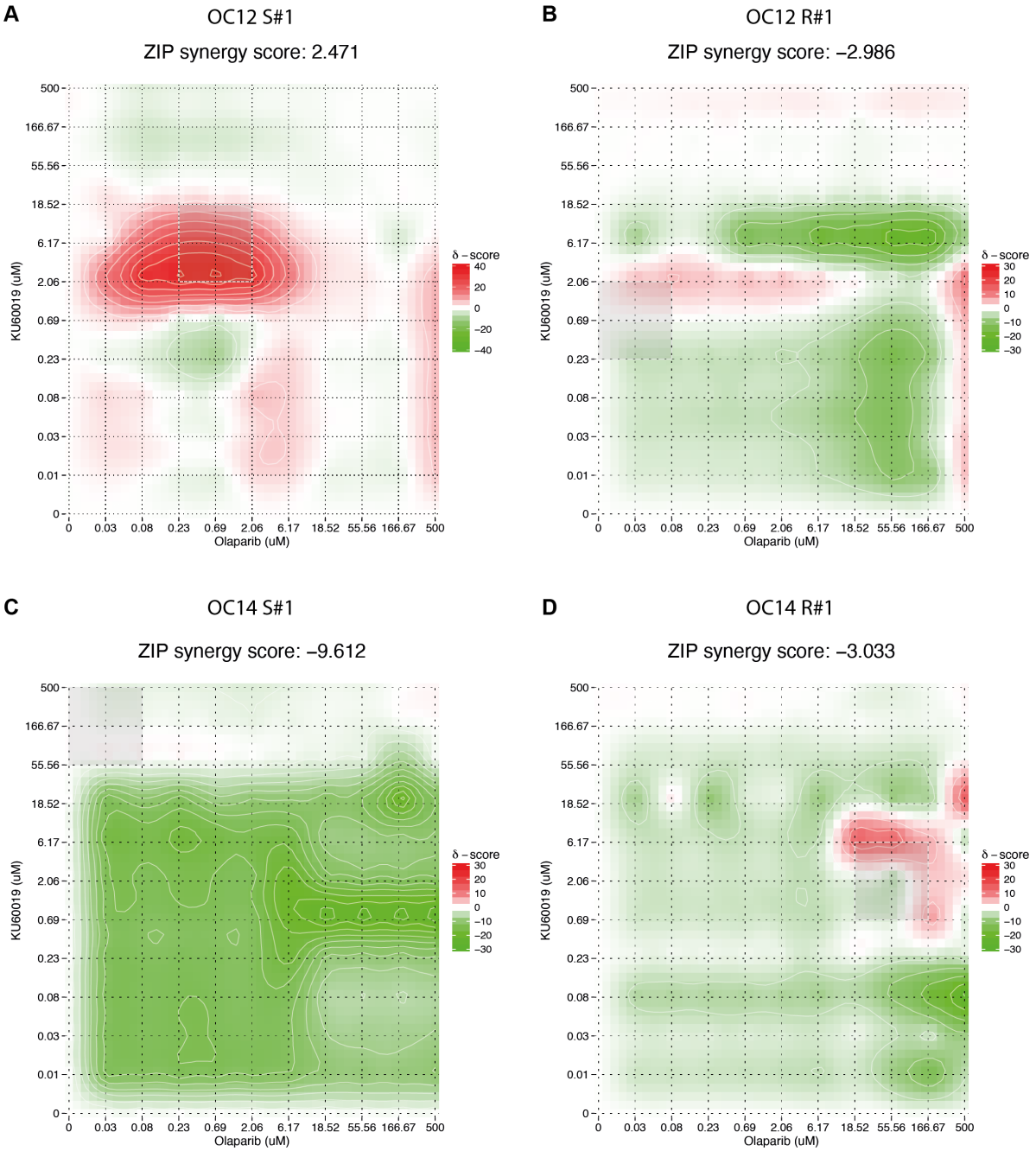

suppl. Figure 10 Cross titration with olaparib and the ATM inhibitor (KU60019) revealed no synergy between both drugs in OC12 and OC14 R#1 and S#1.

A Synergy score matrix for OC12 S#1 following 72 h of combined olaparib and KU60019 treatment. Normalized cell viability was used to calculate combination effects utilizing the ZIP score model with baseline correction. **B** Synergy score matrix for OC12 R#1 following 72 h of combined olaparib and KU60019 treatment. Normalized cell viability was used to calculate combination effects utilizing ZIP score model with baseline correction. **C** Synergy score matrix for OC14 S#1 following 72 h of combined olaparib and KU60019 treatment. Normalized cell viability was used to calculate combination effects utilizing the ZIP score model with baseline correction. **D** Synergy score matrix for OC14 R#1 following 72 h of combined olaparib and KU60019 treatment. Normalized cell viability was used to calculate combination effects utilizing ZIP score model with baseline correction. Synergy scores (δ-scores) between 0 and 10 suggest the interaction between the two drugs is likely additive, while synergy scores larger than 10 indicate the interaction between the two drugs is probably synergistic.

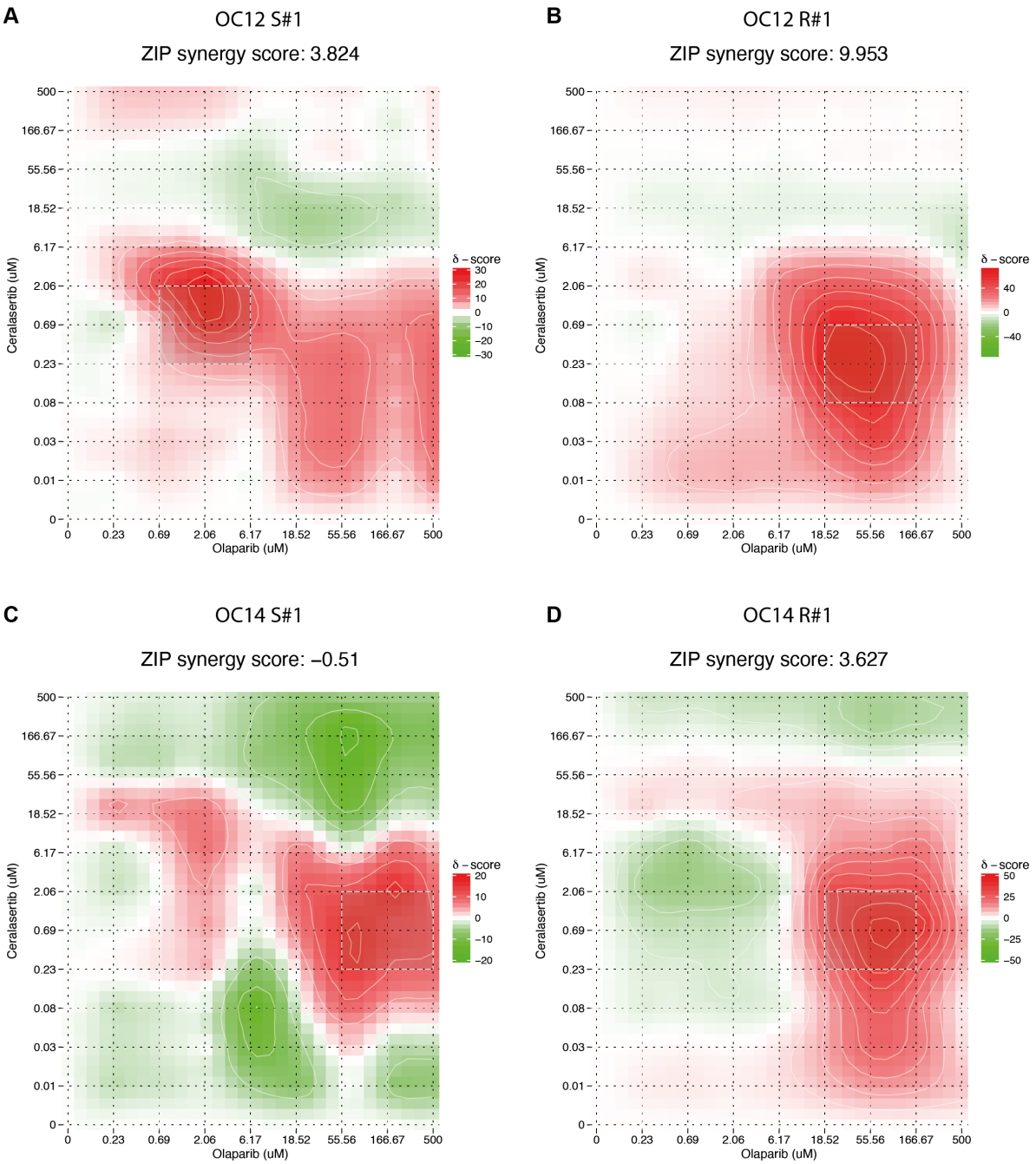

suppl. Figure 11 Cross titration with olaparib and the ATR inhibitor (Ceralasertib) revealed no synergy between both drugs in OC12 and OC14 R#1 and S#1.

A Synergy score matrix for OC12 S#1 following 72 h of combined olaparib and ceralasertib treatment. Normalized cell viability was used to calculate combination effects utilizing the ZIP score model with baseline correction. **B** Synergy score matrix for OC12 R#1 following 72 h of combined olaparib and ceralasertib treatment. Normalized cell viability was used to calculate combination effects utilizing ZIP score model with baseline correction. **C** Synergy score matrix for OC14 S#1 following 72 h of combined olaparib and ceralasertib treatment. Normalized cell viability was used to calculate combination effects utilizing the ZIP score model with baseline correction. **D** Synergy score matrix for OC14 R#1 following 72 h of combined olaparib and ceralasertib treatment. Normalized cell viability was used to calculate combination effects utilizing ZIP score model with baseline correction. Synergy scores (δ-scores) between 0 and 10 suggest the interaction between the two drugs is likely additive, while synergy scores larger than 10 indicate the interaction between the two drugs is probably synergistic.

Table 20 Functional mutations in resistant OC12 cells that are not present in basal or sensitive OC12 cell lines

Gene	Exonic classification	Annovar Transcripts
VKORC1L1	nonframeshift deletion	VKORC1L1:ENST00000434382.2:exon2:c.488_490del:p.163_164del,
PRMT3	frameshift deletion	PRMT3:ENST00000437750.2:exon8:c.788delT:p.V263fs, PRMT3:ENST00000331079.6:exon10:c.974delT:p.V325fs,
NUTM1	frameshift deletion	NUTM1:ENST00000537011.1:exon8:c.2943_2959del:p.Q981fs, NUTM1:ENST00000333756.4:exon7:c.2859_2875del:p.Q953fs, NUTM1:ENST00000438749.3:exon7:c.2913_2929del:p.Q971fs,
DCXR	frameshift deletion	DCXR:ENST00000577532.1:exon6:c.499_517del:p.T167fs,
FAM155B	nonframeshift deletion	FAM155B:ENST00000252338.4:exon1:c.54_56del:p.18_19del,
NR0B2	nonframeshift deletion	NR0B2:ENST00000254227.3:exon2:c.699_719del:p.233_240del,
NR0B2	frameshift insertion	NR0B2:ENST00000254227.3:exon2:c.693_694insAGATG:p.L232fs,
AHDC1	nonframeshift deletion	AHDC1:ENST00000374011.2:exon6:c.3272_3274del:p.1091_1092del, AHDC1:ENST00000247087.5:exon5:c.3272_3274del:p.1091_1092del,
ALG10B	frameshift deletion	ALG10B:ENST00000308742.4:exon3:c.873delA:p.L291fs,
AVEN	nonframeshift deletion	AVEN:ENST00000306730.3:exon1:c.123_134del:p.41_45del,

Table 21 Single nucleotide variants (SNVs) in resistant OC12 cells that are not present in basal and sensitive cells

Annovar function	gene	Exonic classififcation
exonic	OR10J5	stopgain
exonic	ALMS1	nonsynonymous SNV
exonic	CCDC93	nonsynonymous SNV
exonic	IGSF11	nonsynonymous SNV
exonic	ATP13A3	nonsynonymous SNV
exonic	CRIPAK	nonsynonymous SNV
exonic	SPOCK3	nonsynonymous SNV
exonic	CDC5L	nonsynonymous SNV
exonic	SLA	stopgain
exonic	SPATA6L	nonsynonymous SNV
splicing	SNX30(ENST00000374232.3:exon7:c.1101+2T>C,ENST00000416585.1:exon2:c.200+2T>C)	
exonic	PKN3	nonsynonymous SNV
exonic	RNLS	nonsynonymous SNV
exonic	SORCS1	nonsynonymous SNV
exonic	CLRN3	stopgain
exonic	OR51F1	nonsynonymous SNV
exonic	OR51Q1	nonsynonymous SNV
exonic	WNT11	nonsynonymous SNV
exonic	ZNF740	nonsynonymous SNV
exonic	SALL2	nonsynonymous SNV

exonic	SERPINA12	nonsynonymous SNV
exonic	IGHV1OR15-1	nonsynonymous SNV
exonic	NDUFAF1	nonsynonymous SNV
splicing	LTK(ENST00000561619.1:exon5:c.439+1G>A)	.
exonic	GANC	nonsynonymous SNV
exonic	WDR76	nonsynonymous SNV
exonic	SCG3	nonsynonymous SNV
exonic	FAM214A	nonsynonymous SNV
exonic	DYX1C1	nonsynonymous SNV
exonic	CGNL1	nonsynonymous SNV
exonic	CGNL1	nonsynonymous SNV
exonic	HERC1	nonsynonymous SNV
exonic	SMAD3	nonsynonymous SNV
exonic	NOX5	nonsynonymous SNV
splicing	CD276	.
exonic	WHAMM	nonsynonymous SNV
exonic	DET1	nonsynonymous SNV
exonic	ZNF774	nonsynonymous SNV
exonic	SYNM	nonsynonymous SNV
exonic	LRRK1	nonsynonymous SNV
exonic	PSMB6	nonsynonymous SNV
exonic	TNRC6C	nonsynonymous SNV
exonic	ENGASE	nonsynonymous SNV
exonic	ASPSCR1	nonsynonymous SNV
exonic	ABCE1	nonsynonymous SNV
exonic	AL390778.1	nonsynonymous SNV
exonic	RYR3	nonsynonymous SNV
exonic	BUB1B	nonsynonymous SNV
exonic	ZNF729	nonsynonymous SNV
exonic	CCT8L2	nonsynonymous SNV
exonic	KLHL22	nonsynonymous SNV
exonic	HUWE1	nonsynonymous SNV
exonic	ARHGEF10L	nonsynonymous SNV
exonic	BTBD19	nonsynonymous SNV
exonic	PGBD5	stopgain
exonic	ABCG5	nonsynonymous SNV
exonic	PRPF40A	nonsynonymous SNV
exonic	TTN	nonsynonymous SNV
exonic	ZNF621	stopgain
exonic	GC	nonsynonymous SNV
exonic	HRH2	stopgain
exonic	TREML4	nonsynonymous SNV
exonic	MDN1	nonsynonymous SNV
exonic	HECW1	nonsynonymous SNV
exonic	ASB15	nonsynonymous SNV
exonic	GIMAP7	nonsynonymous SNV
exonic	C5	nonsynonymous SNV
exonic	COL5A1	nonsynonymous SNV
exonic	ACBD5	stopgain
exonic	PDZD7	nonsynonymous SNV
exonic	AP2A2	nonsynonymous SNV
splicing	USP28(ENST00000003302.4:exon20:c.2305-1G>T,ENST00000538224.1:exon5:c.368-1G>T)	.
splicing	HOXC11(ENST00000546378.1:exon2:c.683-2A>C,ENST00000243082.4:exon2:c.687-2A>C)	.
exonic	LTBP2	stopgain
exonic	MYH8	nonsynonymous SNV
exonic	SSH2	nonsynonymous SNV
splicing	AXIN2	.
exonic	OR10H4	nonsynonymous SNV
exonic	LILRA4	nonsynonymous SNV
exonic	SLC12A5	nonsynonymous SNV
exonic	CXorf21	stopgain
exonic	DMD	nonsynonymous SNV
exonic	DMD	stopgain
exonic	DMD	nonsynonymous SNV

Table 22 Functional mutations in resistant OC14 cells that are not present in basal or sensitive OC14 cell lines

Gene	Exonic classification	Annovar Transcripts
KLHL41	frameshift deletion	KLHL41:ENST00000284669.1:exon1:c.401_402del:p.N134fs,
DDIT4L	frameshift deletion	DDIT4L:ENST00000273990.2:exon3:c.540delA:p.K180fs,
METTL17	frameshift deletion	METTL17:ENST00000554283.1:exon1:c.122_125del:p.P41fs,
TRAV19	frameshift deletion	TRAV19:ENST00000390447.3:exon2:c.68_71del:p.K23fs,
NOP9	nonframeshift insertion	NOP9:ENST00000267425.3:exon2:c.484_485insGAGGAGGAG:p.E162delinsGGGE, NOP9:ENST00000396802.3:exon2:c.484_485insGAGGAGGAG:p.E162delinsGGGE,
SSTR1	nonframeshift insertion	SSTR1:ENST00000267377.2:exon3:c.1170_1171insGCTCTGAGCCCGGGCCACGCAGGG:p.T390delinsTALSPGHAG,
RP11-131H24.4	frameshift deletion	RP11-131H24.4:ENST00000557646.1:exon5:c.167delA:p.Q56fs,
RTL1	nonframeshift insertion	RTL1:ENST00000534062.1:exon1:c.454_455insAGA:p.E152delinsEK,
EXOC3L4	unknown	UNKNOWN
RP11-467N20.5	nonframeshift deletion	RP11-467N20.5:ENST00000558241.1:exon8:c.2314_2316del:p.772_772del,
TPTE	nonframeshift deletion	TPTE:ENST00000361285.4:exon12:c.660_662del:p.220_221del, TPTE:ENST00000298232.7:exon11:c.606_608del:p.202_203del, TPTE:ENST00000342420.5:exon10:c.546_548del:p.182_183del,

Table 23 Single nucleotide variants (SNVs) in resistant OC14 cells that are not present in basal and sensitive cells

Annovar function	gene	Exonic classififcation
exonic	ADAM15	nonsynonymous SNV
exonic	OR10K1	nonsynonymous SNV
exonic	FCRL6	nonsynonymous SNV
exonic	LRRC52	nonsynonymous SNV
exonic	NR5A2	nonsynonymous SNV
exonic	LAMB3	nonsynonymous SNV
exonic	OR2AJ1	nonsynonymous SNV
exonic	OR2G6	nonsynonymous SNV
exonic	DHX57	nonsynonymous SNV
exonic	IWS1	nonsynonymous SNV
exonic	ZEB2	stopgain
exonic	SLC4A10	nonsynonymous SNV
exonic	TTC30B	nonsynonymous SNV
exonic	CCDC141	nonsynonymous SNV
exonic	STAT1	nonsynonymous SNV
exonic	AC104809.3	nonsynonymous SNV
exonic	UBA5	nonsynonymous SNV
exonic	PCYT1A	nonsynonymous SNV
exonic	ZNF732	nonsynonymous SNV
exonic	ZNF721	nonsynonymous SNV
splicing	PDE6B	.
exonic	NOP14	nonsynonymous SNV
exonic	GRK4	nonsynonymous SNV
exonic	HTT	nonsynonymous SNV
exonic	MSANTD1	nonsynonymous SNV
exonic	AL590235.1	nonsynonymous SNV
exonic	STX18	nonsynonymous SNV
exonic	C4orf50	nonsynonymous SNV
exonic	SH3TC1	nonsynonymous SNV

exonic	TBC1D1	nonsynonymous SNV
exonic	LIMCH1	nonsynonymous SNV
exonic	CENPC	nonsynonymous SNV
exonic	UGT2B7	nonsynonymous SNV
exonic	NAAA	nonsynonymous SNV
exonic	SHROOM3	nonsynonymous SNV
exonic	ANTXR2	nonsynonymous SNV
exonic	CDS1	nonsynonymous SNV
exonic	MTTP	nonsynonymous SNV
exonic	BANK1	nonsynonymous SNV
exonic	TBCK	nonsynonymous SNV
splicing	HADH(ENST00000511742.1:exon3:c.387-1G>C)	.
exonic	LRIT3	nonsynonymous SNV
exonic	C4orf21	nonsynonymous SNV
exonic	ANK2	nonsynonymous SNV
exonic	PDE5A	nonsynonymous SNV
exonic	KIAA1109	nonsynonymous SNV
exonic	NUDT6	nonsynonymous SNV
exonic	FAT4	nonsynonymous SNV
exonic	HSPA4L	nonsynonymous SNV
exonic	PLK4	nonsynonymous SNV
exonic	DCHS2	nonsynonymous SNV
exonic	FGB	nonsynonymous SNV
exonic	FGA	nonsynonymous SNV
exonic	TDO2	nonsynonymous SNV
exonic	FSTL5	nonsynonymous SNV
exonic	NAF1	nonsynonymous SNV
exonic	ANXA10	nonsynonymous SNV
exonic	DDX60	nonsynonymous SNV
exonic	DDX60	nonsynonymous SNV
exonic	DDX60L	nonsynonymous SNV
exonic	GALNT7	nonsynonymous SNV
exonic	CLDN24	nonsynonymous SNV
exonic	MLF1IP	nonsynonymous SNV
exonic	FAT1	nonsynonymous SNV
exonic	FAT1	nonsynonymous SNV
exonic	FAT1	nonsynonymous SNV
exonic	AGGF1	nonsynonymous SNV
exonic	PCDHB12	nonsynonymous SNV
exonic	MCUR1	nonsynonymous SNV
exonic	MCUR1	stopgain
exonic	MICA	nonsynonymous SNV
exonic	COL11A2	nonsynonymous SNV
exonic	VNN1	nonsynonymous SNV
exonic	OSBPL3	nonsynonymous SNV
exonic	ZNF716	nonsynonymous SNV
exonic	REPIN1	nonsynonymous SNV
exonic	GIMAP7	nonsynonymous SNV
exonic	TACC1	nonsynonymous SNV
exonic	BARX1	nonsynonymous SNV
exonic	OR5C1	nonsynonymous SNV
exonic	AL390778.1	nonsynonymous SNV
exonic	MYOF	nonsynonymous SNV
exonic	OR6T1	nonsynonymous SNV
exonic	GYS2	stopgain
exonic	RP11-571M6.15,TSFM	nonsynonymous SNV
exonic	RIMBP2	nonsynonymous SNV
exonic	OR4K1	nonsynonymous SNV
exonic	OR11H6	nonsynonymous SNV
splicing	RNASE9(ENST00000553706.1:exon5:c.1+1G>A,ENST00000557209.1:exon4:c.1+1G>A)	.
exonic	SLC39A2	nonsynonymous SNV
exonic	SALL2	nonsynonymous SNV
exonic	TRDV1	nonsynonymous SNV
exonic	ACIN1	nonsynonymous SNV
exonic	ACIN1	nonsynonymous SNV
exonic	IPO4	nonsynonymous SNV
exonic	NFATC4	nonsynonymous SNV
exonic	NFATC4	nonsynonymous SNV
exonic	NYNRIN	nonsynonymous SNV

exonic	SFTA3	nonsynonymous SNV
exonic	PAX9	nonsynonymous SNV
exonic	FOXA1	nonsynonymous SNV
exonic	TTC6	nonsynonymous SNV
exonic	TTC6	nonsynonymous SNV
exonic	FSCB	nonsynonymous SNV
exonic	DNAAF2	nonsynonymous SNV
exonic	VCPKMT	nonsynonymous SNV
exonic	L2HGDH	nonsynonymous SNV
exonic	ATP5S	nonsynonymous SNV
exonic	ATP5S	nonsynonymous SNV
exonic	CDKL1	nonsynonymous SNV
exonic	PYGL	nonsynonymous SNV
exonic	ABHD12B	nonsynonymous SNV
exonic	TXNDC16	nonsynonymous SNV
exonic	DDHD1	nonsynonymous SNV
exonic	KIAA0586	nonsynonymous SNV
exonic	CCDC175	nonsynonymous SNV
exonic	SIX4	nonsynonymous SNV
exonic	SYNE2	nonsynonymous SNV
exonic	ZFYVE26	nonsynonymous SNV
exonic	ZFP36L1	nonsynonymous SNV
exonic	RGS6	nonsynonymous SNV
exonic	FAM161B	nonsynonymous SNV
exonic	COQ6	nonsynonymous SNV
exonic	SAMD15	nonsynonymous SNV
exonic	SPTLC2	nonsynonymous SNV
exonic	FLRT2	nonsynonymous SNV
exonic	GALC	nonsynonymous SNV
exonic	KCNK10	nonsynonymous SNV
exonic	GOLGA5	nonsynonymous SNV
exonic	UNC79	nonsynonymous SNV
exonic	SERPINA1	nonsynonymous SNV
splicing	WARS	.
exonic	WDR25	nonsynonymous SNV
exonic	ZNF839	nonsynonymous SNV
exonic	RD3L	nonsynonymous SNV
exonic	ASPG	nonsynonymous SNV
exonic	ASPG	nonsynonymous SNV
exonic	C14orf79	nonsynonymous SNV
exonic	BRF1	nonsynonymous SNV
exonic	IGHG2	nonsynonymous SNV
exonic	IGHM	nonsynonymous SNV
exonic	IGHV3-11	nonsynonymous SNV
exonic	IGHV3-11	nonsynonymous SNV
exonic	IGHV3-11	nonsynonymous SNV
exonic	IGHV3-11	nonsynonymous SNV
exonic	IGHV3-11	nonsynonymous SNV
exonic	IGHV3-21	nonsynonymous SNV
exonic	IGHV4-39	nonsynonymous SNV
exonic	IGHV3-53	nonsynonymous SNV
exonic	IGHV1-69	nonsynonymous SNV
splicing	TRPM7(ENST00000560955.1:exon35:c.4733-2A>T,ENST00000313478.7:exon35:c.4736-2A>T)	.
exonic	SMAD6	nonsynonymous SNV
exonic	RAD51C	nonsynonymous SNV
exonic	ABCA10	stopgain
exonic	CD7	nonsynonymous SNV
exonic	MYO5B	nonsynonymous SNV
splicing	SEC11C(ENST00000587834.1:exon2:c.88-2A>G,ENST00000299714.3:exon2:c.88-2A>G,ENST00000588875.1:exon2:c.88-2A>G)	.
exonic	FBN3	nonsynonymous SNV
exonic	DNM2,TMED1	nonsynonymous SNV
exonic	ZNF433	nonsynonymous SNV
exonic	ZNF433	nonsynonymous SNV
exonic	RFX1	nonsynonymous SNV
exonic	FCGBP	nonsynonymous SNV
exonic	ZNF235	stopgain
exonic	LILRB4	nonsynonymous SNV

exonic	PPP1R12C	nonsynonymous SNV
exonic	FRG1B	nonsynonymous SNV
exonic	SAMHD1	nonsynonymous SNV
exonic	GART	nonsynonymous SNV
exonic	AP001055.1	nonsynonymous SNV
exonic	ICOSLG	nonsynonymous SNV
exonic	ICOSLG	nonsynonymous SNV
exonic	ICOSLG	nonsynonymous SNV
exonic	SLC25A17	nonsynonymous SNV
exonic	IL1RAPL1	nonsynonymous SNV
exonic	LPAR4	nonsynonymous SNV
exonic	FCRL5	nonsynonymous SNV
exonic	HHIPL2	stopgain
exonic	URB2	nonsynonymous SNV
exonic	CHML	nonsynonymous SNV
exonic	NLRP3	nonsynonymous SNV
exonic	SHISA5	nonsynonymous SNV
exonic	TXK	nonsynonymous SNV
exonic	LRIT3	nonsynonymous SNV
exonic	SLC27A6	nonsynonymous SNV
exonic	ITPR3	nonsynonymous SNV
exonic	PKHD1	nonsynonymous SNV
exonic	ZFAT	nonsynonymous SNV
exonic	TEK	nonsynonymous SNV
exonic	ADARB2	nonsynonymous SNV
exonic	IL18BP	nonsynonymous SNV
exonic	FAT3	nonsynonymous SNV
exonic	NXPE4	stopgain
exonic	SLC6A12	nonsynonymous SNV
exonic	OLR1	nonsynonymous SNV
exonic	ZNF280D	nonsynonymous SNV
exonic	SKOR1	nonsynonymous SNV
exonic	ZNF774	nonsynonymous SNV
exonic	MYO5B	nonsynonymous SNV
exonic	CACNA1A	nonsynonymous SNV
exonic	PGLS	nonsynonymous SNV
exonic	CLPTM1	nonsynonymous SNV
exonic	RPA4	nonsynonymous SNV
exonic	AMOT	nonsynonymous SNV
exonic	RBMXL3	nonsynonymous SNV
exonic	FATE1	nonsynonymous SNV
exonic	MAST2	nonsynonymous SNV
exonic	DNAH14	nonsynonymous SNV
exonic	GTF3C2	nonsynonymous SNV
exonic	SIX2	nonsynonymous SNV
exonic	CHST10	nonsynonymous SNV
exonic	CYTIP	nonsynonymous SNV
exonic	KIAA1715	stopgain
exonic	HOXD9	nonsynonymous SNV
exonic	OSBPL10	nonsynonymous SNV
exonic	TOMM70A	nonsynonymous SNV
exonic	FREM3	nonsynonymous SNV
exonic	SMAP1	nonsynonymous SNV
exonic	PXDNL	nonsynonymous SNV
exonic	NAA35	stopgain
exonic	TEX10	nonsynonymous SNV
exonic	ZNF248	nonsynonymous SNV
exonic	DKK1	nonsynonymous SNV
exonic	REEP3	nonsynonymous SNV
exonic	LRIT2	nonsynonymous SNV
exonic	CCDC172	nonsynonymous SNV
exonic	OR51L1	nonsynonymous SNV
exonic	YBX3	nonsynonymous SNV
exonic	ATXN7L3B	nonsynonymous SNV
exonic	PRDM4	nonsynonymous SNV
exonic	RFXAP	nonsynonymous SNV
exonic	TRPC4	nonsynonymous SNV
exonic	TNFSF11	nonsynonymous SNV
exonic	PRM2	nonsynonymous SNV

exonic	KRT35	nonsynonymous SNV
exonic	AARSD1	nonsynonymous SNV
exonic	PSMD12	nonsynonymous SNV
exonic	FASN	nonsynonymous SNV
exonic	CELF4	stopgain
exonic	CDH20	stopgain
exonic	CDH20	nonsynonymous SNV
exonic	TMEM38A	nonsynonymous SNV
exonic	PRR12	nonsynonymous SNV
exonic	USP29	stopgain
exonic	TFIP11	nonsynonymous SNV
exonic	TST	nonsynonymous SNV
exonic	KLHL4	nonsynonymous SNV

7. References

1. Kossai, M., et al., *Ovarian Cancer: A Heterogeneous Disease.* Pathobiology, 2018. **85**(1-2): p. 41-49.
2. Siegel, R.L., et al., *Cancer statistics, 2023.* CA Cancer J Clin, 2023. **73**(1): p. 17-48.
3. Stewart, C., C. Ralyea, and S. Lockwood, *Ovarian Cancer: An Integrated Review.* Semin Oncol Nurs, 2019. **35**(2): p. 151-156.
4. Siegel, R.L., K.D. Miller, and A. Jemal, *Cancer statistics, 2020.* CA Cancer J Clin, 2020. **70**(1): p. 7-30.
5. Bast, R.C., Jr., B. Hennessy, and G.B. Mills, *The biology of ovarian cancer: new opportunities for translation.* Nat Rev Cancer, 2009. **9**(6): p. 415-28.
6. Matulonis, U.A., et al., *Ovarian cancer.* Nat Rev Dis Primers, 2016. **2**: p. 16061.
7. Cancer Genome Atlas Research, N., *Integrated genomic analyses of ovarian carcinoma.* Nature, 2011. **474**(7353): p. 609-15.
8. Konstantinopoulos, P.A., et al., *Homologous Recombination Deficiency: Exploiting the Fundamental Vulnerability of Ovarian Cancer.* Cancer Discov, 2015. **5**(11): p. 1137-54.
9. Bassuk, S.S. and J.E. Manson, *Oral contraceptives and menopausal hormone therapy: relative and attributable risks of cardiovascular disease, cancer, and other health outcomes.* Ann Epidemiol, 2015. **25**(3): p. 193-200.
10. Kurian, A.W., et al., *Histologic types of epithelial ovarian cancer: have they different risk factors?* Gynecol Oncol, 2005. **96**(2): p. 520-30.
11. Gorski, J.W., F.R. Ueland, and J.M. Kolesar, *CCNE1 Amplification as a Predictive Biomarker of Chemotherapy Resistance in Epithelial Ovarian Cancer.* Diagnostics (Basel), 2020. **10**(5).
12. Narod, S., *Can advanced-stage ovarian cancer be cured?* Nat Rev Clin Oncol, 2016. **13**(4): p. 255-61.
13. Hanahan, D. and R.A. Weinberg, *Hallmarks of cancer: the next generation.* Cell, 2011. **144**(5): p. 646-74.
14. Gee, M.E., et al., *DNA damage repair in ovarian cancer: unlocking the heterogeneity.* J Ovarian Res, 2018. **11**(1): p. 50.
15. Lord, C.J. and A. Ashworth, *PARP inhibitors: Synthetic lethality in the clinic.* Science, 2017. **355**(6330): p. 1152-1158.
16. Liu, J.F., P.A. Konstantinopoulos, and U.A. Matulonis, *PARP inhibitors in ovarian cancer: current status and future promise.* Gynecol Oncol, 2014. **133**(2): p. 362-9.
17. Lindahl, T. and D.E. Barnes, *Repair of endogenous DNA damage.* Cold Spring Harb Symp Quant Biol, 2000. **65**: p. 127-33.
18. Kim, Y.J. and D.M. Wilson, 3rd, *Overview of base excision repair biochemistry.* Curr Mol Pharmacol, 2012. **5**(1): p. 3-13.
19. Tubbs, A. and A. Nussenzweig, *Endogenous DNA Damage as a Source of Genomic Instability in Cancer.* Cell, 2017. **168**(4): p. 644-656.
20. Caldecott, K.W., *DNA single-strand break repair.* Exp Cell Res, 2014. **329**(1): p. 2-8.
21. Caldecott, K.W., *Single-strand break repair and genetic disease.* Nat Rev Genet, 2008. **9**(8): p. 619-31.
22. Hoeijmakers, J.H., *DNA damage, aging, and cancer.* N Engl J Med, 2009. **361**(15): p. 1475-85.
23. Zhang, X., M. Yin, and J. Hu, *Nucleotide excision repair: a versatile and smart toolkit.* Acta Biochim Biophys Sin (Shanghai), 2022. **54**(6): p. 807-819.
24. Lieber, M.R., *The mechanism of double-strand DNA break repair by the nonhomologous DNA end-joining pathway.* Annu Rev Biochem, 2010. **79**: p. 181-211.

25. Ranjha, L., S.M. Howard, and P. Cejka, *Main steps in DNA double-strand break repair: an introduction to homologous recombination and related processes.* Chromosoma, 2018. **127**(2): p. 187-214.
26. Chang, H.H.Y., et al., *Non-homologous DNA end joining and alternative pathways to double-strand break repair.* Nat Rev Mol Cell Biol, 2017. **18**(8): p. 495-506.
27. Scully, R., et al., *DNA double-strand break repair-pathway choice in somatic mammalian cells.* Nat Rev Mol Cell Biol, 2019. **20**(11): p. 698-714.
28. Zhao, B., et al., *The molecular basis and disease relevance of non-homologous DNA end joining.* Nat Rev Mol Cell Biol, 2020. **21**(12): p. 765-781.
29. Kanaar, R., J.H. Hoeijmakers, and D.C. van Gent, *Molecular mechanisms of DNA double strand break repair.* Trends Cell Biol, 1998. **8**(12): p. 483-9.
30. Mladenov, E., et al., *DNA double-strand-break repair in higher eukaryotes and its role in genomic instability and cancer: Cell cycle and proliferation-dependent regulation.* Semin Cancer Biol, 2016. **37-38**: p. 51-64.
31. Bizard, A.H. and I.D. Hickson, *The dissolution of double Holliday junctions.* Cold Spring Harb Perspect Biol, 2014. **6**(7): p. a016477.
32. Ame, J.C., C. Spenlehauer, and G. de Murcia, *The PARP superfamily.* Bioessays, 2004. **26**(8): p. 882-93.
33. Gibson, B.A. and W.L. Kraus, *New insights into the molecular and cellular functions of poly(ADP-ribose) and PARPs.* Nat Rev Mol Cell Biol, 2012. **13**(7): p. 411-24.
34. Boehler, C., et al., *Poly(ADP-ribose) polymerase 3 (PARP3), a newcomer in cellular response to DNA damage and mitotic progression.* Proc Natl Acad Sci U S A, 2011. **108**(7): p. 2783-8.
35. Rulten, S.L., et al., *PARP-3 and APLF function together to accelerate nonhomologous end-joining.* Mol Cell, 2011. **41**(1): p. 33-45.
36. Chambon, P., J.D. Weill, and P. Mandel, *Nicotinamide mononucleotide activation of new DNA-dependent polyadenylic acid synthesizing nuclear enzyme.* Biochem Biophys Res Commun, 1963. **11**: p. 39-43.
37. D'Amours, D., et al., *Poly(ADP-ribosyl)ation reactions in the regulation of nuclear functions.* Biochem J, 1999. **342 (Pt 2)**: p. 249-68.
38. Ray Chaudhuri, A., et al., *Replication fork stability confers chemoresistance in BRCA-deficient cells.* Nature, 2016. **535**(7612): p. 382-7.
39. Bai, P. and C. Canto, *The role of PARP-1 and PARP-2 enzymes in metabolic regulation and disease.* Cell Metab, 2012. **16**(3): p. 290-5.
40. Ray Chaudhuri, A. and A. Nussenzweig, *The multifaceted roles of PARP1 in DNA repair and chromatin remodelling.* Nat Rev Mol Cell Biol, 2017. **18**(10): p. 610-621.
41. Dias, M.P., et al., *Understanding and overcoming resistance to PARP inhibitors in cancer therapy.* Nature Reviews Clinical Oncology, 2021. **18**(12): p. 773-791.
42. Shall, S. and G. de Murcia, *Poly(ADP-ribose) polymerase-1: what have we learned from the deficient mouse model?* Mutat Res, 2000. **460**(1): p. 1-15.
43. Satoh, M.S. and T. Lindahl, *Role of poly(ADP-ribose) formation in DNA repair.* Nature, 1992. **356**(6367): p. 356-8.
44. Hottiger, M.O., *SnapShot: ADP-Ribosylation Signaling.* Mol Cell, 2015. **58**(6): p. 1134-1134.e1.
45. Davidovic, L., et al., *Importance of poly(ADP-ribose) glycohydrolase in the control of poly(ADP-ribose) metabolism.* Exp Cell Res, 2001. **268**(1): p. 7-13.
46. Haince, J.F., et al., *PARP1-dependent kinetics of recruitment of MRE11 and NBS1 proteins to multiple DNA damage sites.* J Biol Chem, 2008. **283**(2): p. 1197-208.
47. Li, M. and X. Yu, *Function of BRCA1 in the DNA damage response is mediated by ADP-ribosylation.* Cancer Cell, 2013. **23**(5): p. 693-704.

48. Schwertman, P., S. Bekker-Jensen, and N. Mailand, *Regulation of DNA double-strand break repair by ubiquitin and ubiquitin-like modifiers.* Nat Rev Mol Cell Biol, 2016. **17**(6): p. 379-94.
49. Ruscetti, T., et al., *Stimulation of the DNA-dependent protein kinase by poly(ADP-ribose) polymerase.* J Biol Chem, 1998. **273**(23): p. 14461-7.
50. Berti, M., et al., *Human RECQ1 promotes restart of replication forks reversed by DNA topoisomerase I inhibition.* Nat Struct Mol Biol, 2013. **20**(3): p. 347-54.
51. Bryant, H.E., et al., *PARP is activated at stalled forks to mediate Mre11-dependent replication restart and recombination.* EMBO J, 2009. **28**(17): p. 2601-15.
52. Ying, S., F.C. Hamdy, and T. Helleday, *Mre11-dependent degradation of stalled DNA replication forks is prevented by BRCA2 and PARP1.* Cancer Res, 2012. **72**(11): p. 2814-21.
53. Bryant, H.E., et al., *Specific killing of BRCA2-deficient tumours with inhibitors of poly(ADP-ribose) polymerase.* Nature, 2005. **434**(7035): p. 913-7.
54. Farmer, H., et al., *Targeting the DNA repair defect in BRCA mutant cells as a therapeutic strategy.* Nature, 2005. **434**(7035): p. 917-21.
55. Bridges, C.B., *The origin of variations in sexual and sex-limited characters.* The American Naturalist, 1922. **56**(642): p. 51-63.
56. Nijman, S.M., *Synthetic lethality: general principles, utility and detection using genetic screens in human cells.* FEBS Lett, 2011. **585**(1): p. 1-6.
57. Dobzhansky, T., *Genetics of natural populations; recombination and variability in populations of Drosophila pseudoobscura.* Genetics, 1946. **31**(3): p. 269-90.
58. Fong, P.C., et al., *Inhibition of poly(ADP-ribose) polymerase in tumors from BRCA mutation carriers.* N Engl J Med, 2009. **361**(2): p. 123-34.
59. Audeh, M.W., et al., *Oral poly(ADP-ribose) polymerase inhibitor olaparib in patients with BRCA1 or BRCA2 mutations and recurrent ovarian cancer: a proof-of-concept trial.* The Lancet, 2010. **376**(9737): p. 245-251.
60. Tutt, A., et al., *Oral poly(ADP-ribose) polymerase inhibitor olaparib in patients with BRCA1 or BRCA2 mutations and advanced breast cancer: a proof-of-concept trial.* Lancet, 2010. **376**(9737): p. 235-44.
61. Kaufman, B., et al., *Olaparib monotherapy in patients with advanced cancer and a germline BRCA1/2 mutation.* J Clin Oncol, 2015. **33**(3): p. 244-50.
62. Franzese, E., et al., *PARP inhibitors in ovarian cancer.* Cancer Treat Rev, 2019. **73**: p. 1-9.
63. Baxter, J.S., et al., *Resistance to DNA repair inhibitors in cancer.* Mol Oncol, 2022. **16**(21): p. 3811-3827.
64. Lloyd, R.L., et al., *Combined PARP and ATR inhibition potentiates genome instability and cell death in ATM-deficient cancer cells.* Oncogene, 2020. **39**(25): p. 4869-4883.
65. Shah, P.D., et al., *Combination ATR and PARP Inhibitor (CAPRI): A phase 2 study of ceralasertib plus olaparib in patients with recurrent, platinum-resistant epithelial ovarian cancer.* Gynecol Oncol, 2021. **163**(2): p. 246-253.
66. Do, K.T., et al., *Phase 1 Combination Study of the CHK1 Inhibitor Prexasertib and the PARP Inhibitor Olaparib in High-grade Serous Ovarian Cancer and Other Solid Tumors.* Clin Cancer Res, 2021. **27**(17): p. 4710-4716.
67. Westin, S.N., et al., *EFFORT: EFFicacy Of adavosertib in parp ResisTance: A randomized two-arm non-comparative phase II study of adavosertib with or without olaparib in women with PARP-resistant ovarian cancer.* Journal of Clinical Oncology, 2021. **39**(15_suppl): p. 5505-5505.
68. Fu, X., et al., *Mechanism of PARP inhibitor resistance and potential overcoming strategies.* Genes Dis, 2023. **11**(1): p. 306-320.

69. Zahradka, P. and K. Ebisuzaki, *A shuttle mechanism for DNA-protein interactions. The regulation of poly(ADP-ribose) polymerase.* Eur J Biochem, 1982. **127**(3): p. 579-85.
70. Murai, J. and Y. Pommier, *PARP Trapping Beyond Homologous Recombination and Platinum Sensitivity in Cancers.* Annual Review of Cancer Biology, Vol 3, 2019. **3**: p. 131-150.
71. Murai, J., et al., *Trapping of PARP1 and PARP2 by Clinical PARP Inhibitors.* Cancer Res, 2012. **72**(21): p. 5588-99.
72. Zandarashvili, L., et al., *Structural basis for allosteric PARP-1 retention on DNA breaks.* Science, 2020. **368**(6486).
73. Pommier, Y., M.J. O'Connor, and J. de Bono, *Laying a trap to kill cancer cells: PARP inhibitors and their mechanisms of action.* Sci Transl Med, 2016. **8**(362): p. 362ps17.
74. Francica, P. and S. Rottenberg, *Mechanisms of PARP inhibitor resistance in cancer and insights into the DNA damage response.* Genome Med, 2018. **10**(1): p. 101.
75. Noordermeer, S.M. and H. van Attikum, *PARP Inhibitor Resistance: A Tug-of-War in BRCA-Mutated Cells.* Trends Cell Biol, 2019. **29**(10): p. 820-834.
76. Sakai, W., et al., *Secondary mutations as a mechanism of cisplatin resistance in BRCA2-mutated cancers.* Nature, 2008. **451**(7182): p. 1116-20.
77. Edwards, S.L., et al., *Resistance to therapy caused by intragenic deletion in BRCA2.* Nature, 2008. **451**(7182): p. 1111-5.
78. Pettitt, S.J., et al., *Clinical BRCA1/2 Reversion Analysis Identifies Hotspot Mutations and Predicted Neoantigens Associated with Therapy Resistance.* Cancer Discov, 2020. **10**(10): p. 1475-1488.
79. Barber, L.J., et al., *Secondary mutations in BRCA2 associated with clinical resistance to a PARP inhibitor.* J Pathol, 2013. **229**(3): p. 422-9.
80. Domchek, S.M., *Reversion Mutations with Clinical Use of PARP Inhibitors: Many Genes, Many Versions.* Cancer Discov, 2017. **7**(9): p. 937-939.
81. Kondrashova, O., et al., *Secondary Somatic Mutations Restoring RAD51C and RAD51D Associated with Acquired Resistance to the PARP Inhibitor Rucaparib in High-Grade Ovarian Carcinoma.* Cancer Discov, 2017. **7**(9): p. 984-998.
82. Lin, K.K., et al., *BRCA Reversion Mutations in Circulating Tumor DNA Predict Primary and Acquired Resistance to the PARP Inhibitor Rucaparib in High-Grade Ovarian Carcinoma.* Cancer Discov, 2019. **9**(2): p. 210-219.
83. Weigelt, B., et al., *Diverse BRCA1 and BRCA2 Reversion Mutations in Circulating Cell-Free DNA of Therapy-Resistant Breast or Ovarian Cancer.* Clin Cancer Res, 2017. **23**(21): p. 6708-6720.
84. Norquist, B., et al., *Secondary Somatic Mutations Restoring BRCA1/2 Predict Chemotherapy Resistance in Hereditary Ovarian Carcinomas.* Journal of Clinical Oncology, 2011. **29**(22): p. 3008-3015.
85. Afghahi, A., et al., *Tumor BRCA1 Reversion Mutation Arising during Neoadjuvant Platinum-Based Chemotherapy in Triple-Negative Breast Cancer Is Associated with Therapy Resistance.* Clin Cancer Res, 2017. **23**(13): p. 3365-3370.
86. Pishvaian, M.J., et al., *BRCA2 secondary mutation-mediated resistance to platinum and PARP inhibitor-based therapy in pancreatic cancer.* Br J Cancer, 2017. **116**(8): p. 1021-1026.
87. Quigley, D., et al., *Analysis of Circulating Cell-Free DNA Identifies Multiclonal Heterogeneity of BRCA2 Reversion Mutations Associated with Resistance to PARP Inhibitors.* Cancer Discov, 2017. **7**(9): p. 999-1005.
88. Goodall, J., et al., *Circulating Cell-Free DNA to Guide Prostate Cancer Treatment with PARP Inhibition.* Cancer Discov, 2017. **7**(9): p. 1006-1017.

89. Bouwman, P., et al., *53BP1 loss rescues BRCA1 deficiency and is associated with triple-negative and BRCA-mutated breast cancers.* Nat Struct Mol Biol, 2010. **17**(6): p. 688-95.
90. Bunting, S.F., et al., *53BP1 inhibits homologous recombination in Brca1-deficient cells by blocking resection of DNA breaks.* Cell, 2010. **141**(2): p. 243-54.
91. Jaspers, J.E., et al., *Loss of 53BP1 causes PARP inhibitor resistance in Brca1-mutated mouse mammary tumors.* Cancer Discov, 2013. **3**(1): p. 68-81.
92. Feng, L., et al., *Cell cycle-dependent inhibition of 53BP1 signaling by BRCA1.* Cell Discov, 2015. **1**: p. 15019.
93. Chapman, J.R., et al., *RIF1 is essential for 53BP1-dependent nonhomologous end joining and suppression of DNA double-strand break resection.* Mol Cell, 2013. **49**(5): p. 858-71.
94. Noordermeer, S.M., et al., *The shieldin complex mediates 53BP1-dependent DNA repair.* Nature, 2018. **560**(7716): p. 117-121.
95. He, Y.J., et al., *DYNLL1 binds to MRE11 to limit DNA end resection in BRCA1-deficient cells.* Nature, 2018. **563**(7732): p. 522-526.
96. Clairmont, C.S., et al., *TRIP13 regulates DNA repair pathway choice through REV7 conformational change.* Nat Cell Biol, 2020. **22**(1): p. 87-96.
97. Choi, Y.E., et al., *Platinum and PARP Inhibitor Resistance Due to Overexpression of MicroRNA-622 in BRCA1-Mutant Ovarian Cancer.* Cell Rep, 2016. **14**(3): p. 429-439.
98. Vaidyanathan, A., et al., *ABCB1 (MDR1) induction defines a common resistance mechanism in paclitaxel- and olaparib-resistant ovarian cancer cells.* Br J Cancer, 2016. **115**(4): p. 431-41.
99. Rottenberg, S., et al., *High sensitivity of BRCA1-deficient mammary tumors to the PARP inhibitor AZD2281 alone and in combination with platinum drugs.* Proc Natl Acad Sci U S A, 2008. **105**(44): p. 17079-84.
100. Szakacs, G., et al., *Targeting the Achilles heel of multidrug-resistant cancer by exploiting the fitness cost of resistance.* Chem Rev, 2014. **114**(11): p. 5753-74.
101. Szakacs, G., et al., *Targeting multidrug resistance in cancer.* Nat Rev Drug Discov, 2006. **5**(3): p. 219-34.
102. Cripe, L.D., et al., *Zosuquidar, a novel modulator of P-glycoprotein, does not improve the outcome of older patients with newly diagnosed acute myeloid leukemia: a randomized, placebo-controlled trial of the Eastern Cooperative Oncology Group 3999.* Blood, 2010. **116**(20): p. 4077-85.
103. Ruff, P., et al., *A randomized, placebo-controlled, double-blind phase 2 study of docetaxel compared to docetaxel plus zosuquidar (LY335979) in women with metastatic or locally recurrent breast cancer who have received one prior chemotherapy regimen.* Cancer Chemother Pharmacol, 2009. **64**(4): p. 763-8.
104. Xiong, Y., et al., *Pamiparib is a potent and selective PARP inhibitor with unique potential for the treatment of brain tumor.* Neoplasia, 2020. **22**(9): p. 431-440.
105. Lickliter, J.D., et al., *Phase 1A/1B dose-escalation and -expansion study to evaluate the safety, pharmacokinetics, food effects and antitumor activity of pamiparib in advanced solid tumours.* Br J Cancer, 2022. **126**(4): p. 576-585.
106. Rouleau, M., et al., *PARP inhibition: PARP1 and beyond.* Nat Rev Cancer, 2010. **10**(4): p. 293-301.
107. Pettitt, S.J., et al., *Genome-wide and high-density CRISPR-Cas9 screens identify point mutations in PARP1 causing PARP inhibitor resistance.* Nat Commun, 2018. **9**(1): p. 1849.
108. Gogola, E., et al., *Selective Loss of PARG Restores PARylation and Counteracts PARP Inhibitor-Mediated Synthetic Lethality.* Cancer Cell, 2018. **33**(6): p. 1078-1093 e12.

109. Guillemette, S., et al., *Resistance to therapy in BRCA2 mutant cells due to loss of the nucleosome remodeling factor CHD4.* Genes Dev, 2015. **29**(5): p. 489-94.
110. Taglialatela, A., et al., *Restoration of Replication Fork Stability in BRCA1- and BRCA2-Deficient Cells by Inactivation of SNF2-Family Fork Remodelers.* Mol Cell, 2017. **68**(2): p. 414-430 e8.
111. Luijsterburg, M.S., et al., *A PALB2-interacting domain in RNF168 couples homologous recombination to DNA break-induced chromatin ubiquitylation.* Elife, 2017. **6**.
112. Zong, D., et al., *BRCA1 Haploinsufficiency Is Masked by RNF168-Mediated Chromatin Ubiquitylation.* Mol Cell, 2019. **73**(6): p. 1267-1281 e7.
113. Nakada, S., R.M. Yonamine, and K. Matsuo, *RNF8 regulates assembly of RAD51 at DNA double-strand breaks in the absence of BRCA1 and 53BP1.* Cancer Res, 2012. **72**(19): p. 4974-83.
114. Belotserkovskaya, R., et al., *PALB2 chromatin recruitment restores homologous recombination in BRCA1-deficient cells depleted of 53BP1.* Nat Commun, 2020. **11**(1): p. 819.
115. Feng, Z., et al., *Rad52 inactivation is synthetically lethal with BRCA2 deficiency.* Proc Natl Acad Sci U S A, 2011. **108**(2): p. 686-91.
116. Lok, B.H., et al., *RAD52 inactivation is synthetically lethal with deficiencies in BRCA1 and PALB2 in addition to BRCA2 through RAD51-mediated homologous recombination.* Oncogene, 2013. **32**(30): p. 3552-8.
117. Malacaria, E., et al., *Rad52 prevents excessive replication fork reversal and protects from nascent strand degradation.* Nat Commun, 2019. **10**(1): p. 1412.
118. Sullivan-Reed, K., et al., *Simultaneous Targeting of PARP1 and RAD52 Triggers Dual Synthetic Lethality in BRCA-Deficient Tumor Cells.* Cell Rep, 2018. **23**(11): p. 3127-3136.
119. Karakashev, S., et al., *BET Bromodomain Inhibition Synergizes with PARP Inhibitor in Epithelial Ovarian Cancer.* Cell Rep, 2017. **21**(12): p. 3398-3405.
120. Yang, L., et al., *Repression of BET activity sensitizes homologous recombination-proficient cancers to PARP inhibition.* Sci Transl Med, 2017. **9**(400).
121. Li, L., et al., *Androgen receptor inhibitor-induced "BRCAness" and PARP inhibition are synthetically lethal for castration-resistant prostate cancer.* Sci Signal, 2017. **10**(480).
122. Pilie, P.G., et al., *State-of-the-art strategies for targeting the DNA damage response in cancer.* Nat Rev Clin Oncol, 2019. **16**(2): p. 81-104.
123. Ray-Coquard, I., et al., *Olaparib plus bevacizumab first-line maintenance in ovarian cancer: final overall survival results from the PAOLA-1/ENGOT-ov25 trial.* Ann Oncol, 2023. **34**(8): p. 681-692.
124. Mirza, M.R., et al., *Niraparib plus bevacizumab versus niraparib alone for platinum-sensitive recurrent ovarian cancer (NSGO-AVANOVA2/ENGOT-ov24): a randomised, phase 2, superiority trial.* Lancet Oncol, 2019. **20**(10): p. 1409-1419.
125. Matthews, H.K., C. Bertoli, and R.A.M. de Bruin, *Cell cycle control in cancer.* Nat Rev Mol Cell Biol, 2022. **23**(1): p. 74-88.
126. Lobrich, M. and P.A. Jeggo, *The impact of a negligent G2/M checkpoint on genomic instability and cancer induction.* Nat Rev Cancer, 2007. **7**(11): p. 861-9.
127. Yazinski, S.A., et al., *ATR inhibition disrupts rewired homologous recombination and fork protection pathways in PARP inhibitor-resistant BRCA-deficient cancer cells.* Genes Dev, 2017. **31**(3): p. 318-332.
128. Kim, H., et al., *Combining PARP with ATR inhibition overcomes PARP inhibitor and platinum resistance in ovarian cancer models.* Nat Commun, 2020. **11**(1): p. 3726.
129. Murai, J., et al., *Resistance to PARP inhibitors by SLFN11 inactivation can be overcome by ATR inhibition.* Oncotarget, 2016. **7**(47): p. 76534-76550.

130. D'Andrea, A.D., *Mechanisms of PARP inhibitor sensitivity and resistance.* DNA Repair (Amst), 2018. **71**: p. 172-176.
131. Senichkin, V.V., et al., *Simple and Efficient Protocol for Subcellular Fractionation of Normal and Apoptotic Cells.* Cells, 2021. **10**(4).
132. Conant, D., et al., *Inference of CRISPR Edits from Sanger Trace Data.* CRISPR J, 2022. **5**(1): p. 123-130.
133. Kleinheinz, K., et al., *ACEseq – allele specific copy number estimation from whole genome sequencing.* bioRxiv, 2017: p. 210807.
134. Talevich, E., et al., *CNVkit: Genome-Wide Copy Number Detection and Visualization from Targeted DNA Sequencing.* PLoS Comput Biol, 2016. **12**(4): p. e1004873.
135. Consortium, I.T.P.-C.A.o.W.G., *Pan-cancer analysis of whole genomes.* Nature, 2020. **578**(7793): p. 82-93.
136. Dobin, A., et al., *STAR: ultrafast universal RNA-seq aligner.* Bioinformatics, 2013. **29**(1): p. 15-21.
137. Love, M.I., W. Huber, and S. Anders, *Moderated estimation of fold change and dispersion for RNA-seq data with DESeq2.* Genome Biol, 2014. **15**(12): p. 550.
138. Wagner, S., *Identification of Tumor Initiating Cells in a Patient-Matched Model of Serous Ovarian Carcinoma.* 2013.
139. Jabs, J., et al., *Screening drug effects in patient-derived cancer cells links organoid responses to genome alterations.* Mol Syst Biol, 2017. **13**(11): p. 955.
140. Jamieson, E.R. and S.J. Lippard, *Structure, Recognition, and Processing of Cisplatin-DNA Adducts.* Chem Rev, 1999. **99**(9): p. 2467-98.
141. Bhatlekar, S., J.Z. Fields, and B.M. Boman, *HOX genes and their role in the development of human cancers.* J Mol Med (Berl), 2014. **92**(8): p. 811-23.
142. Xiang, Q., et al., *The Correlation between PSCA Expression and Neuroendocrine Differentiation in Prostate Cancer.* Biomed Res Int, 2020. **2020**: p. 5395312.
143. Michel, T. and P.M. Vanhoutte, *Cellular signaling and NO production.* Pflugers Arch, 2010. **459**(6): p. 807-16.
144. Paul, M., et al., *Nitric-Oxide Synthase trafficking inducer (NOSTRIN) is an emerging negative regulator of colon cancer progression.* BMC Cancer, 2022. **22**(1): p. 594.
145. Waks, A.G., et al., *Reversion and non-reversion mechanisms of resistance to PARP inhibitor or platinum chemotherapy in BRCA1/2-mutant metastatic breast cancer.* Ann Oncol, 2020. **31**(5): p. 590-598.
146. Paes Dias, M., et al., *Loss of nuclear DNA ligase III reverts PARP inhibitor resistance in BRCA1/53BP1 double-deficient cells by exposing ssDNA gaps.* Mol Cell, 2021. **81**(22): p. 4692-4708 e9.
147. Was, H., et al., *Polyploidy formation in cancer cells: How a Trojan horse is born.* Semin Cancer Biol, 2022. **81**: p. 24-36.
148. Zheng, L., et al., *Polyploid cells rewire DNA damage response networks to overcome replication stress-induced barriers for tumour progression.* Nat Commun, 2012. **3**: p. 815.
149. Wang, Z., et al., *Olaparib induced senescence under P16 or P53 dependent manner in ovarian cancer.* J Gynecol Oncol, 2019. **30**(2): p. e26.
150. Efimova, E.V., et al., *Poly(ADP-ribose) polymerase inhibitor induces accelerated senescence in irradiated breast cancer cells and tumors.* Cancer Res, 2010. **70**(15): p. 6277-82.
151. Fleury, H., et al., *Exploiting interconnected synthetic lethal interactions between PARP inhibition and cancer cell reversible senescence.* Nat Commun, 2019. **10**(1): p. 2556.
152. Collins, A., et al., *Measuring DNA modifications with the comet assay: a compendium of protocols.* Nat Protoc, 2023.

153. Hodgson, D.R., et al., *Candidate biomarkers of PARP inhibitor sensitivity in ovarian cancer beyond the BRCA genes.* Br J Cancer, 2018. **119**(11): p. 1401-1409.
154. Lord, C.J. and A. Ashworth, *BRCAness revisited.* Nat Rev Cancer, 2016. **16**(2): p. 110-20.
155. Jonsson, P., et al., *Tumour lineage shapes BRCA-mediated phenotypes.* Nature, 2019. **571**(7766): p. 576-579.
156. Graeser, M., et al., *A marker of homologous recombination predicts pathologic complete response to neoadjuvant chemotherapy in primary breast cancer.* Clin Cancer Res, 2010. **16**(24): p. 6159-68.
157. Certo, M.T., et al., *Tracking genome engineering outcome at individual DNA breakpoints.* Nat Methods, 2011. **8**(8): p. 671-6.
158. Sauriol, A., et al., *Inhibition of nicotinamide dinucleotide salvage pathway counters acquired and intrinsic poly(ADP-ribose) polymerase inhibitor resistance in high-grade serous ovarian cancer.* Sci Rep, 2023. **13**(1): p. 3334.
159. Bajrami, I., et al., *Synthetic lethality of PARP and NAMPT inhibition in triple-negative breast cancer cells.* EMBO Mol Med, 2012. **4**(10): p. 1087-96.
160. Riches, L.C., et al., *Pharmacology of the ATM Inhibitor AZD0156: Potentiation of Irradiation and Olaparib Responses Preclinically.* Mol Cancer Ther, 2020. **19**(1): p. 13-25.
161. Yi, Y.W., et al., *Co-treatment with BEZ235 Enhances Sensitivity of BRCA1-negative Breast Cancer Cells to Olaparib.* Anticancer Res, 2015. **35**(7): p. 3829-38.
162. Ianevski, A., A.K. Giri, and T. Aittokallio, *SynergyFinder 3.0: an interactive analysis and consensus interpretation of multi-drug synergies across multiple samples.* Nucleic Acids Res, 2022. **50**(W1): p. W739-W743.
163. Clements, K.E., et al., *Identification of regulators of poly-ADP-ribose polymerase inhibitor response through complementary CRISPR knockout and activation screens.* Nat Commun, 2020. **11**(1): p. 6118.
164. Johnson, N., et al., *Stabilization of mutant BRCA1 protein confers PARP inhibitor and platinum resistance.* Proc Natl Acad Sci U S A, 2013. **110**(42): p. 17041-6.
165. Baker, M., *Reproducibility: Respect your cells!* Nature, 2016. **537**(7620): p. 433-5.
166. Lee, J., et al., *Tumor stem cells derived from glioblastomas cultured in bFGF and EGF more closely mirror the phenotype and genotype of primary tumors than do serum-cultured cell lines.* Cancer Cell, 2006. **9**(5): p. 391-403.
167. Domcke, S., et al., *Evaluating cell lines as tumour models by comparison of genomic profiles.* Nat Commun, 2013. **4**: p. 2126.
168. Deer, E.L., et al., *Phenotype and genotype of pancreatic cancer cell lines.* Pancreas, 2010. **39**(4): p. 425-35.
169. Ledermann, J., et al., *Olaparib maintenance therapy in patients with platinum-sensitive relapsed serous ovarian cancer: a preplanned retrospective analysis of outcomes by BRCA status in a randomised phase 2 trial.* Lancet Oncol, 2014. **15**(8): p. 852-61.
170. Rigakos, G. and E. Razis, *BRCAness: finding the Achilles heel in ovarian cancer.* Oncologist, 2012. **17**(7): p. 956-62.
171. Turner, N., A. Tutt, and A. Ashworth, *Hallmarks of 'BRCAness' in sporadic cancers.* Nat Rev Cancer, 2004. **4**(10): p. 814-9.
172. Helleday, T., *The underlying mechanism for the PARP and BRCA synthetic lethality: clearing up the misunderstandings.* Mol Oncol, 2011. **5**(4): p. 387-93.
173. Davies, H., et al., *HRDetect is a predictor of BRCA1 and BRCA2 deficiency based on mutational signatures.* Nat Med, 2017. **23**(4): p. 517-525.
174. Watkins, J.A., et al., *Genomic scars as biomarkers of homologous recombination deficiency and drug response in breast and ovarian cancers.* Breast Cancer Res, 2014. **16**(3): p. 211.

175. Patch, A.M., et al., *Whole-genome characterization of chemoresistant ovarian cancer.* Nature, 2015. **521**(7553): p. 489-94.
176. Brenner, J.C., et al., *Mechanistic rationale for inhibition of poly(ADP-ribose) polymerase in ETS gene fusion-positive prostate cancer.* Cancer Cell, 2011. **19**(5): p. 664-78.
177. Brenner, J.C., et al., *PARP-1 inhibition as a targeted strategy to treat Ewing's sarcoma.* Cancer Res, 2012. **72**(7): p. 1608-13.
178. Shen, W.H., et al., *Essential role for nuclear PTEN in maintaining chromosomal integrity.* Cell, 2007. **128**(1): p. 157-70.
179. Sun, Z., et al., *PTEN C-terminal deletion causes genomic instability and tumor development.* Cell Rep, 2014. **6**(5): p. 844-54.
180. Fedier, A., et al., *Exposure to escalating olaparib does not induce acquired resistance to PARPi and to other chemotherapeutic compounds in ovarian cancer cell lines.* Int J Oncol, 2022. **61**(1).
181. Chaudhary, P.M. and I.B. Roninson, *Induction of multidrug resistance in human cells by transient exposure to different chemotherapeutic drugs.* J Natl Cancer Inst, 1993. **85**(8): p. 632-9.
182. Sun, C., et al., *Reversible and adaptive resistance to BRAF(V600E) inhibition in melanoma.* Nature, 2014. **508**(7494): p. 118-22.
183. Antolin, A.A., et al., *The kinase polypharmacology landscape of clinical PARP inhibitors.* Sci Rep, 2020. **10**(1): p. 2585.
184. You, B., et al., *Low probability of disease cure in advanced ovarian carcinomas before the PARP inhibitor era.* Br J Cancer, 2022. **127**(1): p. 79-83.
185. Lisio, M.A., et al., *High-Grade Serous Ovarian Cancer: Basic Sciences, Clinical and Therapeutic Standpoints.* Int J Mol Sci, 2019. **20**(4).
186. Ehrsson, H., I. Wallin, and J. Yachnin, *Pharmacokinetics of oxaliplatin in humans.* Med Oncol, 2002. **19**(4): p. 261-5.
187. Graham, J., M. Mushin, and P. Kirkpatrick, *Oxaliplatin.* Nat Rev Drug Discov, 2004. **3**(1): p. 11-2.
188. Di Francesco, A.M., A. Ruggiero, and R. Riccardi, *Cellular and molecular aspects of drugs of the future: oxaliplatin.* Cell Mol Life Sci, 2002. **59**(11): p. 1914-27.
189. Kelland, L., *The resurgence of platinum-based cancer chemotherapy.* Nat Rev Cancer, 2007. **7**(8): p. 573-84.
190. Chu, G., *Cellular responses to cisplatin. The roles of DNA-binding proteins and DNA repair.* J Biol Chem, 1994. **269**(2): p. 787-90.
191. Nikolova, T., et al., *Homologous recombination protects mammalian cells from replication-associated DNA double-strand breaks arising in response to methyl methanesulfonate.* DNA Repair (Amst), 2010. **9**(10): p. 1050-63.
192. Sehouli, J. and G. Oskay-Ozcelik, *Use of paclitaxel for advanced ovarian cancer in clinical practice: analysis of 541 patients. Results from a German multi-centre observational study.* Anticancer Res, 2010. **30**(10): p. 4245-50.
193. Von Hoff, D.D., et al., *Increased survival in pancreatic cancer with nab-paclitaxel plus gemcitabine.* N Engl J Med, 2013. **369**(18): p. 1691-703.
194. Stage, T.B., T.K. Bergmann, and D.L. Kroetz, *Clinical Pharmacokinetics of Paclitaxel Monotherapy: An Updated Literature Review.* Clin Pharmacokinet, 2018. **57**(1): p. 7-19.
195. Borrego-Soto, G., R. Ortiz-Lopez, and A. Rojas-Martinez, *Ionizing radiation-induced DNA injury and damage detection in patients with breast cancer.* Genet Mol Biol, 2015. **38**(4): p. 420-32.

196. Gogola, E., S. Rottenberg, and J. Jonkers, *Resistance to PARP Inhibitors: Lessons from Preclinical Models of BRCA-Associated Cancer.* Annual Review of Cancer Biology, 2019. **3**(1): p. 235-254.
197. Becker, J.R., et al., *The ASCIZ-DYNLL1 axis promotes 53BP1-dependent non-homologous end joining and PARP inhibitor sensitivity.* Nat Commun, 2018. **9**(1): p. 5406.
198. Wang, H., et al., *Discovery of Pamiparib (BGB-290), a Potent and Selective Poly (ADP-ribose) Polymerase (PARP) Inhibitor in Clinical Development.* J Med Chem, 2020. **63**(24): p. 15541-15563.
199. Fenton, A.L., et al., *The PARP3- and ATM-dependent phosphorylation of APLF facilitates DNA double-strand break repair.* Nucleic Acids Res, 2013. **41**(7): p. 4080-92.
200. Dong, W., et al., *End Processing Factor APLF Promotes NHEJ Efficiency and Contributes to TMZ- and Ionizing Radiation-Resistance in Glioblastoma Cells.* Onco Targets Ther, 2020. **13**: p. 10593-10605.
201. Yang, J., et al., *Twist, a master regulator of morphogenesis, plays an essential role in tumor metastasis.* Cell, 2004. **117**(7): p. 927-39.
202. Roberts, C.M., et al., *TWIST1 drives cisplatin resistance and cell survival in an ovarian cancer model, via upregulation of GAS6, L1CAM, and Akt signalling.* Sci Rep, 2016. **6**: p. 37652.
203. Zheng, F., et al., *Mechanism and current progress of Poly ADP-ribose polymerase (PARP) inhibitors in the treatment of ovarian cancer.* Biomed Pharmacother, 2020. **123**: p. 109661.
204. Guillon, J., et al., *Chemotherapy-induced senescence, an adaptive mechanism driving resistance and tumor heterogeneity.* Cell Cycle, 2019. **18**(19): p. 2385-2397.
205. Wang, L., L. Lankhorst, and R. Bernards, *Exploiting senescence for the treatment of cancer.* Nat Rev Cancer, 2022. **22**(6): p. 340-355.
206. Inbar-Rozensal, D., et al., *A selective eradication of human nonhereditary breast cancer cells by phenanthridine-derived polyADP-ribose polymerase inhibitors.* Breast Cancer Res, 2009. **11**(6): p. R78.
207. Warburg, O., *über den Stoffwechsel der Carcinomzelle.* Klinische Wochenschrift, 1925. **4**(12): p. 534-536.
208. Zheng, J., *Energy metabolism of cancer: Glycolysis versus oxidative phosphorylation (Review).* Oncol Lett, 2012. **4**(6): p. 1151-1157.
209. Bosc, C., M.A. Selak, and J.E. Sarry, *Resistance Is Futile: Targeting Mitochondrial Energetics and Metabolism to Overcome Drug Resistance in Cancer Treatment.* Cell Metab, 2017. **26**(5): p. 705-707.
210. Kumar, P.R., et al., *Mitochondrial oxidative phosphorylation in cutaneous melanoma.* Br J Cancer, 2021. **124**(1): p. 115-123.
211. Sica, V., et al., *Oxidative phosphorylation as a potential therapeutic target for cancer therapy.* Int J Cancer, 2020. **146**(1): p. 10-17.
212. Kuntz, E.M., et al., *Targeting mitochondrial oxidative phosphorylation eradicates therapy-resistant chronic myeloid leukemia stem cells.* Nat Med, 2017. **23**(10): p. 1234-1240.
213. Machado, N.D., et al., *Targeting mitochondrial oxidative phosphorylation: lessons, advantages, and opportunities.* Br J Cancer, 2023. **129**(6): p. 897-899.
214. Srivastava, S., *Emerging therapeutic roles for NAD(+) metabolism in mitochondrial and age-related disorders.* Clin Transl Med, 2016. **5**(1): p. 25.
215. Kennedy, B.E., et al., *NAD(+) salvage pathway in cancer metabolism and therapy.* Pharmacol Res, 2016. **114**: p. 274-283.

216. Xie, N., et al., *NAD(+) metabolism: pathophysiologic mechanisms and therapeutic potential.* Signal Transduct Target Ther, 2020. **5**(1): p. 227.
217. Gupte, R., Z. Liu, and W.L. Kraus, *PARPs and ADP-ribosylation: recent advances linking molecular functions to biological outcomes.* Genes Dev, 2017. **31**(2): p. 101-126.
218. Demeny, M.A. and L. Virag, *The PARP Enzyme Family and the Hallmarks of Cancer Part 1. Cell Intrinsic Hallmarks.* Cancers (Basel), 2021. **13**(9).
219. Nahimana, A., et al., *The NAD biosynthesis inhibitor APO866 has potent antitumor activity against hematologic malignancies.* Blood, 2009. **113**(14): p. 3276-86.
220. Hassa, P.O., et al., *Transcriptional coactivation of nuclear factor-kappaB-dependent gene expression by p300 is regulated by poly(ADP)-ribose polymerase-1.* J Biol Chem, 2003. **278**(46): p. 45145-53.
221. Krishnakumar, R., et al., *Reciprocal binding of PARP-1 and histone H1 at promoters specifies transcriptional outcomes.* Science, 2008. **319**(5864): p. 819-21.
222. Aravind, L., *The WWE domain: a common interaction module in protein ubiquitination and ADP ribosylation.* Trends Biochem Sci, 2001. **26**(5): p. 273-5.
223. Mann, M., et al., *PARP-1 inhibitor modulate beta-catenin signaling to enhance cisplatin sensitivity in cancer cervix.* Oncotarget, 2019. **10**(42): p. 4262-4275.
224. Nakagawa, Y., et al., *NF-kappaB signaling mediates acquired resistance after PARP inhibition.* Oncotarget, 2015. **6**(6): p. 3825-39.
225. Leung, A.K., et al., *Poly(ADP-ribose) regulates stress responses and microRNA activity in the cytoplasm.* Mol Cell, 2011. **42**(4): p. 489-99.
226. Mirza, M.R., et al., *Niraparib Maintenance Therapy in Platinum-Sensitive, Recurrent Ovarian Cancer.* N Engl J Med, 2016. **375**(22): p. 2154-2164.
227. Kim, D.S., C.V. Camacho, and W.L. Kraus, *Alternate therapeutic pathways for PARP inhibitors and potential mechanisms of resistance.* Exp Mol Med, 2021. **53**(1): p. 42-51.
228. Lheureux, S., et al., *Long-Term Responders on Olaparib Maintenance in High-Grade Serous Ovarian Cancer: Clinical and Molecular Characterization.* Clin Cancer Res, 2017. **23**(15): p. 4086-4094.
229. Michael, M. and M.M. Doherty, *Drug metabolism by tumours: its nature, relevance and therapeutic implications.* Expert Opin Drug Metab Toxicol, 2007. **3**(6): p. 783-803.
230. Noll, E.M., et al., *CYP3A5 mediates basal and acquired therapy resistance in different subtypes of pancreatic ductal adenocarcinoma.* Nat Med, 2016. **22**(3): p. 278-87.
231. Bruin, M.A.C., et al., *Pharmacokinetics and Pharmacodynamics of PARP Inhibitors in Oncology.* Clin Pharmacokinet, 2022. **61**(12): p. 1649-1675.
232. Fernandez-Mateos, J., et al., *Epigenetic heritability of cell plasticity drives cancer drug resistance through one-to-many genotype to phenotype mapping.* bioRxiv, 2023: p. 2023.11.15.567140.

8. Contributions

The following people contributed to the work presented in this dissertation:

This doctoral thesis was conducted under the supervision of Prof. Dr. Andreas Trumpp and Dr. Martin Sprick. The project was conceived collaboratively by myself and Dr. Martin Sprick. The patient-derived cell lines used in the study were established by Dr. Steve Wagner. Dr. Sarah-Jane Neuberth and I conducted Seahorse Mito Stress metabolic measurements, and I would like to express gratitude to Dr. Guoliang Cui for providing the Agilent Seahorse XFe 96 machine at DKFZ Heidelberg. Additionally, Dr. Ali Bakr from the Plass group at DKFZ support me with the Comet assay, and Rad51 γH2A.X staining and analysis. M-FISH experiments were conducted in collaboration with Prof. Anna Jauch from the university clinic Heidelberg.

In the initial stages of the project, Dr. Franzisak Zickgraf provided invaluable guidance, introducing me to OC cell lines and various cell culture techniques. Special thanks to Dr. Aino Maija Leppä and Manuel Mastel for their essential support in analysis of my RNA-seq data, especially Aino Maija Leppä offering significant assistance with R-related queries. I am also grateful to Paul Schwerd Kleine for his support in analyzing WGS data. Technical support for experiments was provided by Dr. Andreas Narr and Dr. Vera Thiel.

I would like to extend my appreciation to all technicians of HI-STEM, especially Corinna Klein, Vanessa Vogel, and Ornella Kossi of the METICS group, for their technical assistance. Acknowledgments go to Steffen Schmitt, Marcus Eich, Klaus Hexel, Tobias Rubner, and Florian Blum from the DKFZ Flow Cytometry Core Facility for their assistance. Special thanks to the DKFZ Genomics and Proteomics Core Facility and the DKFZ ODCF System Administration for their support.

At the end I would like to express special thank you to Dr Aino Maija Leppä and Dr. Vera Thiel for proofreading this doctoral thesis.

9. Acknowledgements

The past five years have been a rollercoaster ride of highs and lows, and these highs wouldn't have been possible without the many fantastic people I met during my time at HI-STEM and the dkfz. When I started on my PhD journey in 2018, I was uncertain about the challenges that come with it. Now, I understand the thrill of discovering new and fascinating results and the disappointment when experiments don't go as planned. I vividly recall the advice of my Bachelor thesis supervisor, who once said, "90 % of the experiments end up in the bin, and only 10 % actually work." Until I began my PhD, I thought it was just a cliché.
Importantly, the work presented in this thesis and the memorable experiences as a PhD student would not have been possible without the support of wonderful people who joined me on this rollercoaster ride.

Firstly, I want to express my gratitude to Dr. Martin Sprick. I appreciate that you selected me; otherwise, I would have missed the rollercoaster ride of my life. Thank you for your support throughout my PhD. Your door was always open for me, and you were willing to discuss any questions I had regarding my project. I truly admire your technical and scientific expertise, especially when we tackled new methods or faced challenges during my project. Your guidance supported my development as a scientist, and you enhanced my awareness of critical thinking. I am particularly thankful for your warm and supportive words during the time when I contemplated giving up on my PhD. Thank you for the great time I had in the METICS group.

I am grateful to my Ph.D. supervisor, Prof. Dr. Andreas Trumpp, for providing me with the wonderful opportunity to pursue my PhD in your laboratory. You created an atmosphere where everyone could develop their projects with nearly endless opportunities. I appreciated the chances you gave me to present my research at international conferences and grow into who I am now. Lastly, thank you for organizing the annual Christmas party at your place, which was always a highlight.

Moreover, I would like to thank Prof. Dr. Benedikt Brors for being a member of my thesis advisory committee and serving as the second examiner for my dissertation. I value your support and input during my Ph.D., especially our discussions about the formal details of writing a thesis at Heidelberg University.

Thank you, Prof. Dr. Ingrid Lohmann and Prof. Dr. Peter Angel, for being members of my defense committee. I am very grateful for your interest in my work and the time you took to evaluate this thesis.

I want to thank my thesis advisory committee member, Prof. Dr. Frederik Marmé, for supporting me scientifically and encouraging me to believe that my work is meaningful.

I would also like to thank Dr. Ali Bakr for his contribution, expertise, and time supporting me in my experiments regarding DNA damage assays; I truly enjoyed working with you.

As mentioned, my PhD life would not have been what it was without my fellow students, who accompanied me on my rollercoaster ride. Starting with the present and past members of our 11:30 Lunch-crew and Milk Club: Aino-Maija Leppä, Andreas Narr, Vera Thiel, Manuel Mastel, Tim Vorberg, Paul-Schwerd-Kleine, Tasneem Cheytan, Karolin Stumpf, Frank Yi-Tao Huang, Nikolai Schleußner, Sarah Jane Neuberth, Carolin Andresen, Franziska Zickgraf, Andrea Geist, Felix Geist, Manuel Reitberger, and Pia Sommerkamp. I thank them for the fun we had during lunch breaks, the support they provided, and the adventures outside the lab. I would also like to express my gratitude to all members of the METICS group: Roberto Würth, Jennifer Wischhusen, Vera Thiel, Paul Schwerd-Kleine, Tasneem Cheytan, Tim Vorberg, Corinna Klein, Vanessa Vogel, Jennifer Lewis, and Dominique Schulz. Thank you for your support, scientific advice, critical feedback, motivation, and kind words after my presentations.

Thanks to all the members of BioContact, which was my second home in Heidelberg next to the lab, especially Adela, Alex, Denise, Melli, Michelle, and Jasmin.

A special thanks goes to Maija, Andi, Vera, Shubhankar, and Manu for all the amazing moments we had together in the past years, which I will never forget. Maija, for joining me for TRX sessions in the gym and all your support in R-related questions; Andi, for the sports events we watched on your couch, the trips to Mainz and Freiburg, and for being chairman together with me of BioContact; Vera, for being my PARPi resistance buddy, for the parties at your place, and for organizing (most of) the lab events; Shubhankar, for being the person who makes everybody happy when you are around; Manu, for our talks about football and your impressive knowledge about new technologies that you were always happy to share. To all of you, thank you for your friendship, the fun, and for motivating me to keep on doing my PhD, happy hours and parties, and our trip to Europapark. You were special to me during my time at HI-STEM, and I will forever be grateful for our time together.

At the end, I would like to thank my whole family, especially my parents Dorothea and Andreas, for their support during my PhD and throughout my whole life! You always supported, believed, and encouraged me in what I was doing; I could not have wished for better parents.

Abschließend möchte ich meiner ganzen Familie, insbesondere meinen Eltern Dorothea und Andreas, für ihre Unterstützung während meiner Promotion und während meines gesamten Lebens danken! Ihr habt mich immer unterstützt, an mich geglaubt und mich ermutigt in dem, was ich gemacht habe; ich hätte mir keine besseren Eltern wünschen können!

Lastly, I would like to thank Lena for accepting and holding out after only five months of our relationship when I moved to Heidelberg to do my PhD. I am really happy that we are still together, and I am very much looking forward to our future.

10. List of abbreviations

%	Percent
° C	degree celsius
Ab	Antibody
ADP	Adenosine diphosphate
alt-NHEJ	alternative end joining
Asc	Ascites
ATP	Adenosine triphosphate
BCA	Bicinchoninic Acid
BER	base excision repair
BFP	Blue fluorescent protein
bp	base pair
BrdU	Bromdesoxyuridin
BrdU	5-Bromo-2'-deoxyuridine
BSA	bovine serum albumin
Cas	CRISPR associated
CD	cluster of differentitation
CFA	colony forming assay
COBG	CO2-independent medium
CRISPR	clustered regularly interspaced short palindromic repeat
crRNA	CRISPR RNA
CSC	Cancer stem cell
CTB	Cell Titer Blue
CV	cristal violet
DAPI	4′,6-diamidino-2-phenylindole
ddH2O	sterile, nuclease-free water
DEG	differentially expressed genes
DKFZ	german cancer reserach center
DMEM	Dulbeccos Modified Eagle Medium
DMSO	dimethylsulfoxide
DNA	deoxyribonucleic acid
DSB	double-strand break
EMA	European Medicines Agency
EpCAM	epithelial cell adhesion molecule
FACS	fluorscent activated cell sorting
FC	fold change
FCCP	carbonyl cyanide-p-trifluoromethoxyphenylhydrazone
FCS	fetal calf serum
FDA	American Food and Drug Administration
FDR	false discovery rate
FW	forward
GFP	Green fluorescent protein

GPCF	Genomics and Proteomics Core Facility
gRNA	guide RNA
GSEA	gene set enrichment analysis
Gy	Gray
h	hour
H_20	water
HGSOC	High-grade serous ovarian cancer
HR	Homologous recombination
HRD	Homologous recombination deficinecy
IC_{50}	half-maximal inhibitory concentration
IF	Immunofluorescence
indel	inserion or delition
IR	ionizing radiation
kDa	kilo Dalton
KO	knock-out
L	liter
LDS	Lithiumdodecylsulfate
log_2FC	log2 fold change
LOH	loss of heterozygosity
M	Mol
mg	milligram
min	minutes
Mio	million
mL	milliliter
mm	millimeter
mM	millimolar
MMR	mismatch repair
MMS	methyl methanesulfonate
mRNA	messenger ribonucleic acid
ms	millisecond
MsigDB	Molecular signature data base
MW	molecular weight
NaCl	sodium chloride
NAD	Nicotinamide adenine dinucleotide
NADH	nicotinamide dinucleotide hydrogen
NADPH	nicotinamide dinucleotide phosphate hydrogen
NER	ucleotide excision repair
ng	nanogram
NHEJ	non-homologous end joining
nM	nanomolar
NT	non-targeting
OC	Ovarian cancer cell line
OCR	oxygen consumption rate
ODCF	Omics IT and Data Management Core Facility

OS	overall survival
OTM	Olive Tail Moment
OxPhos	oxidative phosphorylation
PAM	protospacer adjacent motif
PAR	poly (ADP-ribose)
PARP	poly (ADP-ribose) polymerase
PARPi	PARP inhibitor
PARPis	PARP inhibitors
PBS	phosphate buffered saline
PC	principal component
PCA	principal component analysis
PCR	polymerase chain reaction
PE	paired end
PFA	paraformaldehyde
pH	potential of hydrogen
PVDF	Polyvinylidenfluoride
R	PARPi resistant
Rev	reverse
RFP	red fluorscent protein
RNA	ribonucleic acid
RNP	ribonuceloprotein
ROS	reactive oxygen species
rpm	rounds per minute
RT	room temperature
RT-qPCR	reverse transcriptase-quantitative polymerase chain reaction
S	PARPi sensitive
sec	second
SSB	single-strand break
STS	staurosporine
TBS	Tris-buffered saline
TBST	TBS + 0.05 % Tween 20
TCEP	Tris(2-chlorehyl)phosphate
TCGA	The Cancer Genome Atlas
Td	doubling time
tracrRNA	tracer RNA
UV	ultra violet
V	voltage
v.	version
WB	western blot
WT	wild-type
x g	relative centrifugal force
ZIP	zero-interaction potency
µg	microgram